Department of Physics and Astronomy
Heidelberg University

Master thesis
in Physics
submitted by
Niklas Euler
born in Bremen
2021

Certification of High-Dimensional Entanglement in Ultracold Atom Systems

This Master thesis has been carried out by Niklas Euler
at the
Kirchhoff-Intstitute of Physics
under the supervision of
Herrn Priv.-Doz. Dr. Martin Gärttner

Certification of High-Dimensional Entanglement in Ultracold Atom Systems:

Quantum entanglement has been identified as a crucial concept underlying many intriguing phenomena in condensed matter systems, such as topological phases or many-body localization. Recently, instead of considering mere quantifiers of entanglement like entanglement entropy, the study of entanglement structure in terms of the entanglement spectrum has shifted into focus, leading to new insights into fractional quantum Hall states and topological insulators, among others. What remains a challenge is the experimental detection of such fine-grained properties of quantum systems. Here we present a method to bound the width of the entanglement spectrum or entanglement dimension of cold atoms in lattice geometries, requiring only measurements in two experimentally accessible bases and utilizing ballistic time-of-flight (ToF) expansion. Building on previous proposals for entanglement certification for photon pairs, we first consider entanglement between two atoms of different atomic species and later generalize to higher numbers of atoms per species and multispecies configurations showing multipartite high-dimensional entanglement. Through numerical simulations of a Fermi-Hubbard system we demonstrate that our method is robust against typical experimental noise effects and that the required measurement statistics is manageable.

Zertifizierung von hochdimensionaler Verschränkung in ultrakalten Atomsystemen:

Quantenverschränkung wurde als Schlüsselkonzept der Quantenmechanik identifiziert, das essentiell für die Erklärung von einer Vielzahl von physikalischen Phänomenen ist. Insbesondere in der Festkörperphysik konnte Verschränkung mit topologische Phasen und Vielteilchen-Lokalisierung in Verbindung gebracht werden. In den letzten Jahren wird daher Verschränkung nicht mehr nur anhand von reinen Verschränkungszeugen untersucht, sondern vermehrt auch durch die Analyse des zugrundeliegenden Verschränkungsspektrums selbst. Dies führte unter anderem zu neuen Einsichten in topologische Isolatoren und in den fraktionalen Quanten-Hall-Effekt. Der experimentelle Zugang zum Verschränkungsspektrum und zu anderen hochaufgelösten Eigenschaften von Quantenzuständen bleibt bis jetzt jedoch überaus herausfordernd. In dieser Arbeit präsentieren wir eine neue Methode, um die Breite des Verschränkungsspektrums von Systemen von kalten Atomen in optischen Gittern abzuschätzen. Dafür benötigen wir Messungen in nur zwei experimentell zugänglichen Basen und nutzen hierfür sogenannte "time-of-flight"-Messmethoden (ToF). Angelehnt an einen Vorschlag aus der Quantenoptik für verschränkte Photonenpaare beginnen wir mit zwei verschränkten Atomen und generalisieren das Ergebnis dann für Vielteilchen-Konfigurationen in zwei oder mehreren Spinzuständen, welche dann echte Vielparteienverschränkung aufweisen. Abschließend demonstrieren wir anhand numerischer Simulationen eines Fermi-Hubbard-Systems die Stabilität des hier vorgestellten Verfahrens hinsichtlich üblicher experimenteller Fehlerquellen und endlicher Messstatistik.

Contents

1. Introduction

Of all concepts and constructions unearthed since the introduction of quantum mechanics, quantum entanglement is perhaps the most counter-intuitive for us classical humans. It has no counterpart in any classical description of nature and therefore sets apart what is "classical" and what is inherently "quantum". Initially, the idea of nonlocality - "spooky action at a distance" - was subject of controversial debate in the scientific community, so instead models based on hidden variables were conceived to explain the strange observed correlations in remote measurements [1]. This changed decisively with a landmark paper by Bell [2] which demonstrated how quantum mechanics and local hidden variable theories lead to measurable differences. He concluded that "some mechanism" must exist that would allow remote influence between particles that had interacted before - the first description of what would later be called entanglement. Since then quantum entanglement has been identified as a key aspect in the understanding of a plethora of physical phenomena, such as the dynamics of disordered spin systems [3], the thermalization in closed systems [4, 5], or even in the context of the black hole information paradox [6]. But entanglement is not just some scientific property of quantum matter far removed from practical application in any real world scenarios. Over the last decades, a branch of novel quantum technologies has emerged, which utilize entanglement as a physical resource [5, 7]. Notable examples of successful implementations are quantum key distribution [8–10] for entanglement-enabled quantum cryptography, and quantum teleportation [11–13] as well as superdense coding [14, 15] for advanced quantum communication techniques.

In recent years, much attention has been directed towards the effects of entanglement in condensed matter, where it has been linked to topological properties of quantum states [16, 17] and quantum phase transitions [18–20], among others [21]. Investigating these many-body systems directly is oftentimes too challenging due to limited experimental control and measurement capabilities. Furthermore, exponential growth of the Hilbert space generally prohibits scalable numerical simulation. In the low entanglement regime tensor network states provide an efficient approach to investigate many-body systems with discrete local degrees of freedom, but they are not suitable for states with high-dimensional entanglement [22]. A common approach to simulate complex quantum systems is to construct simpler synthetic systems called quantum simulators which mimic, or emulate, the dynamics of the system of interest. Over the last two decades, cold atoms in optical lattices have evolved into the leading platform for quantum simulation of condensed matter systems [23–29]. Through the application of external fields, model parameters can be tuned within a broad regime, ranging from strong repulsive to attractive interactions, equipping the system with an ideal framework to simulate high-dimensional quantum states with single atom resolved readout [30–33]. The capability to detect entanglement in these platforms is crucial for the investigation of aforementioned processes, but is a challenging undertaking, as determining if a general quantum state ρ is separable can be proved

to be NP-hard [34]. Many experimental implementations can in fact only indicate ("witness") the existence of entanglement in a state qualitatively [35].

In this work we want to go beyond simple witnessing and instead make statements on the internal entanglement structure. The standard measure of entanglement for bipartite pure quantum states $\rho_{AB} = |\psi\rangle\langle\psi|$ is the entanglement entropy defined as $S(\rho_A) = S(\rho_B) = -\sum_{i=1}^{d} p_i \log p_i$ with the reduced density matrix $\rho_A = \mathrm{Tr}_A(\rho_{AB})$ (ρ_B analogously) and its eigenvalues p_i [5]. Even though in many cases much can be learned from this quantity, it contains less information than the full eigenvalue spectrum from which it is derived. Therefore, more recently the eigenvalue spectrum itself has been used extensively to investigate the role of entanglement in different phenomena including fractional quantum Hall states [36], topological insulators and superconductors [37], 1D-systems in the scaling regime [38], emergent irreversibility [39, 40], and in many-body localization transitions [41, 42], leading to new insights. Furthermore, the ability to prepare and certify high-dimensional entanglement would enable the use of algorithms utilizing quantum states with higher dimensions, leading to quantum speedup [43–45]. The number of non-vanishing terms in the eigenvalue spectrum is known as the entanglement dimension or Schmidt rank of the state. It represents the number of terms needed to faithfully represent the wave function in the product Hilbert space (with generalizations established for mixed states). Standard methods to obtain the entanglement dimension for cold atom systems available today are based on full state tomography (FST) or on efficient fidelity measurement schemes, for which the number of required measurement bases scales with the local Hilbert space dimension L like $\sim L$ or $\sim L^2$ respectively [35]. Recently, new variational approaches to learn the entanglement Hamiltonian and thus the entanglement spectrum have been explored [46, 47]. These methods are restricted to states well modeled through few parameters, or alternatively, to states for which the entanglement Hamiltonian is a sum of local operators. Any results from these methods can only be interpreted as entanglement information for pure states; for mixed states the entanglement Hamiltonian has no immediate meaning for the entanglement of the state. This renders these methods impractical in the high-dimensional regime, where many wave function contributions are needed to faithfully represent quantum states.

We propose an alternative approach to certify entanglement in ultracold few-body atom systems. Our method is inspired by earlier findings for entangled photon pairs in different polarization states [48]. In that work the authors construct a bound on the state fidelity to a highly entangled reference state. This approach provides a powerful tool as one can define a set of fidelity thresholds with each threshold corresponding to a matching minimum entanglement dimension of the measured state [49]. Bounds on the fidelity to the reference state thus naturally translate to bounds on the entanglement dimension of the prepared quantum state. One can construct such a bound by measuring in only two mutually unbiased bases (MUB) $|i\rangle_{\mathrm{m}}$ and $|i\rangle_{\mathrm{n}}$, i.e. $\forall i, j : {}_{\mathrm{m}}\langle i|j\rangle_{\mathrm{n}} = L^{-1}$, simplifying experimental procedure significantly. Implementation of two such MUB measurements for cold atom systems is a challenging problem.

Our main contribution is to derive a fidelity lower bound that only requires position and momentum correlation measurements, independent of system size. Both bases can be accessed experimentally by measuring the atom positions *in situ* and after time-of-flight expansion [33, 50], techniques which have been recently demonstrated [51]. The bound can be used as described above to bound the entanglement dimension of experimental states. We find that this protocol can be applied for bipartite systems with multiple particles per species (party) and in a multipartite setting. One might expect that a bound based on the fidelity to a reference state gives satisfactory result only for experimental states close to that reference, i.e. for states whose reduced density matrix spectrum is similar to that of the reference state. Our findings indicate, however, that the entanglement dimension that is certified when using the maximally entangled state as reference can be understood as the number of macroscopic eigenvalues in the prepared state. The bound turns out to be robust against typical experimental noise sources and its tightness decreases only linearly with the noise strength, i.e. with the purity of the prepared state.

The observed entanglement dimension can also be used to make further statements about the experimental quantum state under investigation. We demonstrate that our method can indicate disorder in the periodic potential landscape and thus localization effects, even if the disorder fluctuates from shot to shot. This seems counter intuitive at first, as each shot is one probe of a changing probability distribution, but we show that only localization effects can decrease the fidelity without loss of bound tightness.

The remainder of this thesis is structured as follows. We first go over the theoretical basics needed later for our main result in Sec.2. Based on that framework we then formulate a method to measure fidelity bounds for a pair of two entangled atoms in a lattice potential and explain how to extract entanglement information from it in Sec. 3. We give some remarks on used numerical methods for data processing and simulation in Sec. 4. Following up we establish the robustness of our method under realistic experimental conditions using numerical simulations in Sec. 5. Subsequently, we generalize the method to multiple indistinguishable atoms per species (Sec. 6) and to a multipartite setting, where more than two different atomic species are entangled (Sec. 7), sharing genuine multipartite entanglement. Conclusions and discussion of our results are provided in Sec. 8.

2. Theoretical Foundations

In this chapter we introduce some of the basic theoretical concepts and features used extensively throughout this work. We start with some remarks concerning quantum entanglement and how it can be quantified using the Schmidt decomposition in Sec. 2.1. Subsequently, in Sec. 2.2 we derive the nature of single particle wave functions in periodic potentials and explain how they can be used to construct many-body Hamiltonians. We conclude this section with some details on the Fermi-Hubbard Hamiltonian, a toy model of condensed matter we later apply our model to, in Sec. 2.3.

2.1. Quantum Entanglement

Quantum systems can differ in many ways from the classical systems that surround us in our daily lives. The state of a classical system can in principle be known to any given precision, and all conceivable properties of it, such as position or momentum, exist independently of each other at all times [52]. Einstein, Podolsky, and Rosen called such properties "elements of reality" [1], expressing their belief that quantum particles follow the same deterministic principles. They showed that quantum mechanics is incompatible with local realism; remote systems that interacted in the past could influence each other at a distance. Their counterproposal of local hidden variables which govern the dynamics of the systems would be disproved by Bell almost 30 years later, showing that no classical framework could explain the correlations observed between distant systems after prior interaction [2]. Countless experiments have since then conclusively backed up Bell's findings and demonstrated that the rules of quantum mechanics apply [53]. The mechanism for this remote influence is called quantum entanglement, a concept pertinent to compound quantum systems. In the following we introduce the mathematical framework used to describe entanglement and give an outline of how it can be quantified.

We consider two distant quantum systems $|\Psi_a\rangle$ and $|\Psi_b\rangle$. Prior to any interaction, these systems have no knowledge of each other and can be described completely independently using some local bases $|\alpha_i\rangle$ and $|\beta_i\rangle$,

$$|\Psi_a\rangle = \sum_{i=1}^{L} a_i \, |\alpha_i\rangle \qquad |\Psi_b\rangle = \sum_{i=1}^{K} b_i \, |\beta_i\rangle \,, \tag{1}$$

with some basis coefficients a_i and b_i. One can, however, describe both systems at the same time as a separable *tensor product state* $|\Psi_{ab}\rangle = |\Psi_a\rangle \otimes |\Psi_b\rangle$. We now let these systems interact through some local interaction. In general, a simple product of the wave functions does not deliver an adequate description of the system after the interaction anymore. Instead, the two

individual wave functions get replaced by one compound wave function written in a tensor basis of the two individual bases as shown below [54],

$$|\Psi_{ab}\rangle = \sum_{i=1}^{L}\sum_{j=1}^{K} c_{ij}\,|\alpha_i\rangle \otimes |\beta_j\rangle \tag{2}$$

In this picture the wave function can only be written as a product of the two systems, if all but one of the c_{ij} coefficients vanish. A state where this is possible for at least some basis is called a *product state* or *separable*. If instead more than one coefficient takes non-zero value for all basis choices, the two wave functions are said to be *entangled* with each other.

Each tensor product basis derived from two full (orthonormal) basis sets of the two local Hilbert spaces $\mathcal{H}_A$ and $\mathcal{H}_B$ gives in principle a full description of the compound wave function. However, for each state $|\Psi_{ab}\rangle \in \mathcal{H}_A \otimes \mathcal{H}_B$ on the tensor product of the two local Hilbert spaces, there always exists a special, but generically not unique basis choice called Schmidt decomposition [55]. It minimizes the number of non-vanishing coefficients c_{ij}, which we later show to be a helpful property. We now demonstrate how the Schmidt basis can be constructed. Here we restrict us to the simple case of equal local dimensions ($L = K$) [7, p.109]; a full proof for arbitrary local dimensions can be found in [56].

We start with Eq. (2) and interpret c_{ij} as the matrix elements of a generally complex matrix $\boldsymbol{C}$. This matrix can be decomposed using the singular value decomposition, which reads $\boldsymbol{C} = \boldsymbol{U}\boldsymbol{\Sigma}\boldsymbol{V}$, where $\boldsymbol{U}$ and $\boldsymbol{V}$ are unitary matrices and $\boldsymbol{\Sigma}$ is a diagonal non-negative matrix. We therefore are able to replace c_{ij} going forward as

$$|\Psi_{ab}\rangle = \sum_{i,j=1}^{L}\sum_{k=1}^{L} u_{ik}\sigma_{kk}v_{kj}\,|\alpha_i\rangle \otimes |\beta_j\rangle\,. \tag{3}$$

The matrix elements u_{ik} and v_{kj} can be taken as the basis coefficients of two transformed local orthogonal bases $\left|\tilde{\alpha}_k\right\rangle = \sum_{i=1}^{L} u_{ik}\,|\alpha_i\rangle$ and $\left|\tilde{\beta}_k\right\rangle = \sum_{j=1}^{L} v_{kj}\,|\beta_j\rangle$. The remaining non-negative matrix elements of the diagonal matrix $\lambda_k \coloneqq \sigma_{kk}$ are commonly called the Schmidt coefficients and act as the basis weights of the new tensor product basis,

$$\left|\Psi_{ab}\right\rangle = \sum_{k=1}^{L} \lambda_k \left|\tilde{\alpha}_k\right\rangle \otimes \left|\tilde{\beta}_k\right\rangle. \tag{4}$$

Using this decomposition we find a basis where each basis element $\left|\tilde{\alpha}_k\right\rangle \otimes \left|\tilde{\beta}_k\right\rangle$ is characterized by only one index instead of the previous two for the two subsystemse. The maximum number of terms is hence reduced from L^2 to L. Since the local bases $\left|\tilde{\alpha}_k\right\rangle$ and $\left|\tilde{\beta}_k\right\rangle$ are orthogonal,

no other basis choice can be found which reduces the number of non-negative λ_k even further. Oftentimes, one refers to the set of coefficients λ_k as the *entanglement spectrum*.

Whereas a Schmidt decomposition can be found in the above fashion for all bipartite pure quantum states, no straight-forward generalization to higher-dimensional partitions exist [57]. Certain states like the GHZ-state and its generalization however can be written in an analogous way. We cover this topic in more detail in Sec. 7.1.

The Schmidt coefficients are well suited to describe the entanglement of bipartite quantum states as they give a complete picture of the probability distribution between the Schmidt basis elements. Furthermore, there exists a clear recipe on how to obtain the coefficients, which allows comparison between different systems. However, in many cases it is sufficient to utilize simpler qualitative or quantitative measures of entanglement derived from the Schmidt coefficients instead. One of the standard entanglement measures is the entanglement entropy $S(\lambda_i^2) = -\sum_{i=1}^{L} \lambda_i^2 \log \lambda_i^2$ [5]. For separable states holds $S = 0$, whereas maximally entangled states with local dimension L have $S = \log_2 L$. While these entanglement measures are informative, they do not hold the full information contained in the full set of Schmidt coefficients. In recent years, much effort has been made to investigate the coefficients directly through numerical simulation as well as experiments [36–42]. Obtaining the coefficients experimentally however is a challenging task and requires a lot of physical resources.

Alternatively, one can measure the number of non-vanishing Schmidt coefficients, also known as *Schmidt rank* or *entanglement dimension* D_{ent}. Per definition, for separable states $D_{\text{ent}} = 1$. Conversely, any state with more than one entanglement dimension is considered to be entangled.

The concept of entanglement, and with it a generalization of the Schmidt rank, can also be translated into the framework of mixed quantum states. Mixed states are "noisy" quantum states consisting of a mixture of pure components. It is therefore not possible to assign a single state vector to them, but rather one needs to write them in the formalism of density matrices. The density matrix of a pure state $|\psi\rangle$ is simply given by $\rho = |\psi\rangle\langle\psi|$. General mixed state need to be written as a mixture of several pure components, $\rho = \sum_i p_i \, |\psi_i\rangle\langle\psi_i|$ with $\sum_i p_i = 1$ [5]. The decomposition of a given density matrix into pure states is in general not unique, which complicates a clear definition of entanglement for mixed bipartite quantum states in contrast to the pure states outlined above. A mixed quantum state is considered to be entangled iff no decomposition into product states exist. Solving this problem has been proved to be a NP-hard problem [5, 34].

This ambiguity of decomposition convolutes the definition of a Schmidt rank for mixed states: Every decomposition has different pure components with unique Schmidt coefficients and Schmidt rank. As a consequence, one typically defines a *Schmidt number* $D_{\text{ent}}(\rho)$ for mixed

states using a convex roof construction. It is defined as the maximum Schmidt rank $D_{\text{ent}}(\psi)$ among all pure components ψ_i of a mixed state, minimized over all possible decompositions [5, 58],

$$D_{\text{ent}}(\rho) = \min_{\text{decomp.}}\{\max_i[D_{\text{ent}}(\psi_i)]\} \tag{5}$$

The entanglement spectrum therefore is not a good entanglement quantifier of mixed states, but the Schmidt number still is. For the remainder of this work we will use the term entanglement dimension when talking about pure as well as mixed states, where in the latter case the generalized Schmidt number is meant.

The main contribution of this work is the development of a new method to extract the entanglement dimension of cold atoms in optical lattice potentials. The derivation of the details of this result is discussed in Sec. 3.

2.2. Single Particle Wave Functions in Periodic Potentials

Solid state materials have the defining feature of being centered around a periodic lattice structure consisting of ions. This lattice acts as a periodic potential on the free electrons available in the material and is the foundation for the characteristic electronic properties of solid state matter [59]. Experimental probes into these materials have been found to be immensely difficult due to naturally occurring imperfections and fast-paced dynamics [25]. Numerical simulations of these systems well in the many-body regime are also prohibitively complex and hence restricted to the sparsely populated few-body regimes or subjected to confining simplifications [22].

Over the past 20 years, a third scientific avenue originally conceptualized by Feynman [60] has made significant progress and is now at a stage where reliable results can be produced with high frequency: Quantum simulation. Instead of probing real solid state materials, one sets up a synthetic system in the laboratory, designed to capture (what is believed to be) the essence of the real system under investigation [28]. Cold atoms in optical lattices have been used extensively to simulate the dynamics typically found in condensed matter with great success [23–29]. The system is built around an optical lattice to resemble a periodic ion structure and is thus able to reproduce much of what is observed in real solid state materials. Typical experiments use atoms which are $\sim 10^5 - 10^6$ times heavier than electrons, have been cooled to the $\mathcal{O}(10^{-9}\,\text{K})$ regime, and utilize optical lattices with lattice site spacings a factor of $\sim 10^3$ wider than natural ionic lattices [33]. All these differences combined yield dynamics several orders of magnitude slower in the synthetic system, giving sufficient time for in-depth observation [61, 62]. Experimentalists can then reintroduce new features such as interactions and tune the system parameters over

a wide range, making the system a platform for comprehensive simulation applications. We discuss a common system choice and its realizations in the following section in more detail.

Even though many of the complications like impurities and lattice vibrations are removed from the dynamics of a synthetic system, deriving many-body wave functions in such a complex potential landscape is still a non-trivial task. For deep potential wells it is sensible to expand the wave function in terms of a single particle basis localized on the lattice sites, known as the Wannier basis [63]. We first derive this set of localized basis functions for a given periodic potential in typical experimental applications and in a second step construct the desired Hamiltonian based on these functions. Any Hamiltonian with local interactions can in principle be developed in terms of single particle wave function tensor products, and thus the dynamics of the spatial wave function can be studied in detail.

There are several ways to implement periodic potentials in the lab available to experimentalists today. The most common and straightforward method works by producing a standing wave of laser light, which then induces an electric dipole moment in the atoms through the inhomogeneous AC stark effect [24, 27]. Utilizing several laser sources in parallel opens up a wide variety of lattice geometries of different dimensionalities, so even complex crystal structures can be realized [27, 33]. By choosing either a red-detuned or blue-detuned wavelength with respect to the atom transition frequency, the potential can be made either attractive or repulsive [24]. The strength of the potential is proportional to the intensity of the laser field, yielding the following form in one dimension,

$$V = -V_0 \cdot \sin^2(k_l \cdot x), \tag{6}$$

with the lattice spacing $d = \lambda/2$, the wavenumber $k_l = \pi/d$, and the amplitude $V_0 > 0$ depending on the laser intensity and atom polarizability [28]. This lattice in combination with confining potentials in the other two dimensions forms the potential landscape of the experiment investigated in this work. An alternative approach is given through the use of microtraps, called optical tweezers. These traps can be created and manipulated individually and allow for very close positioning of adjacent lattice sites [33], but are a source of uncorrelated potential noise, which can impact atom populations tremendously as we show later. Through arrays of optical tweezers it is possible to create potentials of the form of Eq. (6) with a site-dependent amplitude $V_0(x)$. This gives experimentalists a precision tool to alter state populations. We will explore this possibility at a later point in Sec. 5. In the following we deduce the form of the single-atom wave function in a periodic potential of the form of Eq. (6). The Hamiltonian describing the dynamics of the system is given by

$$H = \frac{-\hbar^2}{2m}\frac{\partial^2}{\partial x^2} - V_0 \cdot \sin^2(k_l \cdot x). \tag{7}$$

The potential clearly is of the form $V(x) = V(x + nd)$ with $n \in \mathbb{N}$ and the lattice separation d and thus has the same periodicity by construction as the underlying lattice. Using Bloch's theorem, one can rewrite the eigenstates of this Hamiltonian as a phase factor times a function of the lattice period,

$$\psi_{nq}(x) = \exp(iqx) \cdot u_{nq}(x), \tag{8}$$

with the band index n and the lattice momentum q [59]. Since $u_{nq}(x)$ is a periodic function, it can be decomposed into its Fourier components as follows,

$$u_{nq}(x) = \lim_{j\to\infty} \sum_{p=-j}^{j} c_{nq}^{p} \exp\left(2\pi i \cdot \frac{px}{d}\right). \tag{9}$$

Here we write the infinite sum as the limit of some index j; in numerical implementations one can introduce a cutoff $j_{\max}$ to deal with the infinities [64]. Combining this wave function ansatz with the Hamiltonian of Eq. (7), one arrives at the full Schrödinger equation given by

$$\lim_{j\to\infty} \left(\frac{-\hbar^2}{2m}\frac{\partial^2}{\partial x^2} - V_0 \cdot \sin^2(k_l \cdot x) - E_{qn}\right) \left[\exp(iqx) \cdot \sum_{p=-j}^{j} c_{nq}^{p} \exp\left(2\pi i \cdot \frac{px}{d}\right)\right] = 0. \tag{10}$$

In the following we neglect all higher bands and assume that only the lowest energy band $n = 1$ is occupied and omit the band index n going forward. We continue by resolving the derivative and replacing $\sin(x) = [\exp(ix) - \exp(-ix)]/2i$ to obtain

$$\begin{aligned} &\lim_{j\to\infty} \left[\exp(iqx) \cdot \sum_{p=-j}^{j} c_{q}^{p} \exp(2ixk_l p)\right] \\ &\cdot \left\{\left(2p + \frac{q}{k_l}\right)^2 \cdot \underbrace{\frac{\hbar^2 k_l^2}{2m}}_{=:E_r} + \frac{V_0}{4}\left[\exp(2ixk_l) + \exp(-2ixk_l) - 2\right] - E_q\right\} = 0\,. \end{aligned} \tag{11}$$

Reorganization of the exponential functions and division by $\exp(iqx)$ leads to a simplified version of the equation, where we pulled out the eigenenergy and separated it from the other terms as shown below,

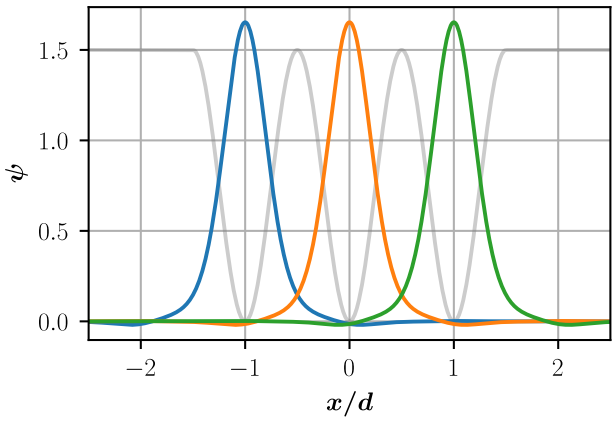

Figure 1: Wannier basis of a triple-well. The basis shape is approximately Gaussian, but each wave function is negative in the vicinity of adjacent lattice sites to ensure orthonormality. Grey line in the background is a sketch of the lattice potential, where finite size effects have been neglected.

$$\lim_{j\to\infty}\sum_{p=-j}^{j} c_q^p \Bigg\{ \left[\left(2p+\frac{q}{k_l}\right)^2 E_r - \frac{V_0}{2}\right]\exp(2ixk_lp) + \frac{V_0}{4}\left\{\exp[2ixk_l(p-1)] + \exp[2ixk_l(p+1)]\right\}\Bigg\} = E_q \sum_{p=-j}^{j} c_q^p \exp(2ixk_lp). \tag{12}$$

This still somewhat cumbersome equation is cleared up by first multiplying with $\exp(-2ixk_lp')$ and then integrating over x. In this way, all exponentials are replaced with Dirac delta functions respectively,

$$E_q c_q^{p'} = \lim_{j\to\infty}\sum_{p=-j}^{j} c_q^p \left\{\left[\left(2p+\frac{q}{k_l}\right)^2 E_r - \frac{V_0}{2}\right]\delta(p-p') + \frac{V_0}{4}\left[\delta(p-p'-1)+\delta(p-p'+1)\right]\right\} \tag{13}$$

Finding the Fourier components of the lattice-periodic part of $u_q(x)$ is thus a tridiagonal eigenproblem which can be solved through exact diagonalization [64]. The so obtained Bloch functions are highly delocalized as they are invariant under translation with a lattice vector; they are not a viable basis choice to develop highly localized atom states in. By instead applying a quasimomentum Fourier transformation to the Bloch wave function basis set, one obtains a localized basis of eigenfunctions of the single-atom Hamiltonian called Wannier basis [27, 64]

$$w_i(x) \coloneqq w(x-x_i) = \frac{1}{\sqrt{L}}\sum_{q\in\mathrm{BZ}} \exp(-iqx_i)\psi_q(x), \tag{14}$$

with $w_i(x)$ being the Wannier basis function of site i. In one dimensions this explicit choice of phase factors is guaranteed to yield a maximally localized basis function, but for higher

dimensions with non-separable potentials finding the optimal phase factors is a non-trivial problem and remains under investigation [28, 65]. The function shape is well approximated by a Gaussian close to the center of the lattice site, but shows deviation as soon as the function reaches into the next lattice site. In that region the actual Wannier function is negative (shown in Fig. 1) so that the overlap integral $\int \mathrm{d}x\, w_i(x) w_j(x) = \delta_{ij}$ observes the required orthonormality condition.

2.3. Fermi-Hubbard Model

With the localized single particle Wannier wave functions derived in the previous section in place, one has a complete basis set to describe single particle dynamics in lattice potentials. These functions however can also be utilized for the investigation of many-body quantum systems. By developing the corresponding Hamiltonian in terms of the tensor product basis of single particle Wannier functions, one can map the interactions and dynamics of the Hamiltonian to a set of local basis functions in a natural way.

One common choice of a relatively simple yet feature-rich system description for interacting fermions in a lattice is the Fermi-Hubbard model [66]. It assumes a deep periodic potential and thus strong localization on the lattice sites, known as "tight binding", which justifies the expansion in localized basis functions. Additionally, only the lowest energy band is filled in such a configuration [64]. The model includes tunneling with magnitude J only to adjacent lattice sites, as next-to-nearest neighbour wave function overlap is severely suppressed due to the strong localization. Furthermore, through application of external magnetic fields, one can induce an attractive or repulsive atom-atom contact interaction. The dynamics are schematically depicted in Fig. 2.

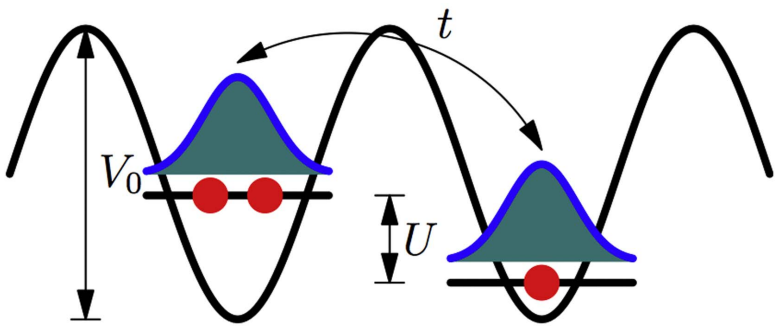

Figure 2: Schematic of Fermi-Hubbard model in an optical lattice. Fermions can tunnel between adjacent site with tunneling strength J (or t) and have a contact interaction of strength U. The wave function can be expanded in terms of localized single particle Wannier functions [28].

Both tunneling and contact interaction are captured by the Fermi-Hubbard Hamiltonian

$$\hat{H} = -J \sum_{\sigma} \sum_{i,j} (\hat{c}^{\dagger}_{i,\sigma} c_{j,\sigma} + \text{h.c.}) + U \sum_{i} \hat{\text{n}}_{i\downarrow} \hat{\text{n}}_{i\uparrow} \,, \tag{15}$$

with the tunneling strength J, interaction strength U, creation (annihilation) operator $\hat{c}^{\dagger}_{i,\sigma}$ ($\hat{c}_{i,\sigma}$) for an atom on site i and spin state $\sigma \in \{\uparrow, \downarrow\}$ and their corresponding atom number operators $\hat{\text{n}}_{i\downarrow}$, $\hat{\text{n}}_{i\uparrow}$. Only adjacent pairs of lattice sites are considered in the second sum of the tunneling contribution. The interaction strength U is given by [24]

$$U = \frac{4\pi a}{m} \int \text{d}x \, |w(x)|^4, \tag{16}$$

with atom mass m and scattering length a. By varying the magnetic field in the vicinity of the Feshbach resonance of the two atomic species present, one can tune a, and therefore also the interaction strength U [67]. Since the atoms are in different spin states, they can be distinguished by their different atomic transmission frequencies. It is hence possible to resolve single atoms using fluorescence imaging, which enables the needed accuracy to measure fine-grained properties of quantum states [33].

The whole system is then characterized by the ratio U/J, where negative values correspond to attractive and positive values to repulsive interactions. A two-body ground state wave function representation for a lattice of $L = 6$ sites, two atoms, and an attractive interaction ($U/J = -12$) is depicted in Fig. 3(a) in Sec. 3. We choose this specific model implementation to test our entanglement bound based on its simplicity, experimental feasibility, and widespread use in numerical modeling [27, 64], but other configuration with bosons or higher bands could also be analyzed.

3. Bound on Entanglement Dimension

In this work we show that it is both feasible and insightful to experimentally determine the entanglement dimension of cold atom systems in lattice potentials. We first focus to introduce the basic idea of our method here and add model extension in later sections.

Any bipartite product Hilbert space is bounded by the size of the smaller of the two local Hilbert spaces, $k_{\max} = \min[\dim(\mathcal{H}_A), \dim(\mathcal{H}_B)] =: L$, which we take to be finite and identical in this work. One can choose a maximally entangled state (MES) of that Hilbert space with equal coefficients for all L terms,

$$|\Psi\rangle_{\mathrm{MES}} = \frac{1}{\sqrt{L}} \cdot \sum_{m=1}^{L} |mm\rangle \,. \tag{17}$$

This highly entangled state has the maximum entanglement dimension $D_{\mathrm{ent}}^{\max} = L$ and acts as an entanglement reference to which experimentally prepared states ρ can be compared. The two subsystems are given by the two atom positions in the lattice; later we can exchange the single atoms with more complex systems of atoms. The maximally entangled state of the Hubbard Hamiltonian therefore represents a superposition of atom pairs on the same site, equally distributed among all sites.

The fidelity of the experimental state ρ to the maximally entangled reference state

$$F(\rho, \Psi_{\mathrm{MES}}) = \frac{1}{L} \cdot \sum_{m,n=1}^{L} \langle mm| \, \rho \, |nn\rangle \tag{18}$$

implies a convenient state distance measure to compare the two states, as it is bounded in dependence of the entanglement dimension of ρ. One can explicitly construct a set of bounds B_k on the fidelity to the maximally entangled state $F(\rho, \Psi_{\mathrm{MES}})$, given by

$$F(\rho, \Psi_{\mathrm{MES}}) \leq \mathrm{B}_k(\Psi_{\mathrm{MES}}) = \frac{k}{L}, \tag{19}$$

where k is the entanglement dimension of the experimental state [49, 68]. This inequality also holds for general mixed states occurring in real physical implementations through the Schmidt number (see Sec. 2.1). The violation of this relation for any ρ and given k therefore indicates that ρ is entangled with a dimension of $D_{\mathrm{ent}} = k + 1$ or higher. The set of thresholds is immediately clear from the local dimension L and does not require complicated computations. This not only gives a robust entanglement witness since the lowest threshold $\mathrm{B}_1 = L^{-1}$ already indicates entanglement, but also bounds the width of the entanglement spectrum and hence

gives insight into the internal entanglement structure. We will show this in Sec. 5.3 on the example of localized states where the number of macroscopic eigenvalues can be related to the entanglement dimension. Additionally, one can use the fidelity to construct lower bounds on the entanglement of formation as has been shown in [48, 69], establishing $F(\rho, \Psi_{\mathrm{MES}})$ as a versatile source of information about the entanglement content of ρ. On the other hand, a fidelity measurement comes at significant experimental complexity, in general requiring measuring in $L+1$ different bases for a L dimensional local Hilbert space [48].

Our method bounds the fidelity from below, but always uses only two measurement bases, independent of the local Hilbert space dimension. We now go on and explicitly construct this bound $\tilde{F}(\rho, \Psi_{\mathrm{MES}})$.

It is insightful to split the fidelity [Eq. (18)] into two terms,

$$F(\rho, \Psi_{\mathrm{MES}}) = \sum_{m=1}^{L} \frac{\langle mm| \rho |mm\rangle}{L} + \underbrace{\sum_{\substack{m,n=1 \\ m\neq n}}^{L} \frac{\langle mm| \rho |nn\rangle}{L}}_{F_{\mathrm{coh}}}, \tag{20}$$

dividing the contributions into state populations (left sum) and two-particle coherences F_{coh} (right sum). The state populations of the two distinguishable species, here labeled as $\uparrow$ and $\downarrow$ with their corresponding number operators $\hat{\mathrm{n}}_\uparrow$ and $\hat{\mathrm{n}}_\downarrow$, can be obtained by spatially discretizing the joint density distribution $\langle \hat{\mathrm{n}}_\uparrow(x_1)\hat{\mathrm{n}}_\downarrow(x_2)\rangle$. This distribution can be probed directly through single particle resolved fluorescence imaging, allowing for an exact in situ measurement [33, 51, 70]. A representation of $\langle \hat{\mathrm{n}}_\uparrow(x_1)\hat{\mathrm{n}}_\downarrow(x_2)\rangle$ for the ground state of a Fermi-Hubbard Hamiltonian with $L = 6$ at $U/J = -12$ is displayed in Fig. 3(a) (for more details on the numerical model implementation see Sec. 5). Each grid point represents a contribution to the two-particle state ρ. The signals on the diagonal represent double occupation probabilities, whereas off-diagonal elements correspond to configurations with atoms on different sites [Fig. 3(b)]. The wave function envelope is determined by the underlying Wannier basis of the lattice and depends on the lattice depth V_0 and site spacing d [64].

Such direct experimental readout is not available for the two-particle coherences F_{coh}, but one can construct a bound on the coherences from below by measuring in a second basis. A natural choice for cold atoms is the momentum basis, as the required basis change equivalent to a Fourier transformation can be efficiently achieved by letting the atoms propagate in a weak harmonic potential for $t = T/4$ with T being the trap oscillation period [33, 51]. This is possible, since the eigenfunctions of the quantum harmonic oscillator, the Hermite polynomials, are also the eigenfunctions of the Fourier transformation. For the specific propagation time $t = T/4$, the eigenvalues coincide. Through repeated application of this procedure to an ensemble of states, the momentum correlation function $\langle \hat{\mathrm{n}}_\uparrow(k_1)\hat{\mathrm{n}}_\downarrow(k_2)\rangle$ can then be probed. The joint momentum

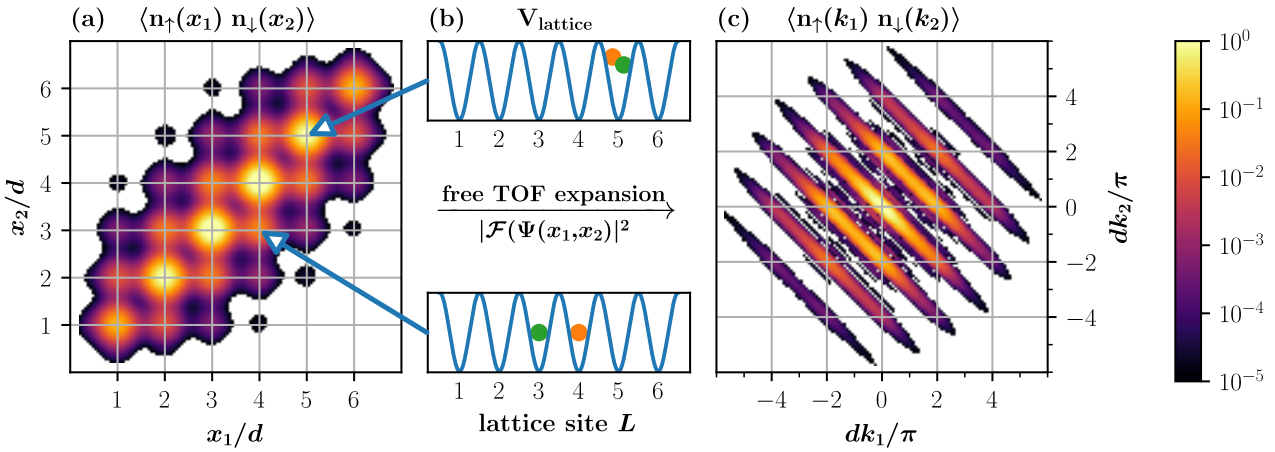

Figure 3: (a) Position space representation of the two-particle ground state wave function $\Psi(x_1, x_2)$ for $L = 6$ lattice sites with lattice spacing d. **(b)** Graphical representation of both particles occupying the same lattice site (top) or adjacent lattice sites (bottom) with the respective signals in (a). **(c)** The lattice momentum correlation function $\langle \hat{n}_\uparrow(k_1)\hat{n}_\downarrow(k_2)\rangle$ corresponding to the position space wave function of (a). All values smaller than 1×10^{-5} in both (a) and (c) have been masked.

distribution to the position distribution shown in Fig. 3(a) is presented in Fig. 3(c). We start to construct the corresponding mathematical transformation operator by stating the effect on the localized Wannier functions of the lattice potential. The basis function for the nth lattice site can be expressed as $w(x - nd)$ due to the translation invariance of the lattice. Any shift in position space causes a phase factor in momentum space, so one obtains

$$\mathcal{F}[w(x - nd)](k) = \tilde{w}(k) \exp(indk) \tag{21}$$

for the single-atom wave function in momentum space [51]. The fermionic number operator in momentum space can therefore be expressed in the position space basis $\{|j\rangle \,|\, j \in \{1, ..., L\}\}$ as $\hat{n}(k) = |\tilde{w}(k)|^2 \sum_{m,n=1}^{L} |m\rangle\langle n| \exp[idk(m - n)]$. The full expectation value $\langle \hat{n}_\uparrow(k_1)\hat{n}_\downarrow(k_2)\rangle$ in the density matrix picture is given by the trace over the product of the two momentum number operators and the density matrix, $\langle \hat{n}_\uparrow(k_1)\hat{n}_\downarrow(k_2)\rangle = \mathrm{Tr}\{\hat{n}_\uparrow(k_1)\hat{n}_\downarrow(k_2)\rho\}$. Finally, by exploiting the cyclic property of the trace, one arrives at the following representation of the momentum correlation operator expectation value, given by

$$\langle \hat{n}_\uparrow(k_1)\hat{n}_\downarrow(k_2)\rangle = \sum_{m,n,m',n'=1}^{L} \phi_{mnm'n'}(k_1, k_2) \cdot \langle mn|\, \rho\, |m'n'\rangle\,, \tag{22a}$$

$$\phi_{mnm'n'}(k_1, k_2) = |\tilde{w}(k_1, k_2)|^2 \cdot \exp\{-id \cdot [(m - m')k_1 + (n - n')k_2]\}. \tag{22b}$$

Each coherence is weighted by $\phi_{mnm'n'}(k_1, k_2)$ [Eq. (22b)], containing the Fourier transformed Wannier envelope $\tilde{w}(k_1, k_2) \coloneqq \tilde{w}(k_1) \cdot \tilde{w}(k_2)$ and a phase factor obtained during the Fourier transformation [70]. Above given description naturally decomposes into a basis of trigonometric basis functions of the two lattice momenta k_1 and k_2 times the Wannier envelope,

$$\langle \hat{\mathrm{n}}_\uparrow(k_1)\hat{\mathrm{n}}_\downarrow(k_2)\rangle = |\tilde{w}(k_1,k_2)|^2 \left\{ \sum_{(\alpha,\beta)\in M} \mathrm{Re}(g_{\alpha\beta}) \cos[d(\alpha k_1 + \beta k_2)] - \mathrm{Im}(g_{\alpha,\beta}) \sin[d(\alpha k_1 + \beta k_2)] \right\}, \tag{23a}$$

$$M = \{(\alpha,\beta) \in \{0,\dots,L-1\} \times \{-(L-1),\dots,L-1\} \mid \alpha > 0 \vee \beta \geq 0\}, \tag{23b}$$

$$g_{\alpha\beta} = 2 \sum_{m=1}^{L-\alpha} \sum_{n=\max(1,1-\beta)}^{\min(L,L-\beta)} \langle mn| \rho |(m+\alpha),(n+\beta)\rangle . \tag{23c}$$

The basis weights $\mathrm{Re}(g_{\alpha\beta})$ and $\mathrm{Im}(g_{\alpha\beta})$ in Eq. (23a) are sums over the real and imaginary parts of the coherences of the density matrix ρ. Each coefficient $g_{\alpha\beta}$ is defined by the pair of numbers $(\alpha,\beta) \in M$ which identifies the admissible "gap pair" of lattice sites between $\langle mn|$ and $|m'n'\rangle$ for coherences $\langle mn| \rho |m'n'\rangle$ to be summed over for that specific coefficient, as shown in Eq. (23c). Using that ρ is Hermitian, we rewrite the sum of relevant coherences F_{coh} introduced in Eq. (20) as

$$\sum_{\substack{m,n=1 \\ m\neq n}}^{L} \frac{\langle mm| \rho |nn\rangle}{L} = \sum_{\substack{m,n=1 \\ m<n}}^{L} \frac{\langle mm| \rho |nn\rangle + \langle nn| \rho |mm\rangle}{L} = \sum_{\substack{m,n=1 \\ m<n}}^{L} \frac{2\,\mathrm{Re}(\langle mm| \rho |nn\rangle)}{L}, \tag{24}$$

demonstrating that it can be replaced by a sum over the real parts of coherences in the upper (or alternatively lower) triangular part of ρ. This fact is encoded in the set definition of M given in Eq. (23b) by forcing the leading non-zero digit of (α,β) to be positive.

Obtaining the coefficients $g_{\alpha\beta}$ is not directly straightforward, as the basis of cosine and sine function introduced in Eq. (23a) is non-orthogonal due to the envelope $|\tilde{w}(k_1,k_2)|^2$ modulating the periodic basis functions [51]. Projecting the measured distribution onto the basis function set therefore yields smeared out coefficients $\mathrm{Re}\, c_{\alpha\beta}$ and $\mathrm{Im}\, c_{\alpha\beta}$,

$$\mathrm{Re}(c_{\alpha\beta}) = \int \mathrm{d}k_1 \mathrm{d}k_2 \, \langle \hat{\mathrm{n}}_\uparrow(k_1)\hat{\mathrm{n}}_\downarrow(k_2)\rangle \cdot |\tilde{w}(k_1,k_2)|^2 \cdot \cos[d(\alpha k_1 + \beta k_2)], \tag{25a}$$

$$\mathrm{Im}(c_{\alpha\beta}) = \int \mathrm{d}k_1 \mathrm{d}k_2 \, \langle \hat{\mathrm{n}}_\uparrow(k_1)\hat{\mathrm{n}}_\downarrow(k_2)\rangle \cdot |\tilde{w}(k_1,k_2)|^2 \cdot \sin[d(\alpha k_1 + \beta k_2)], \tag{25b}$$

where each weight also contains small contributions coming from other cosine or sine basis elements respectively. These additional contributions are proportional to the overlap integral of the two basis functions. It is however possible to explicitly construct the linear transformation $\boldsymbol{Q}$ that maps the actual basis weight distribution $\vec{G}$ to the measured coefficients $\mathrm{Re}(c_{\alpha\beta})$ and $\mathrm{Im}(c_{\alpha\beta})$ contained in $\vec{C}$,

$$\vec{C} = \boldsymbol{Q}\vec{G}, \tag{26}$$

where each matrix element $\boldsymbol{Q}_{mn}$ is given by the respective overlap integrals of the mth and nth basis functions [51]. We prove in Sec. 4.3 that these integrals factorize since the Fourier transformed Wannier envelope factorizes; consequently one only has to compute a small number of 1D integrals linear in the number of lattice sites in order to compute $\boldsymbol{Q}$. The actual basis weights $g_{\alpha\beta}$ are then extracted by inverting $\boldsymbol{Q}$ and rewriting Eq. (26) as

$$\vec{G} = \boldsymbol{Q}^{-1}\vec{C}. \tag{27}$$

The two projection integrals in Eqs. (25a) and (25b) can be evaluated in a simplified way using Monte Carlo importance sampling techniques. By treating the momentum correlation function as a multivariate probability density, it can absorbed in the redefinition of the integration variable. We elaborate on this procedure in Sec. 4.1.

At this point one has obtained access to the basis weights $g_{\alpha\beta}$, which are sums over certain subsets of coherences of ρ. However not only the two-particle coherences relevant for F_{coh} in Eq. (20) are contained within the basis weights $g_{\alpha\beta}$, but also different-site two-particle coherences not contributing to the fidelity $F(\rho, \Psi_{\mathrm{MES}})$. The next step is therefore to subtract a bound of these non-contributing coherences. We note that any general density matrix element is bounded from above by using Cauchy-Schwarz inequality

$$\mathrm{Re}(\langle mn|\,\rho\,|m'n'\rangle) \leq |\,\langle mn|\,\rho\,|m'n'\rangle\,| \overset{\mathrm{CSI}}{\leq} \sqrt{\langle m'n'|\,\rho\,|m'n'\rangle\,\langle mn|\,\rho\,|mn\rangle}, \tag{28}$$

using only already measured state populations and thus adding no new experimental complexity. For pure states the right inequality in Eq. (28) is tight as can be easily seen by inserting any pure quantum state, but grows more loose with increasing mixedness of the state. In the two-atom case presented here the set of $(\alpha, \beta) \in M$, which carries relevant two-particle coherences, reduces to $\alpha = \beta =: \delta \in \{1, \ldots, L-1\}$. The desired sum of relevant coherences can then be extracted by subtracting the bounds in Eq. (28) for all non-contributing coherences from the sum of relevant basis coefficients,

$$\sum_{\substack{m,n=1\\m\neq n}}^{L}\frac{\langle mm|\,\rho\,|nn\rangle}{L}=\sum_{\substack{m,n=1\\m<n}}^{L}\frac{2\,\mathrm{Re}(\langle mm|\,\rho\,|nn\rangle)}{L}\geq$$
$$\sum_{\delta=1}^{L-1}\left(\frac{\mathrm{Re}(g_{\delta\delta})}{L}-2\sum_{\substack{m,n=1\\m\neq n}}^{L-\delta}\frac{\sqrt{\langle m'n'|\,\rho\,|m'n'\rangle\,\langle mn|\,\rho\,|mn\rangle}}{L}\right)=:\ \tilde{F}_{\mathrm{coh}}(\rho,\Psi_{\mathrm{MES}}) \tag{29}$$
$$\text{with}\quad m'\coloneqq m+\delta\quad n'\coloneqq n+\delta$$

where the second sum of the last expression includes all single occupancy coherences. Together with the same site populations displayed in the first sum of Eq. (20) we formulate the complete experimentally accessible bound for the fidelity of the experimental state ρ to the maximally entangled state Ψ_{MES} as

$$\tilde{F}(\rho,\Psi_{\mathrm{MES}})=\sum_{m=1}^{L}\frac{\langle mm|\,\rho\,|mm\rangle}{L}+\tilde{F}_{\mathrm{coh}}(\rho,\Psi_{\mathrm{MES}}). \tag{30}$$

Inserting this bound in Eq. (19) yields

$$\tilde{F}(\rho,\Psi_{\mathrm{MES}})\leq F(\rho,\Psi_{\mathrm{MES}})\leq \mathrm{B}_k(\Psi_{\mathrm{MES}}), \tag{31}$$

analogous to the result for entangled photon pairs obtained in Ref. [48].

To summarize experimental protocol, the implementation of this readout scheme entails the preparation of two atomic species in a periodic potential and consecutive single atom resolved readout of the position space correlation distribution $\langle\hat{\mathrm{n}}_\uparrow(x_1)\hat{\mathrm{n}}_\downarrow(x_2)\rangle$. The signal is discretized by identifying the atom positions obtained in each shot with a pair of lattice sites, which yields the populations $\langle mn|\,\rho\,|mn\rangle$ entering in Eqs. (29) and (30). The momentum space distribution is probed through ballistic time-of-flight expansion, resulting in an effective Fourier transformation of the wave function. From the measured momentum correlation function $\langle\hat{\mathrm{n}}_\uparrow(k_1)\hat{\mathrm{n}}_\downarrow(k_2)\rangle$ the coefficients $c_{\alpha\beta}$ are obtained by projecting onto above specified trigonometric basis functions. Practically, this is done by summing over the basis functions evaluated at the momentum samples (see Sec. 4.1). The corrected expansion coefficients $g_{\alpha\beta}$ are obtained from these sums via Eq. (27) and inserted into Eq. (29), which yields the desired lower bound on the MES fidelity Eq. (30). The statistical requirements for confident certification are discussed in Sec. 5.1 and a study of the robustness of the protocol with respect to typical experimental noise effects is given in Secs. 5.2 and 5.3.

4. Numerical Methods

Several numerical methods and techniques have been developed or adapted for the simulation of the extraction method shown in the previous section. In this chapter we want to illustrate some of key algorithms and implementations that make computation even for bigger system sizes possible. For the sake of simplicity we shall explain these methods for the simple case of two atoms. In later Secs. 6 and 7 configurations with more atoms are introduced, for which we give some remarks on how to generalize to these higher particle numbers. We start with the Monte Carlo scheme for the evaluation of basis coefficients in Sec. 4.1, followed by the sampling method chosen for synthetic data generation in Sec 4.2. Concluding this chapter we discuss how the computation of the basis element overlap matrix $\boldsymbol{Q}$ can be simplified in Sec. 4.3.

4.1. Scalable Numerical Simulation of Momentum Correlations

The extraction of information from the momentum correlations of the many-body wave function is at the heart of the method presented in this thesis. It is therefore necessary to evaluate the momentum correlation function efficiently to obtain the basis weights $g_{\alpha\beta}$ of the trigonometric basis functions defined earlier in Eq. (23c). Since the full density matrix ρ of the simulated state is always known, one can take a direct route in numerical simulations: Obtain the exact weights from the density matrix and multiply them with corresponding trigonometric basis functions to construct the joint momentum distribution. For the small systems presented so far, the resulting distribution and the needed basis functions can easily be discretized on a grid, allowing for simple and fast computation of the required projection integrals presented in Eqs. (25). However, with the generalizations developed later in Secs. 6 and 7, bigger systems with higher particle numbers can in principle be analyzed. Each additional particle increases the dimension of the discretized grid by one. Such a grid with a number of grid points N_{grid} in each dimension has a total of $(N_{\text{grid}})^N$ grid points for N atoms. Considering a resolution of $N_{\text{grid}} = 1000$, for $N = 2$ atoms the size of the grid is in the $\mathcal{O}(\text{MB})$ range, which poses no computational challenge on modern computer systems. For $N = 4$ the complexity changes dramatically already, as the grid size jumps to the $\mathcal{O}(\text{TB})$ range, which is barely accessible to state-of-the-art supercomputers, but still possible. But systems with $N = 6$ at the latest pose an insurmountable challenge due to their characteristic $\mathcal{O}(\text{EB})$ size range, clearly demonstrating that discretization is an infeasible approach for systems even remotely representing many-body dynamics.

A more natural method much closer to experimental procedure is given by drawing samples from the momentum correlation function and using them in a Monte Carlo integration of the projection integrals. There are several advantages compared to discretization which we give in the following. Most importantly, numerical sample production requires significantly less

computer memory resources, as only the samples have to be stored, and not the full grid. For $N = 6$ atoms and a sample size of $N_{\text{sample}} = 1 \times 10^5$, this means a size reduction in computer memory by a factor of $\sim 1 \times 10^{13}$, which places the resource demands again in the $\mathcal{O}$(MB) range!

But besides this very compelling argument, there are other reasons to utilize Monte Carlo methods. Classical Newton-Cotes integration techniques on discretized functions have fast error convergence in low dimensions, but become less efficient in higher dimensions [71]. The integration error term of the commonly used trapezoidal rule, a stepwise linear approximation through trapezoids, scales with the total atom number N like $\sigma_{\text{NC}} \sim 1/N_{\text{grid}}^{2/N}$ [71]. Contrarily, Monte Carlo methods are slower than Newton-Cotes techniques in low dimensions, but do not scale with the dimensions of the integral, yielding $\sigma_{\text{MC}} \sim 1/\sqrt{N_{\text{sample}}}$ [72]. They are thus on par for integrals with $N = 4$ dimensions and have favourable scaling for even higher configurations. It should be noted that one can choose better approximations like the Simpson's rule, exact for polynomials up to rank three, which perform better or equal for up to $N = 8$ atoms [71]. These methods however come with greater computational complexity, and only increase the threshold above which Monte Carlo based methods prevail. Monte Carlo methods should therefore be applied to few-body and many-body systems. For the sake of simplicity, we demonstrate our Monte Carlo approach below for $N = 2$, even though discretization techniques are faster at that dimensionality.

Finally, an analysis based on numerical samples mirrors experimental implementations, which also do not have access to the full momentum correlations. In experimental setups the momentum correlations are probed one experimental shot at a time. Observed errors and problems in Monte Carlo simulation results are hence more in line with what can be expected from experimental data.

In the original formulation, the aforementioned projection integrals from Eqs. (25) over the full momentum space contain the correlation function, the Fourier transformed Wannier envelope $|\tilde{w}(k_1, k_2)|^2$, and the respective trigonometric cosine or sine function,

$$\text{Re}(c_{\alpha\beta}) = \int \mathrm{d}k_1 \mathrm{d}k_2 \, \langle \hat{\text{n}}_\uparrow(k_1) \hat{\text{n}}_\downarrow(k_2) \rangle \cdot |\tilde{w}(k_1, k_2)|^2 \cdot \cos[d(\alpha k_1 + \beta k_2)], \tag{32a}$$

$$\text{Im}(c_{\alpha\beta}) = \int \mathrm{d}k_1 \mathrm{d}k_2 \, \langle \hat{\text{n}}_\uparrow(k_1) \hat{\text{n}}_\downarrow(k_2) \rangle \cdot |\tilde{w}(k_1, k_2)|^2 \cdot \sin[d(\alpha k_1 + \beta k_2)]. \tag{32b}$$

It is in principle possible to evaluate the full integrand through a crude uniform Monte Carlo sampling approach [72], but the momentum correlation function is highly peaked and the cosine and sine are oscillating functions. This causes a so-called sign problem, meaning that

the highly fluctuating integrand requires unattainable high sample numbers necessary for integral convergence. By instead treating the non-negative and normalized momentum correlation function as a multivariate random variable distribution and drawing samples from it, several goals can be achieved simultaneously. First, by going from a uniform random distribution to the momentum correlation function $\langle \hat{n}_\uparrow(k_1)\hat{n}_\downarrow(k_2)\rangle$, we can move the appearance of the latter in the integral into the differential of a new integration variable $G(k_1, k_2)$ as follows, $\mathrm{d}k_1\mathrm{d}k_2 \langle \hat{n}_\uparrow(k_1)\hat{n}_\downarrow(k_2)\rangle = \mathrm{d}^2G(k_1, k_2)$. The resulting integrals in their simplified form are thus given by

$$\mathrm{Re}(c_{\alpha\beta}) = \int \mathrm{d}^2G(k_1, k_2)\, |\tilde{w}(k_1, k_2)|^2 \cdot \cos[d(\alpha k_1 + \beta k_2)], \tag{33a}$$

$$\mathrm{Im}(c_{\alpha\beta}) = \int \mathrm{d}^2G(k_1, k_2)\, |\tilde{w}(k_1, k_2)|^2 \cdot \sin[d(\alpha k_1 + \beta k_2)], \tag{33b}$$

with trivial generalization to higher dimensions. The evaluations of the momentum correlation functions have effectively been shifted away from the integral itself to sample generation. In numerical simulations, much care has to be taken to deal with this problem accordingly, as the numerical complexity has not been decreased so far and the problem is just dealt with in another step of the computation. We give more detail on the sample generation step in the next section.

Quantum simulation experiments on the other hand work inherently different compared to numerical simulations. The quantum simulator does all necessary computations to produce real random samples of the needed momentum distribution $\langle \hat{n}_\uparrow(k_1)\hat{n}_\downarrow(k_2)\rangle$. All experimental samples can therefore be used directly for the integration, making the Monte Carlo formulation numerically more efficient. This demonstrates the built-in advantage of quantum simulators.

Moreover, there is another crucial side effect caused by the redefinition of the integration variables. The integration error is also proportional to the square root of the integrand's variance $\sigma_{\mathrm{MC}} \sim \sqrt{\mathrm{Var}}$ [72]. In the original formulation of the equations in Eqs. (32), the momentum correlation function fluctuates heavily and thus is a major contribution to said variance. Moving the correlation function to sample generation therefore decreases the variance and improves the convergence rate. The redefinition of the integration variable in Monte Carlo integration with the aim to reduce the variance is a common technique known as importance sampling [72]. Here, this effect coincides with our main goal of efficient integral computation through experimental data. We discuss the question of how the remaining integrand scales with the system size later in Sec. 6.2 in more Detail. In summary, applying Monte Carlo techniques gives better scaling at high dimensions compared to Newton-Cotes types methods while at the same time reducing computer memory requirements, making them the favorable choice in

this situation. The successful application depends on the efficient sample generation, which we discuss in the following.

4.2. Synthetic Data Generation

As discussed in the previous section, computation of projection integrals based on random samples is the only feasible way for the simulation of few-body and many-body systems. Experimentally, these samples are produced by measuring the actual momentum correlation function of the prepared quantum state through ToF expansion, but a way to efficient numerical sampling is *a priori* unclear. The distribution from which the samples are drawn, the momentum correlation function $\langle \hat{\mathrm{n}}_\uparrow(k_1)\hat{\mathrm{n}}_\downarrow(k_2)\rangle$, is known analytically. Each basis weight $g_{\alpha\beta}$ of the trigonometric basis functions can be extracted from the density matrix, and the corresponding frequencies are determined by the number of lattice sites (and later also by the number of atoms). For the larger systems investigated in this work (see Secs. 6 and 7), up to $\sim 3 \times 10^4$ individual frequency terms contribute to the momentum correlations. This results in a highly peaked functional landscape with structure sizes distributed over several orders of magnitude. A crude Monte Carlo Hit-or-Miss sampling approach which bounds the correlation function therefore yields very poor sample acceptance rates. But also more sophisticated variance reduction methods like the previously discussed importance sampling [72] face significant issues. The high number of trigonometric function contributions effectively hide the location of peak structures, which makes finding an appropriate transformation immensely challenging, especially in high dimensions.

We therefore follow a different approach and compute our synthetic data by iteratively computing the marginal probabilities for each atom. The marginal probabilities are obtained by integrating out all remaining unknown particle momenta except one, yielding a one-dimensional probability distribution. This function can then be discretized for subsequent sample generation. Once a sample has been drawn, the next marginal can be computed, now with one more fixed variable. By repeating this step, all momenta can be fixed, until a full sample of all atom momenta is obtained. This autoregressive sampling process is also know as ancestral sampling [73], referring to how each momentum k_i only depends on its ancestors $\{k_1, \ldots, k_{i-1}\}$.

We now develop a simple functional form of the marginal probability density function (pdf) for the two-atom case. After the derivation we give some comments how this derivation can be adapted to more atoms. The marginal probability density $p(k_1)$ of the first particle is obtained by integrating over the full phase space of the momentum of the second particle $k_2 \in \mathbb{R}$,

$$p(k_1) = \int \mathrm{d}k_2 \, \langle \hat{\mathrm{n}}_\uparrow(k_1)\hat{\mathrm{n}}_\downarrow(k_2)\rangle. \tag{34}$$

By inserting the expansion into trigonometric basis functions from Eq. (23a) into Eq. (34), one obtains

$$p(k_1) = \int \mathrm{d}k_2 \, |\tilde{w}(k_1, k_2)|^2 \left\{ \sum_{(\alpha,\beta)\in M} \mathrm{Re}(g_{\alpha\beta}) \cos[d(\alpha k_1 + \beta k_2)] - \mathrm{Im}(g_{\alpha,\beta}) \sin[d(\alpha k_1 + \beta k_2)] \right\}. \tag{35}$$

Next, one expands the trigonometric functions in terms of complex exponentials and pulls the terms containing k_1 out of the integral. We split the marginal pdf $p(k_1) = p_{\mathrm{Re}}(k_1) + p_{\mathrm{Im}}(k_1)$ as follows for the ease of notation,

$$\begin{aligned} p_{\mathrm{Re}}(k_1) = \sum_{(\alpha,\beta)\in M} \frac{\mathrm{Re}(g_{\alpha\beta})|\tilde{w}(k_1)|^2}{2} \Bigg[& \exp(id\alpha k_1) \int \mathrm{d}k_2 \, |\tilde{w}(k_2)|^2 \exp(id\beta k_2) \\ & + \exp(-id\alpha k_1) \int \mathrm{d}k_2 \, |\tilde{w}(k_2)|^2 \exp(-id\beta k_2) \Bigg], \end{aligned} \tag{36a}$$

$$\begin{aligned} p_{\mathrm{Im}}(k_1) = \sum_{(\alpha,\beta)\in M} \frac{-\mathrm{Im}(g_{\alpha\beta})|\tilde{w}(k_1)|^2}{2i} \Bigg[& \exp(id\alpha k_1) \int \mathrm{d}k_2 \, |\tilde{w}(k_2)|^2 \exp(id\beta k_2) \\ & - \exp(-id\alpha k_1) \int \mathrm{d}k_2 \, |\tilde{w}(k_2)|^2 \exp(-id\beta k_2) \Bigg]. \end{aligned} \tag{36b}$$

We note that the integral domains in Eqs. (36a) and (36b) are symmetric and that the Wannier envelope squared $|\tilde{w}(k_1)|^2$ is an even function due to the lattice symmetry. Using these properties and transforming the integration variable $k \coloneqq -k_2$, we obtain

$$\begin{aligned} p_{\mathrm{Re}}(k_1) = \sum_{(\alpha,\beta)\in M} \frac{\mathrm{Re}(g_{\alpha\beta})|\tilde{w}(k_1)|^2}{2} \Bigg[& \exp(id\alpha k_1) \int \mathrm{d}k \, |\tilde{w}(k)|^2 \frac{\exp(id\beta k) + \exp(-id\beta k)}{2} \\ & + \exp(-id\alpha k_1) \int \mathrm{d}k \, |\tilde{w}(k)|^2 \frac{\exp(-id\beta k) + \exp(id\beta k)}{2} \Bigg], \end{aligned} \tag{37a}$$

$$\begin{aligned} p_{\mathrm{Im}}(k_1) = \sum_{(\alpha,\beta)\in M} \frac{-\mathrm{Im}(g_{\alpha\beta})|\tilde{w}(k_1)|^2}{2i} \Bigg[& \exp(id\alpha k_1) \int \mathrm{d}k \, |\tilde{w}(k)|^2 \frac{\exp(id\beta k) + \exp(-id\beta k)}{2} \\ & - \exp(-id\alpha k_1) \int \mathrm{d}k \, |\tilde{w}(k)|^2 \frac{\exp(-id\beta k) + \exp(id\beta k)}{2} \Bigg]. \end{aligned} \tag{37b}$$

In the next step, we rearrange the exponentials to group terms containing k_1 and terms containing k together, which gives

$$p_{\mathrm{Re}}(k_1) = \sum_{(\alpha,\beta)\in M} \mathrm{Re}(g_{\alpha\beta})|\tilde{w}(k_1)|^2 \left[\frac{\exp(id\alpha k_1) + \exp(-id\alpha k_1)}{2} \cdot \int \mathrm{d}k\, |\tilde{w}(k)|^2 \frac{\exp(id\beta k) + \exp(-id\beta k)}{2} \right], \tag{38a}$$

$$p_{\mathrm{Im}}(k_1) = \sum_{(\alpha,\beta)\in M} -\mathrm{Im}(g_{\alpha\beta})|\tilde{w}(k_1)|^2 \left[\frac{\exp(id\alpha k_1) - \exp(-id\alpha k_1)}{2i} \cdot \int \mathrm{d}k\, |\tilde{w}(k)|^2 \frac{\exp(id\beta k) + \exp(-id\beta k)}{2} \right]. \tag{38b}$$

The above stated expressions can trivially be rewritten using trigonometric functions. Finally, by bringing the real and imaginary parts back together, we derive the final closed form of the marginal probability density function of the first momentum,

$$p(k_1) = \sum_{(\alpha,\beta)\in M} |\tilde{w}(k_1)|^2 \Big[\mathrm{Re}(g_{\alpha\beta}) \cos(d\alpha k_1) - \mathrm{Im}(g_{\alpha\beta}) \sin(d\alpha k_1) \Big] \int \mathrm{d}k\, |\tilde{w}(k)|^2 \cos(d\beta k). \tag{39}$$

For the purpose of sampling, it is convenient to transform the pdf into its corresponding cumulative distribution function (cdf) form. The cdf $P(k_1)$ is defined as the primitive function of $p(k_1)$, such that $P(k_1) \xrightarrow{k_1\to\infty} 1$. One can also define the cdf in terms of an integral equation given by

$$P(k_1) = \int_{-\infty}^{k_1} \mathrm{d}k\, p(k) \qquad \text{with } k_1 \in \mathbb{R},\ P(k_1) \in [0,1]. \tag{40}$$

Since probability density functions are strictly non-negative, cumulative distribution functions are monotonously growing. Any momentum $k_1 \in \mathbb{R}$ with non-vanishing probability can therefore unambiguously be mapped to a cdf value $P(k_1) \in [0,1]$. Numerically inverting $P(k_1)$ yields $P^{-1} : [0,1] \mapsto \mathbb{R}$, an unambiguous map from the interval $[0,1]$ to the real numbers. Evaluating $P^{-1}(x)$ at a uniform random variable x distributed like $X \sim \mathcal{U}[0,1]$ then yields a random variable distributed according to the marginal pdf $p(k_1)$ [74]. Since uniform (pseudo)random numbers like $X \sim \mathcal{U}[0,1]$ are easily produced on computers, this method can naturally be

implemented and yields a (pseudo)random variable correctly distributed according to $p(k_1)$, a method known as inversion sampling [75].

Once a sample of k_1 has been drawn, one can compute the conditional probability distribution $p(k_2|k_1)$ by simply fixing k_1 as shown below,

$$p(k_2|k_1) = \langle \hat{\mathrm{n}}_\uparrow(k)\hat{\mathrm{n}}_\downarrow(k_2)\rangle\Big|_{k=k_1 \text{ fixed}}. \tag{41}$$

The full sample of particle momenta is therefore generated iteratively. The first, unconditional distribution is universal for every sample and has to be computed only once. However, since the second distribution is conditional on k_1, $p(k_2|k_1)$ has to be recomputed for every drawn sample of k_1.

This iterative computation of marginal distributions can also be scaled up to higher particle numbers in the same way. One starts with the unconditional first probability density, which is computed by integrating over all other momenta $\{k_2, \ldots, k_n\}$. Once a sample for k_1 is produced, one can compute $p(k_2|k_1)$ by fixing k_1 and integrating over $\{k_3, \ldots, k_n\}$, and so on for the other marginals. This step can be iterated until all but the last momentum are fixed for the final marginal probability density. Figure 4 illustrates this behavior for a system of four particles. Every row represents the sampling process for one particle momentum with the pdf in the left column and the cdf in the right column. Each sampling process starts with the same distribution shown in Fig. 4(a); all subsequent distributions depend on the drawn explicit sample realizations (here exemplary shown through orange markers). The distributions become increasingly more peaked as more and more particle momenta are fixed and fewer allowed options are left for momentum realization.

4.3. Efficient Computation of Overlap Matrix $\boldsymbol{Q}$

At first glance, calculation of the basis overlap matrix $\boldsymbol{Q}$ [see Eq. (26)] is one of the most computationally complex tasks in the data post processing of this work. As defined above, the matrix contains the overlap integrals of the trigonometric basis of Eq. (23a). Each basis element is modulated by the Fourier transform of the Wannier envelope $|\tilde{w}(k_1, k_2)|^2$, which complicates the otherwise analytically accessible computations and makes this basis non-orthogonal. As a consequence, in general all matrix elements $\boldsymbol{Q}_{mn}$ can hold non-zero values. For the biggest system sizes with up to $N = 6$ atoms in a lattice of $L = 6$ sites, up to $\sim 3 \times 10^4$ basis elements have to be considered, resulting in $\mathcal{O}(10^9)$ matrix elements. The dimension of each of these integrals is equal to the particle number. Direct computation of $\mathcal{O}(10^9)$ 6-dimensional integrals takes up substantial resources and makes on-demand computation infeasible. We show in the

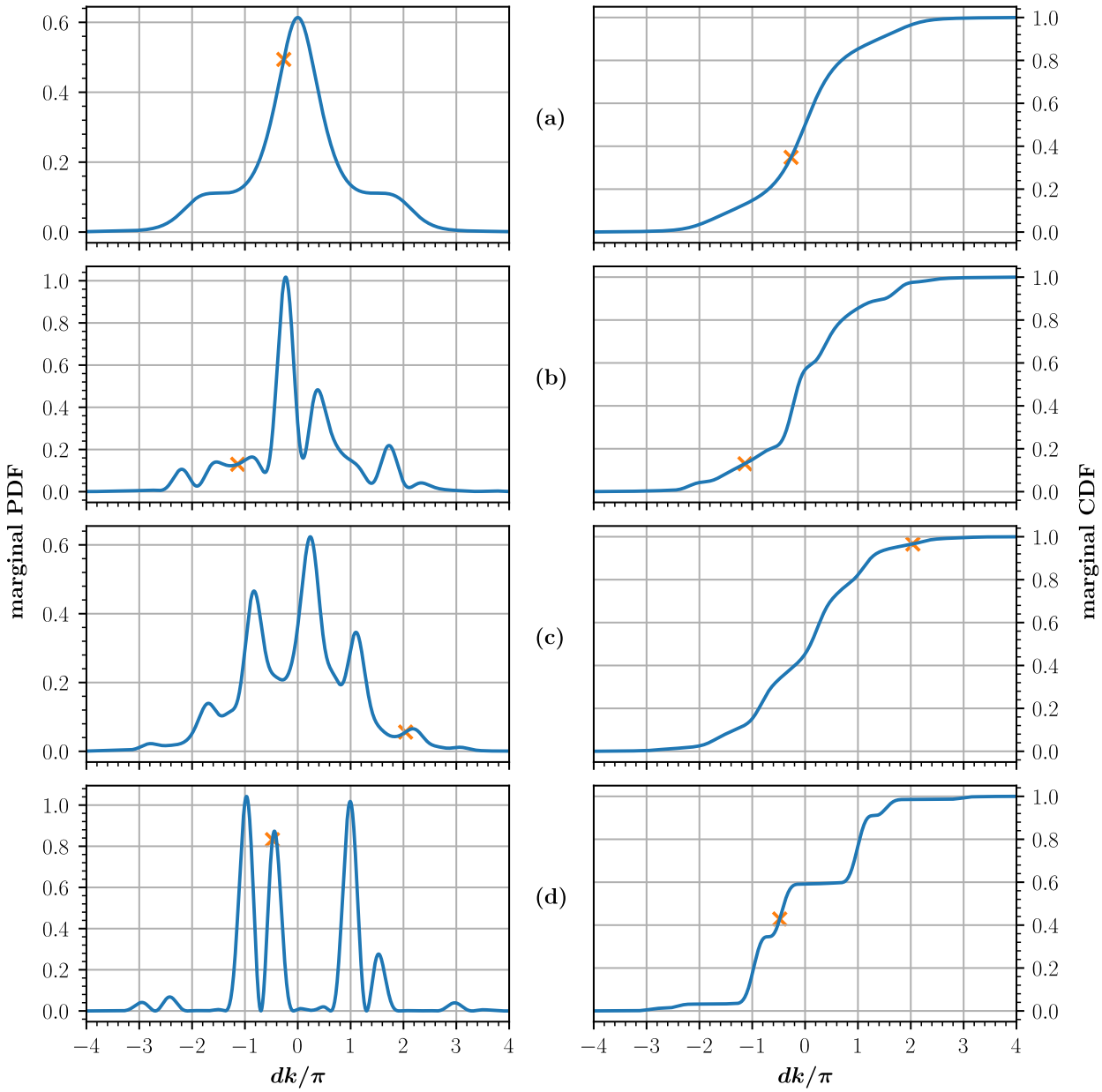

Figure 4: Examplary ancestral sample production for a system of four atoms. In every step [(a) to (d)] of the sampling process, one of the four momenta is drawn from the corresponding pdf on the left column. Each distribution depends on all previous samples (marked by the orange markers). This process is implemented using the related cdf $P(k)$ (right column). A random number x is drawn from $X \sim \mathcal{U}[0,1]$ and matched to a momentum through $P(k) = x \Rightarrow k = P^{-1}(x)$. The pdfs become more and more peaked the more momenta are fixed.

following that the integrals can be factorized into independent 1D integrals, which only need to be computed once.

There are three different types of overlap integral matrix elements that appear in $\boldsymbol{Q}$: Those with two cosine functions, those with two sine functions, and those with one cosine and one sine,

$$\boldsymbol{Q}_{mn}^{cc} = \int \mathrm{d}k_1 \mathrm{d}k_2 \, |\tilde{w}(k_1, k_2)|^4 \cos[d(\alpha k_1 + \beta k_2)] \cos[d(\alpha' k_1 + \beta' k_2)], \tag{42a}$$

$$\boldsymbol{Q}_{mn}^{ss} = \int \mathrm{d}k_1 \mathrm{d}k_2 \, |\tilde{w}(k_1, k_2)|^4 \sin[d(\alpha k_1 + \beta k_2)] \sin[d(\alpha' k_1 + \beta' k_2)], \tag{42b}$$

$$\boldsymbol{Q}_{mn}^{cs} = \int \mathrm{d}k_1 \mathrm{d}k_2 \, |\tilde{w}(k_1, k_2)|^4 \cos[d(\alpha k_1 + \beta k_2)] \sin[d(\alpha' k_1 + \beta' k_2)]. \tag{42c}$$

The above notation identifies state m with the coefficient pair (α, β) and state n with (α', β'). We begin with Eqs. (42a) and (42b) and split up the trigonometric functions into complex exponentials, which then read

$$\begin{aligned} \boldsymbol{Q}_{mn}^{cc} = \int \mathrm{d}k_1 \mathrm{d}k_2 \, |\tilde{w}(k_1, k_2)|^4 & \frac{\exp[id(\alpha k_1 + \beta k_2)] + \exp[-id(\alpha k_1 + \beta k_2)]}{2} \\ & \cdot \frac{\exp[id(\alpha' k_1 + \beta' k_2)] + \exp[-id(\alpha' k_1 + \beta' k_2)]}{2}, \end{aligned} \tag{43a}$$

$$\begin{aligned} \boldsymbol{Q}_{mn}^{ss} = \int \mathrm{d}k_1 \mathrm{d}k_2 \, |\tilde{w}(k_1, k_2)|^4 & \frac{\exp[id(\alpha k_1 + \beta k_2)] - \exp[-id(\alpha k_1 + \beta k_2)]}{2i} \\ & \cdot \frac{\exp[id(\alpha' k_1 + \beta' k_2)] - \exp[-id(\alpha' k_1 + \beta' k_2)]}{2i}. \end{aligned} \tag{43b}$$

By multiplying out the product and introducing $\alpha^+ = \alpha + \alpha'$ and $\alpha^- = \alpha - \alpha'$ with analogous

definitions for β^+ and β^- for brevity, we arrive at

$$\begin{aligned}\boldsymbol{Q}^{cc}_{mn} = \int \mathrm{d}k_1 \mathrm{d}k_2 \, \frac{|\tilde{w}(k_1,k_2)|^4}{4} \Big\{ &\exp\big[id(\alpha^- k_1 + \beta^- k_2)\big] + \exp\big[-id(\alpha^- k_1 + \beta^- k_2)\big] \\ &+ \exp\big[id(\alpha^+ k_1 + \beta^+ k_2)\big] + \exp\big[-id(\alpha^+ k_1 + \beta^+ k_2)\big] \Big\},\end{aligned} \tag{44a}$$

$$\begin{aligned}\boldsymbol{Q}^{ss}_{mn} = \int \mathrm{d}k_1 \mathrm{d}k_2 \, \frac{|\tilde{w}(k_1,k_2)|^4}{4} \Big\{ &\exp\big[id(\alpha^- k_1 + \beta^- k_2)\big] + \exp\big[-id(\alpha^- k_1 + \beta^- k_2)\big] \\ &- \exp\big[id(\alpha^+ k_1 + \beta^+ k_2)\big] - \exp\big[-id(\alpha^+ k_1 + \beta^+ k_2)\big] \Big\}.\end{aligned} \tag{44b}$$

We again utilize symmetry and apply the same transformation first used in Eq. (37) to see that the integrals do not depend on the sign of the exponentials. As a consequence, two integral pairs can be formed, evaluating to the same result, adding a factor of 2 in return. Each of the two remaining exponential terms can now be factorized and computed independently. Since the Fourier transform of the envelope also factorizes by construction, the integral decomposes into separate integrals for each momentum as follows,

$$\begin{aligned}\boldsymbol{Q}^{cc}_{mn} = &\frac{1}{2} \int \mathrm{d}k_1 \, |\tilde{w}(k_1)|^4 \exp\big(id\alpha^- k_1\big) \int \mathrm{d}k_2 \, |\tilde{w}(k_2)|^4 \exp\big(id\beta^- k_2\big) \\ &+ \frac{1}{2} \int \mathrm{d}k_1 \, |\tilde{w}(k_1)|^4 \exp\big(id\alpha^+ k_1\big) \int \mathrm{d}k_2 \, |\tilde{w}(k_2)|^4 \exp\big(id\beta^+ k_2\big),\end{aligned} \tag{45a}$$

$$\begin{aligned}\boldsymbol{Q}^{ss}_{mn} = &\frac{1}{2} \int \mathrm{d}k_1 \, |\tilde{w}(k_1)|^4 \exp\big(id\alpha^- k_1\big) \int \mathrm{d}k_2 \, |\tilde{w}(k_2)|^4 \exp\big(id\beta^- k_2\big) \\ &- \frac{1}{2} \int \mathrm{d}k_1 \, |\tilde{w}(k_1)|^4 \exp\big(id\alpha^+ k_1\big) \int \mathrm{d}k_2 \, |\tilde{w}(k_2)|^4 \exp\big(id\beta^+ k_2\big).\end{aligned} \tag{45b}$$

To simplify these integrals once more, we again use the symmetry of the domain and that $|\tilde{w}(k)|^4$ is even due to lattice symmetry to dismiss the odd part of the complex exponentials.

This only leaves real valued cosine terms,

$$\begin{aligned}\boldsymbol{Q}^{cc}_{mn} = &\frac{1}{2}\int \mathrm{d}k_1\, |\tilde{w}(k_1)|^4 \cos\big(d\alpha^- k_1\big) \int \mathrm{d}k_2\, |\tilde{w}(k_2)|^4 \cos\big(d\beta^- k_2\big) \\ &+\frac{1}{2}\int \mathrm{d}k_1\, |\tilde{w}(k_1)|^4 \cos\big(d\alpha^+ k_1\big) \int \mathrm{d}k_2\, |\tilde{w}(k_2)|^4 \cos\big(d\beta^+ k_2\big),\end{aligned} \tag{46a}$$

$$\begin{aligned}\boldsymbol{Q}^{ss}_{mn} = &\frac{1}{2}\int \mathrm{d}k_1\, |\tilde{w}(k_1)|^4 \cos\big(d\alpha^- k_1\big) \int \mathrm{d}k_2\, |\tilde{w}(k_2)|^4 \cos\big(d\beta^- k_2\big) \\ &-\frac{1}{2}\int \mathrm{d}k_1\, |\tilde{w}(k_1)|^4 \cos\big(d\alpha^+ k_1\big) \int \mathrm{d}k_2\, |\tilde{w}(k_2)|^4 \cos\big(d\beta^+ k_2\big).\end{aligned} \tag{46b}$$

The individual 1D integrals in Eqs. (46a) and (46b) depend only on the four different combinations $\alpha^+, \alpha^-, \beta^+\beta^-$ of the coefficients $\alpha, \alpha', \beta, \beta'$ of the two basis elements. The number of possible values these coefficients can take is small and depends only linearly on the size L of the lattice. There is no dependence on the number of atoms, as each additional atom simply results in more terms with $\gamma k_3, \delta k_4, \ldots$, which take the same values as $\alpha, \beta, \ldots$, and so on. It is hence efficient to compute all possible integrals $\int \mathrm{d}k\, |\tilde{w}(k)|^4 \cos(d\alpha^{\pm} k)$ once in the beginning and simply take the product of the results whenever needed for the computation of matrix elements.

Finally, we calculate the overlap $\boldsymbol{Q}^{cs}_{mn}$ between a cosine and a sine basis element. Mirroring our previous derivation, we expand the cosine and sine in exponentials,

$$\begin{aligned}\boldsymbol{Q}^{cs}_{mn} = \int \mathrm{d}k_1 \mathrm{d}k_2\, |\tilde{w}(k_1,k_2)|^4 &\frac{\exp[id(\alpha k_1 + \beta k_2)] + \exp[-id(\alpha k_1 + \beta k_2)]}{2} \\ &\cdot\frac{\exp[id(\alpha' k_1 + \beta' k_2)] - \exp[-id(\alpha' k_1 + \beta' k_2)]}{2i}.\end{aligned} \tag{47}$$

Two out of the four terms cancel out when the exponentials are multiplied out. This leaves

$$\begin{aligned}\boldsymbol{Q}^{cs}_{mn} &= \int \mathrm{d}k_1 \mathrm{d}k_2\, |\tilde{w}(k_1,k_2)|^4 \frac{\exp[id(\alpha^+ k_1 + \beta^+ k_2)] - \exp[-id(\alpha^+ k_1 + \beta^+ k_2)]}{4i} \\ &= \int \mathrm{d}k_1 \mathrm{d}k_2\, |\tilde{w}(k_1,k_2)|^4 \frac{\sin[d(\alpha^+ k_1 + \beta^+ k_2)]}{2} \\ &= 0,\end{aligned} \tag{48}$$

due to the integral of an odd and an even function over a symmetric domain. Thus, two basis elements have non-vanishing overlap if and only if they both are weighted by the real or the

imaginary part of their respective basis coefficient $g_{\alpha\beta}$ and $g_{\alpha'\beta'}$. Consequently, the real and imaginary parts effectively decouple and can be handled independently.

Although one can reduce the computational complexity significantly through the methods outlined above, it is clear that the number of matrix elements of $\boldsymbol{Q}$ still scales with the square of the local Hilbert space dimension of the system. For two atoms and L lattice sites, this corresponds to $N_{\boldsymbol{Q}} \sim L^2$ scaling, but for systems with $2N$ atoms, the scaling changes to $N_{\boldsymbol{Q}} \sim \binom{L}{N}^2$ (see Sec. 6). In the low density limit $N \ll L$, using Stirling's approximation, one can see that $N_{\boldsymbol{Q}} \sim L^{2N}/N!^2 \sim (eL/N)^{2N}/N$, so we indeed have exponential scaling in particle number and polynomial scaling in the lattice size for fixed N. Data for high particle numbers therefore remains prohibitively difficult to process, even though experimental access to these systems may be available.

5. Certification Robustness Under Realistic Experimental Conditions

In the following we apply our fidelity bounding scheme to a Fermi-Hubbard system of two atoms in an optical lattice of size $L = 6$. The goal of this section is to determine the robustness of our bound with respect to noise sources found in typical experimental environments. All numerical fit parameters referenced in this and the following sections are listed in Tab. 1 in appendix A. We choose a sufficiently deep lattice with $V_0 = 8E_r$ to be well within the tight-binding regime. The ground state of this configuration for attractive interactions ($U/J < 0$) has the maximum entanglement dimension $D_{\text{ent}} = 6$ and thus is a fitting test case for this entanglement detection scheme. We give a description of how such a state could be prepared in appendix B.

Through exact diagonalization we find that the fidelity of the ground state to the maximally entangled state $F(\rho, \Psi_{\text{MES}})$ [Eq. (17)] increases with growing attractive interaction (blue line in Fig. 5), but the ground state does not converge to Ψ_{MES} ($F(\rho, \Psi_{\text{MES}}) < 1$). For this configuration, knowing the available fidelity would enable us to certify 5 out of the 6 entanglement dimensions for moderately attractive interactions [$F(\rho, \Psi_{\text{MES}}) > \text{B}_5$ for $U/J \lesssim -6$]. The apparent fidelity offset is caused by the finite system size of the lattice: Populating central lattice sites is energetically favoured [see Fig. 6(a)].

The ground state therefore has a probability distribution which is significantly different compared to the flat double occupancy distribution of the maximally entangled state. We find that by artificially lowering the depth of the two outmost lattice sites for fixed U/J, this observed discrepancy between the two states can be reduced such that double occupation probabilities

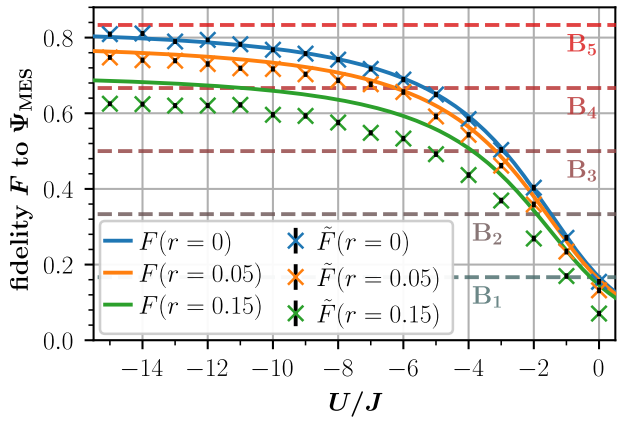

Figure 5: Scaling of the fidelity F and the fidelity bound $\tilde{F}$ for different interaction-to-tunneling-strength ratios U/J for pure ($r = 0$) and dephased ($r \in \{0.05, 0.15\}$) states. The B_k thresholds are the horizontal dashed lines such that fidelities above any B_k indicate at least $k+1$ dimensional entanglement. Both F and $\tilde{F}$ increase with growing attractive interaction strength before saturation. The tightness of $\tilde{F}$ decreases with increasing mixing rate r. All simulations are conducted at $L = 6$ with 2.5×10^4 momentum space and 1×10^4 position space samples.

are evenly spread between all sites [Fig. 6(b)]. At $U/J = -12$ we report that lowering the potential of the boundary sites by an energy shift of $\Delta E/J = -0.165$, the fidelity is increased from $F(\rho, \Psi_{\text{MES}}) = 0.787$ to $F(\rho, \Psi_{\text{MES}}) = 0.957$, which therefore raises the certifyable entanglement dimension to the maximal value of $D_{\text{ent}} = 6$. As pointed out earlier, only the fidelity bound is experimentally accessible, but for pure states we find our bound to be tight, as expected (blue markers in Fig. 5). Using our protocol therefore delivers the same tightness of certification as could be achieved with precise knowledge of the actual state fidelity F. We stress that the value obtained through the state fidelity does not necessarily coincide with the actual entanglement dimension, as the fidelity itself only delivers a lower bound.

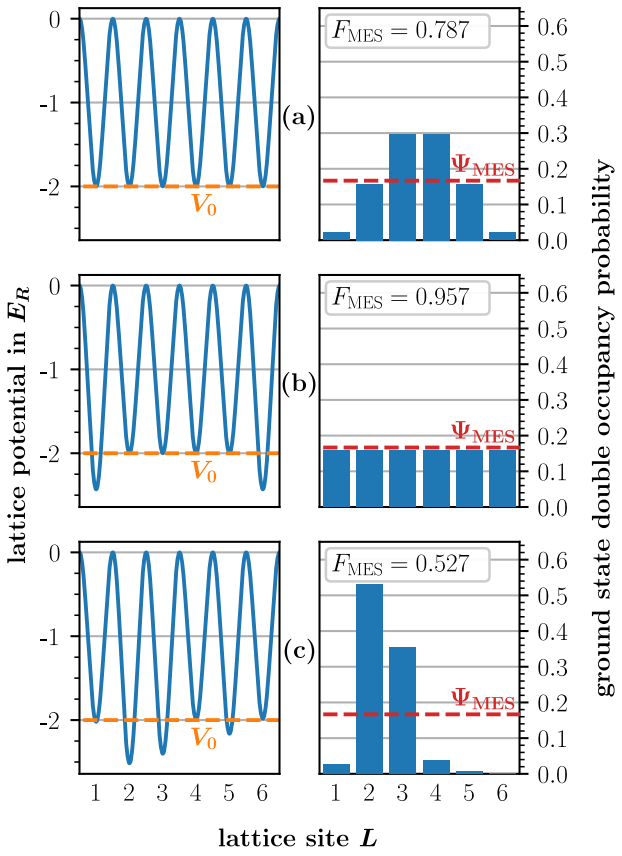

Figure 6: Lattice potential configurations for $L = 6$ in units of the recoil energy E_r (left) and the respective double occupancy probability distributions for the ground state (right) at $U/J = -12$. The dashed lines indicate the potential baseline depth V_0 (orange) and the uniform probability distribution of the maximally entangled state Ψ_{MES} (red). In all three cases the state has maximum entanglement dimension of $D_{\text{ent}} = 6$. **(a)** Even unaltered lattice potential. The same site population is heavily centered on the central lattice sites. One can certify up to $D_{\text{ent}} = 5$. **(b)** Lattice with increased potential depth at the outlying sites, resulting in a uniform distribution among all lattice sites and full certification of $D_{\text{ent}} = 6$. **(c)** Lattice with energy fluctuation $\Delta_E \sim \mathcal{N}(0, (0.08J)^2)$ on each lattice site. The same site population shows strong localization and is far away from Ψ_{MES}. Only $D_{\text{ent}} = 4$ can be certified.

In the following subsections we introduce three different error sources and imperfections during state preparation and measurements of $\tilde{F}$ and discuss their impact on our entanglement certification capabilities: Sampling statistics, dephasing noise, and fluctuations of the depth of individual lattice sites. We discuss the first two imperfections more generally in Secs. 5.1 and 5.2 as they are not specific to any explicit implementation of a quantum system but rather appear universally in quantum experiments. Lattice disorder on the other hand is the limiting system specific challenge for realizations with optical tweezer arrays, which we consider in Sec. 5.3. We conclude our investigation of the fidelity bound behaviour under real experimental

conditions with an analysis of the lattice size scalability in Sec. 5.4.

For the simulation results presented above in Fig. 5, we have already included the first two error sources, namely state dephasing and limited measurement statistics. Experimental realizations of quantum states are in general not pure states $|\psi_0\rangle$, but face mixing and decoherence. A simple model to account for this perturbation is to replace $|\psi_0\rangle$ with a dephased density matrix $\rho = (1-r) \cdot |\psi_0\rangle\langle\psi_0| + r \cdot L^{-2} \cdot \mathbb{1}$ with the mixing parameter r related to the state impurity $\bar{p} = 1 - p$, washing out the probability distribution. We simulate three different levels of dephasing in ground states here: No dephasing in blue ($r = 0$, $\bar{p} = 0$), light dephasing in orange ($r = 0.05$, $\bar{p} \approx 0.095$), and strong dephasing in green ($r = 0.15$, $\bar{p} \approx 0.270$). It is clear from the shown data that the asymptotic value for $F(\rho, \Psi_{\mathrm{MES}})$ decreases with growing dephasing for strongly attractive interactions ($U/J \to \infty$). Furthermore, the fidelity bound $\tilde{F}(\rho, \Psi_{\mathrm{MES}})$ also loses tightness, meaning that the certifiable entanglement dimension decreases even further. The second error, measurement statistics, is connected to the operative procedure of quantum experiments. There the joint momentum and position probabilities are each probed repeatedly and the full distributions are consecutively reconstructed from the samples. The accuracy of reconstruction depends on the available measurement statistics, and limited data introduces statistical fluctuations. This can be seen on the produced bound markers, especially for the pure ground state in blue. This data set has no bias, so the bound $\tilde{F}(\rho, \Psi_{\mathrm{MES}})$ is in principle tight. The markers, however, are distributed around the expected value of $F(\rho, \Psi_{\mathrm{MES}})$, with a standard error indicated by the error bars. We discuss the systematic effects of both errors in more detail in the following subsections.

5.1. Sampling Statistics

In experimental setups, both the joint position space distribution $\langle \mathrm{n}_\uparrow(x_1)\mathrm{n}_\downarrow(x_2)\rangle$ and the momentum space distribution $\langle \mathrm{n}_\uparrow(k_1)\mathrm{n}_\downarrow(k_2)\rangle$ are iteratively reconstructed by repeated sampling. Finite sample numbers are the cause of observed statistical errors in our fidelity bound calculation. In this section we systematically explore the scaling of the standard error of the mean of our bound $\tilde{F}(\rho, \Psi_{\mathrm{MES}})$ with regard to the sample size to determine how many samples are required for acceptable error margins. The position space distribution can be obtained directly in discretized form with L^2 different outcomes, whereas the momentum space distribution is continuous in k_1 and k_2 and needs to be processed via Monte-Carlo integration, demanding more samples. We therefore put special emphasis on the momentum distribution in the following and fix the number of position space samples to $N_{\mathrm{pos}} = 1 \times 10^4$.

To analyze scaling properties with regard to available measurement statistics, we compute the fidelity bound $\tilde{F}$ for a wide range of synthetic momentum space sample sizes N_{s}. The results for different values of $r \in \{0, 0.05, 0.15\}$ are presented in Fig. 7(a). The average of the

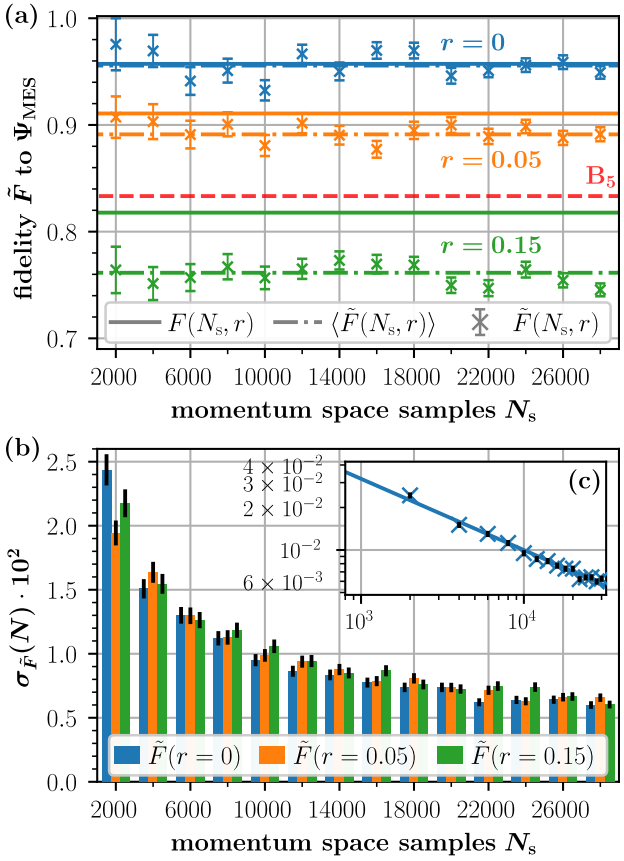

Figure 7: (a) Fidelity bound $\tilde{F}$ as a function of the number of momentum space samples for mixing strengths $r \in \{0,\ 0.05,\ 0.15\}$. The gap between the actual fidelity F (solid lines) and the fidelity bound average $\langle \tilde{F} \rangle$ (dash-dotted lines) increases with growing impurity. Each marker represents one sampling realization. **(b)** Dependency of the fidelity bound standard error of the mean $\sigma_{\tilde{F}}(N_s)$ on the number of momentum space samples N_s for mixing strengths $r \in \{0,\ 0.05,\ 0.15\}$ from (a). **(c)** Linear regression of log-log represented $\sigma_{\tilde{F}}(N_s)$ data for $r = 0$ from (b), demonstrating power law scaling. The simulations are conducted at $U/J = -12$ and 1×10^4 position space samples.

distribution (dash-dotted lines) coincides with the true state fidelity at $\bar{p} = r = 0$ (blue data set), but decreases with rising mixedness r. The standard error of the mean $\sigma_{\tilde{F}}(N)$ of the distribution for different impurities and sample numbers is shown in Fig. 7(b). We report no significant dependence of $\sigma_{\tilde{F}}(N_\mathrm{s})$ on the impurity and find a power-law behaviour with exponent $b = (-0.505 \pm 0.017)$ [Fig. 7(c), computed with the $r = 0$ data set]. This is consistent with the expectation of Monte Carlo error scaling $\sigma_{\mathrm{MC}} \sim 1/\sqrt{N_\mathrm{s}}$. We conclude that 1×10^4 position space samples and 1.2×10^4 momentum space samples are sufficient to reduce the standard error of the mean to $\sigma_{\tilde{F}} < 0.01$, independent on the state impurity.

When the fidelity lower bound is used to certify the entanglement dimension of the experimental state, statistical requirements for faithful certification solely depend on the distance to the next threshold value B_k. Fidelity bound values directly in the middle of two B_k lines maximize this distance and have the highest margin of error, whereas fidelities close to thresholds call for ever increasing sample sets to provide the needed accuracy. The measured bound value can be monitored on the fly to adapt the number of samples taken in order to fulfill statistical requirements.

Our data indicates that surprisingly low sample numbers can be sufficient for robust entanglement detection. For example, the distance to the next relevant threshold B_5 (red dashed line in Fig. 7(a) for the pure ground state at $U/J = -12$ is $\langle \tilde{F} \rangle - \mathrm{B}_5 > 5\sigma_{\tilde{F}}$, even at only $N_\mathrm{s} = 2000$

samples, a statistically significant statement. The fidelity to the MES drops with decreasing attractive interaction strength, and with it the distance to the next lower fidelity threshold. Sample set sizes should thus be increased for less attractive interaction strengths.

5.2. Quantum State Dephasing

We find linear dependencies between the mixing parameter r and both the fidelity F and fidelity bound $\tilde{F}$ (Fig. 8). The bound declines steeper with growing impurity than the actual state fidelity; the linear fit slopes are $a = -0.76$ (fidelity) in contrast to $\tilde{a} = -1.15 \pm 0.03$ (fidelity bound). Consequently, the tightness gap widens linearly with a slope of $a_{\text{Gap}} = 0.39 \pm 0.03$ with r. The state fidelity is not subjected to any random noise, so the fit errors are at floating point precision and can be neglected. Our bound certifies the same entanglement dimension as could be certified with the actual fidelity for most of the investigated impurity regime $r \leq 0.25$ and with only one dimension less in the regime $0.1 \lesssim r \lesssim 0.16$ (Fig. 8). These results show that tight certification of high-dimensional entanglement remains possible even for highly mixed states.

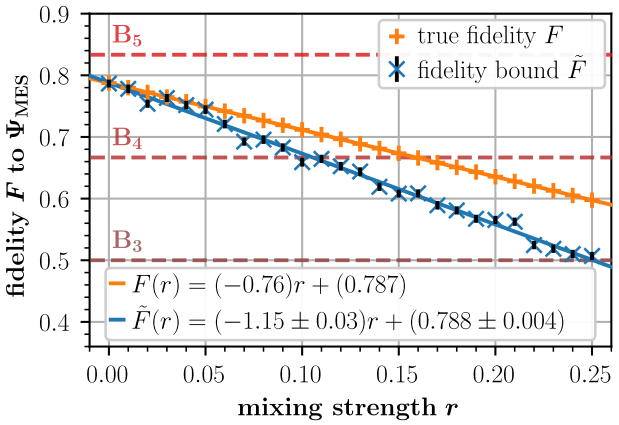

Figure 8: Systematic linear dependency of both F and $\tilde{F}$ on the state mixing parameter r at $U/J = -12$. Since the true fidelity F is not submitted to any noise sources, linear regression errors $[\mathcal{O}(1 \times 10^{-16})]$ are solely caused by machine precision and are omitted here. We use a lattice with $L = 6$ and generate 2.5×10^4 momentum space and 1×10^4 position space samples.

5.3. Lattice Potential Disorder

The third noise source we investigate is linked to imperfections in the lattice potential. This type of perturbation typically arises in experiments with arrays of optical tweezers, where the relative intensities, and thus depths, of the individual tweezer traps are difficult to stabilize. We introduce a modified Hamiltonian based on Eq. (15), which includes normally distributed potential depth fluctuation for each lattice site,

$$\hat{H}_{\Delta_V} = \hat{H} + \sum_i \Delta V_i (\hat{\mathrm{n}}_{i\downarrow} + \hat{\mathrm{n}}_{i\uparrow}) \,, \quad \Delta V_i \sim \mathcal{N}\left(0, \, (J\sigma_V)^2\right) , \tag{49}$$

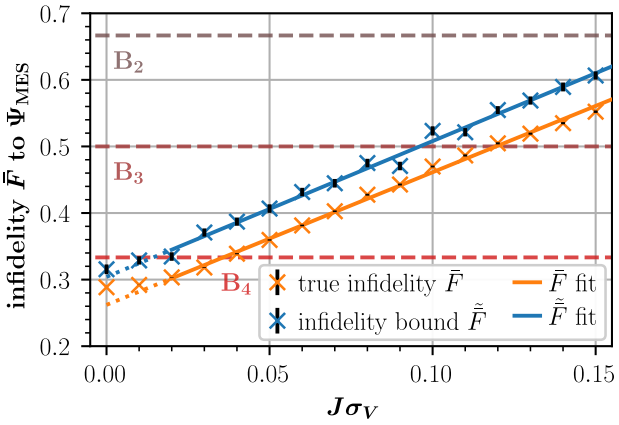

Figure 9: Scaling of the infidelity $\bar{F} = 1 - F$ as a function of the lattice depth standard deviation $J\sigma_V$ at a mixing strength of $r = 0.1$. Linear growth is found for both $\bar{F}$ and $\tilde{\bar{F}}$ for potential fluctuations with $J\sigma_V \geq 0.02$. Horizontal dashed lines indicate thresholds B_k reformulated in the infidelity picture, meaning $\bar{F} \leq B_k \Rightarrow D_{\mathrm{ent}} \geq k$. The simulation is conducted at $U/J = -12$ and 2.5×10^4 momentum space and 1×10^4 position space samples. Only data points contained in the solid part of the line are included in the fit.

with the tunneling strength J as energy scale. It should be noted that the fluctuations are modelled to be uncorrelated, a realistic assumption in the case of optical tweezer arrays, but not necessarily for optical lattices. The ground state of an imperfect array shows strong localization of the wave function and decreased fidelity to the reference state Ψ_{MES}, as seen in Fig. 6(c). There the composition of the localized state is quite different compared to that of Ψ_{MES} with two major and two smaller double occupation probabilities approximately equal to the square of the state's Schmidt coefficients λ_i. Even though significant differences exist, one can still certify an entanglement dimension of $D_{\mathrm{MES}} = 4$, corresponding to the four macroscopic components of the spectrum. This fact demonstrates the wide applicability of our method, as we can detect all significant components of the entanglement spectrum of a state not close to the reference. In particular, it allows us to track the reduction of entanglement due to disorder-induced pair localization, as we discuss in the following.

In the highly attractive regime of $U/J = -12$, the states with both atoms at the same lattice site have a contribution of 95.7% to the pure undisturbed ground state populations. It is therefore a reasonable simplification to treat the atom pair as a single quasiparticle placed in a lattice. The observed ground state localization is then in agreement with the predictions of Anderson localization for disordered potentials, where the occupation probability is exponentially suppressed when going away from the localization center [76]. For 3D systems, such localization appears for disorder strengths above a certain critical value E_c, but is always expected to manifest for lattices in 2D or 1D for any non-zero potential disorder [77]. The localization length heavily depends on the strength of disorder. To investigate the effect of lattice instability during state preparation on the state fidelity, we simulate state mixtures of 5000 individual disorder realizations configured according to Eq. (49). We find that the infidelity $\bar{F} = 1 - F$ of the prepared state grows linearly with increasing potential depth fluctuation $J\sigma_V$, shown in Fig. 9. The displayed errors are obtained through bootstrap sampling of the random ground

state configurations. Both $\bar{F}$ and $\tilde{\bar{F}}$ agree well with numerical fits with slopes $a_{\bar{F}} = 1.99 \pm 0.03$ and $\tilde{a}_{\bar{F}} = (2.04 \pm 0.06)$ for values $J\sigma_V \geq 0.02$. The slopes of both fits do not deviate significantly from each other. This means that even with strong disorder present in the system, our bound does not significantly loose tightness compared to a disorder free configuration. This is a remarkable result, as the investigated state is a mixture of thousands of individual disorder realizations. Furthermore, one can explain the constant difference $\Delta_F = 0.042 \pm 0.007$ between bound and true fidelity entirely through the mixing level of $r = 0.1$, yielding an expected contribution of $\Delta_{F\text{deph}} = 0.039 \pm 0.003$ (see Sec. 5.2). Consequently, our bound remains tight and certifies the same entanglement dimension or Schmidt number as the true fidelity for the majority of sample points. Deviations can reasonably be expected only in the direct vicinity of threshold crossings.

The breakdown of the fit at small disorder strengths can be ascribed to the finite size of the lattice. For very weak disorder, the localization length is greater or at the same order of magnitude as the lattice itself. In this regime, the infidelity therefore only grows slowly with increasing disorder strengths, until single disorder centers can be resolved at the scale of the lattice size. The $J\sigma_v = 0$ data point additionally marks the critical point of the localization phase transition in 1D, so anomalous behaviour fits to the applied Anderson localization picture. This indicates that small disorder strengths do not significantly decrease the fidelity $F(\rho, \Psi_{\text{MES}})$, and thus also our bound remains constant initially.

The simple linear trend in combination with the apparent certification robustness concerning disorder opens up another interesting use case of our fidelity bound: Disorder detection. If the dephasing strength in the experimental state can be estimated, one can gain insight if and how much the lattice potential is disordered. We note again that such assessments are possible, even though knowledge is gained with shot-to-shot changes in the random lattice disorder realizations. Furthermore, if the disorder can be controlled experimentally, one can even determine the disorder strength at which localization length and system size are comparable. This can be achieved by simply looking for the change in scaling behavior presented above.

5.4. Lattice Size Scaling

Scalability of entanglement certification with respect to the lattice size L is of significant concern for experimental implementations. With the aim to systematically investigate this dependency, we fix $U/J = -12$ and simulate $\tilde{F}(\rho, \Psi_{\text{MES}})$ for different lattice sizes. The results for a system with finite sampling statistics and dephasing noise again show power law decrease of the fidelity with growing lattice size, as shown in Fig. 10(a). The fidelities and fidelity bounds asymptotically approach constant values for $L \to \infty$, depending on the state mixing strength r. Consequently, certified entanglement dimensions continue to grow as $L \to \infty$. The

exponent b for the true fidelities F remains approximately constant with increasing mixing ratio, varying only between $b(r = 0) = -2.123 \pm 0.003$ and $b(r = 0.15) = -2.101 \pm 0.003$. Contrarily, a more significant spread can be found for the bounds $\tilde{F}$ with exponents between $\tilde{b}(r = 0) = -2.14 \pm 0.14$ and $\tilde{b}(r = 0.15) = -1.64 \pm 0.08$. The scaling behaviour of our bound thus depends on the level of dephasing.

The addition of lattice disorder complicates the system immensely. From previous data (see Sec. 5.3) we expect localization into dimers, but the dependence on the lattice size is not immediately evident. Our investigation of a lattice with fixed disorder $J\sigma_v = 0.05$ shows an exponential fidelity drop-off $\sim \exp(-bL)$ with scaling factor b. Again the scaling stays approximately constant for the true fidelity, fluctuating only between $b(r = 0) = 0.0523 \pm 5 \times 10^{-4}$ and $b(r = 0) = 0.0534 \pm 3 \times 10^{-4}$. On the other hand, one can see a trend in the bound scaling with $\tilde{b}(r = 0) = 0.0569 \pm 8 \times 10^{-4}$ and $\tilde{F}(r = 0.15) = 0.0735 \pm 6 \times 10^{-4}$ (Fig. 10(b)). All fits agree very well with greater lattice sizes, but significantly underestimate the fidelity in double and triple-well configurations. We explain this behavior with finite size effects: The localization length of the system is longer than the system itself for these very short lattice chains. One can therefore never resolve a localization center fully, and all sites carry non-vanishing populations, leading to higher fidelities.

Since the decision surfaces B_k scale like $\mathrm{B}_k \sim L^{-1}$ in contrast to the exponential fidelity scaling, the certified entanglement dimension decreases to $D_{\mathrm{ent}} = 1$ for $L \to \infty$. Consequentially, after an initial increase of certifiable entanglement, the entanglement dimension accessible through the bound starts to decline. Based on the reported fit we extrapolate a maximum certifiable entanglement dimension at a disorder standard deviation of $D_{\mathrm{ent}} = 7$ for pure states at $J\sigma_v = 0.05$ and of $D_{\mathrm{ent}} = 5$ for the $r = 0.15$ dephased state.

With above simulations we demonstrated that ordered and disordered lattices show significantly different behaviour when more and more lattice sites are added. This observation motivates again the usage of our bound $\tilde{F}(\rho, \Psi_{\mathrm{MES}})$ as an indicator of disorder. The differences between the two systems and with it the strength of our bound as a disorder witness gets more pronounced with increasing system size. Conversely, finite size effects prohibit this use case for smaller lattice configurations.

Finally, we consider the dependency of the standard error $\sigma_{\tilde{F}}(L)$ on the lattice size, again with fixed sample numbers. For this purpose we analyze the numerical resampling errors from Fig. 10(a); they are at display in Fig. 11. For lattice sizes $L > 2$, the standard error fluctuates around $\sigma_{\tilde{F}} \approx 4.5 \times 10^{-3}$, with no discernible differences between mixing rates r. The double-well configuration is a corner case of the model, as only one basis coefficient g_{11} is needed to extract the entanglement information. This fact in combination with the very small number of allowed modes and all coherences being on the same order of magnitude explains the smaller error size of $\sigma_{\tilde{F}} \approx 3.3 \times 10^{-3}$. The number of samples needed for some level of accuracy is

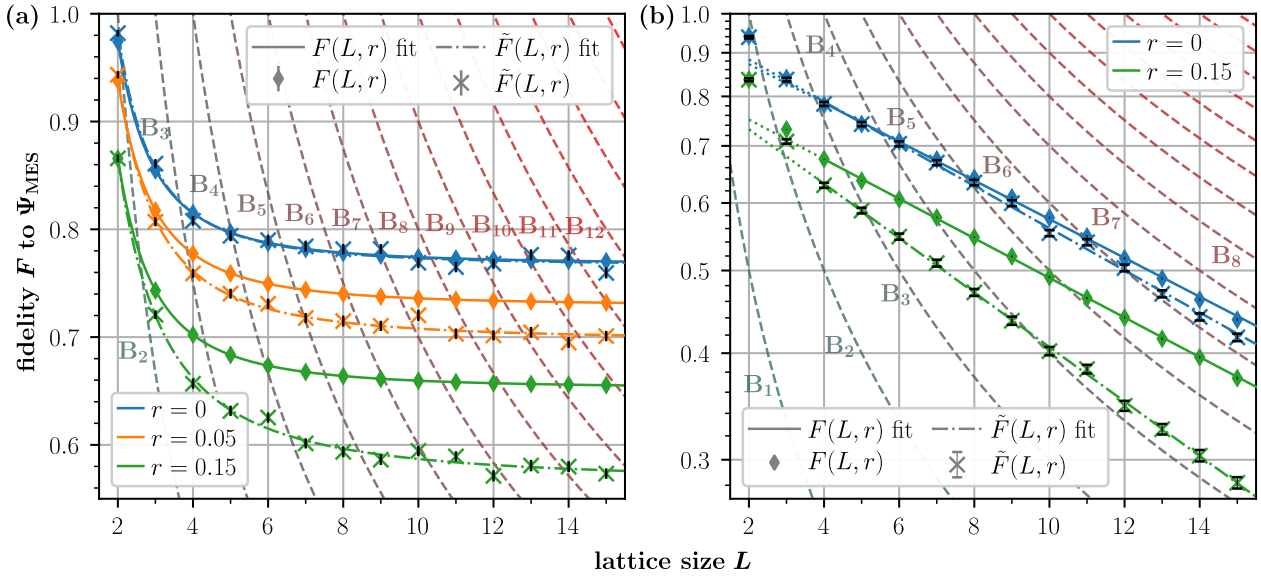

Figure 10: Lattice size dependency of the fidelity. **(a)** Scaling of the fidelity F of the ground state of a flat optical lattice as a function of the number of lattice sites L and the mixing parameter r. Numerical data including statistical noise fits well to power-law behaviour. The certifiable entanglement dimension continues to grow with increasing lattice size, as the fidelity asymptotically approaches its infinite system size value. **(b)** Log-linear plot of the fidelity for a disordered lattice of size L with fixed disorder strength $J\sigma_V = 0.05$, showcasing an exponential fidelity decay. The number of entanglement dimensions accessible to certification has a maximum of $D_{\mathrm{ent}} = 7$ before decreasing again with growing system size. The numerical fits have been computed using data points with $L \geq 4$ (non-dotted lines). Statistical error bars on the fidelity $F(L,r)$ are barely visible. Dashed lines indicate the entanglement dimension boundaries B_k. Both configurations are evaluated through 2.5×10^4 position space and 5×10^4 momentum space samples at $U/J = -12$.

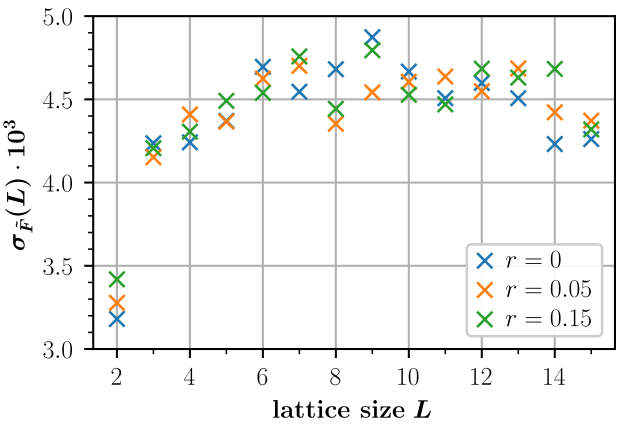

Figure 11: Scaling of the standard error of the fidelity bound $\tilde{F}(\rho, \Psi_{\mathrm{MES}})$ at fixed sample size for the mixing rates $r \in \{0, 0.05, 0.15\}$. Except for $L = 2$, we do not observe a clear data trend for any mixing rate. The data points displayed are the statistical errors from Fig. 10(a); the simulation is conducted at $U/J = -12$ with 5×10^4 momentum space and 2.5×10^4 position space samples.

thus largely independent of the size of the lattice; scaling up to bigger lattices is therefore not statistically prohibitive.

In summary, both pure state dephasing and lattice fluctuations cause a linear decrease of the true fidelity of the state F and of our fidelity bound $\tilde{F}$. Whereas the bound tightness is loosened by growing dephasing with a linear dispersion between F and $\tilde{F}$, it remains tight regarding lattice potential fluctuations. The statistical noise properties follow the expected Monte Carlo scaling $\sim 1/\sqrt{N_{\mathrm{sample}}}$; very moderate samples numbers of $\approx 1 \times 10^4$ both in momentum and position space are sufficient for all investigated lattice sizes. The bound is therefore robust in respect to typical noise sources and the entanglement certification capability is comparable to that of the true state fidelity; only linear correction terms apply.

6. Multiple Particles per Species

In the context of quantum simulation of condensed matter physics problems, the two-atom configuration discussed so far presents a somewhat unphysical low density limit. Eventually, one would like to access the entanglement structure near half filling (total atom number $2N$ equal to the number of lattice sites L) where true many-body effects emerge. However, our method still relies on the measurement of coefficients of a trigonometric basis, the size of which scales with the local Hilbert space size, so exponentially in particle number. The true many-body regime hence stays out of reach for the scheme presented in this work. Nonetheless, studies of few-body cold atom systems in the last decade have revealed that few-body dynamics approaches the many-body limit even at very moderate particle numbers [78, 79]. They are thus interesting candidates for quantum simulation and in extension entanglement certification, and give experimentalists capabilities beyond that of simpler two-particle systems like entangled photons. Recent success in the preparation and control of indistinguishable atom systems motivate this ansatz [80, 81]. In this section we extend our method to the case of multiple atoms per species and present numerical simulations of $2N = 4$ and $2N = 6$ atoms in total. We find that the needed measurement statistics remains manageable for small few-body systems, but grows rapidly for higher atom numbers.

6.1. Theoretical Considerations

Systems in which the number of atoms per species is increased to $N > 1$ can conveniently be described in a second quantization picture with different Fock modes. These modes are labeled by the particles' spin and their lattice positions, and are occupied by a given number of particles. For the fermionic atoms in the Fermi-Hubbard model, only one atom per spin state can populate each lattice site due to Pauli exclusion. The resulting dimension of the local Hilbert space, i.e. the Hilbert space available to each species, which determines the maximal entanglement dimension, changes to

$$D_{\text{ent}}^{\max} = L \xrightarrow[\text{per party}]{\text{N atoms}} \binom{L}{N}, \tag{50}$$

where L is the lattice size. A half filling configuration therefore maximizes the reachable entanglement dimension with $D_{\text{ent}}^{\max}(N = L/2) = L!/[(L/2)!]^2$, whereas a full lattice is described by only one contribution and thus has no interspecies entanglement. The wave function of the MES for a configuration filled with $N + N$ atoms, here shown for the case of $2 + 2$ atoms, becomes

$$|\Psi\rangle_{\mathrm{MES}}^{2+2} = \frac{1}{\sqrt{\binom{L}{N}}} \cdot \sum_{\substack{m_i,n_i=1 \\ m_i<n_i}}^{L} |m_{\mathrm{A}} n_{\mathrm{A}}\rangle \otimes |m_{\mathrm{B}} n_{\mathrm{B}}\rangle \,, \tag{51}$$

with normalization according to the Hilbert space size. In this notation $|m_{\mathrm{A}} n_{\mathrm{A}}\rangle \otimes |m_{\mathrm{B}} n_{\mathrm{B}}\rangle$ designates the Fock state where the two particles of species A occupy lattice sites m_{A} and n_{A} (with $m_{\mathrm{A}} < n_{\mathrm{A}}$) and the atoms of species B occupy sites m_{B} and n_{B}.

The general approach of bounding the fidelity to the MES to bound the Schmidt number remains the same. On the one hand, since still only two different species are present in the system, all experimental tools for single atom and spin resolved detection can still be applied. On the other hand, the theoretical framework has to change significantly to account for the indistinguishability within the subsystems. While state populations can be extracted in a straightforward extension to the two-atom case, the coherences in Eq. (20) are not accessible directly in the second quantization picture. The momentum correlation function now depends on $2N$ atom momenta, but the decomposition of a bipartite state used earlier is only well defined for two dimensions or two atom momenta. This apparent impasse can be overcome by changing to a first quantization interpretation where any Fock state contribution has several counterparts corresponding to label permutations. One can see this in the following example of two atoms per spin state with four terms in first quantization,

$$\begin{aligned} |13\rangle_{\mathrm{A}} \otimes |12\rangle_{\mathrm{B}} \xrightarrow{\text{1st. Quant.}} \frac{1}{2}(&|1\rangle_{\mathrm{A}_1} \otimes |3\rangle_{\mathrm{A}_2} \otimes |1\rangle_{\mathrm{B}_1} \otimes |2\rangle_{\mathrm{B}_2} - |1\rangle_{\mathrm{A}_1} \otimes |3\rangle_{\mathrm{A}_2} \otimes |2\rangle_{\mathrm{B}_1} \otimes |1\rangle_{\mathrm{B}_2} \\ &- |3\rangle_{\mathrm{A}_1} \otimes |1\rangle_{\mathrm{A}_2} \otimes |1\rangle_{\mathrm{B}_1} \otimes |2\rangle_{\mathrm{B}_2} + |3\rangle_{\mathrm{A}_1} \otimes |1\rangle_{\mathrm{A}_2} \otimes |2\rangle_{\mathrm{B}_1} \otimes |1\rangle_{\mathrm{B}_2}) \,, \end{aligned} \tag{52}$$

where explicit atom labels have been introduced on the right-hand side, keeping track of the possible permutations within the two subsystems A and B. The resulting wave function also has to be normalized with a factor of $(N!)^{-1}$ and antisymmetrized under atom exchange within each subsystem. The experimental detection of the state on the left-hand side of Eq. (52) can be interpreted as the detection of any of the states on the right-hand side with equal probability, as the labels are purely artificial and label exchange holds no physical meaning. Thus, through the inherent label exchange symmetry, any result measured in second quantization can be counted as a measurement for each of the first quantization populations, with proper normalization required. Applying this interpretation allows one to measure the momentum correlation function of all $2N$ atoms, $\langle \hat{\mathrm{n}}_\uparrow(k_{\mathrm{A}_1}) \dots \hat{\mathrm{n}}_\uparrow(k_{\mathrm{A}_N}) \hat{\mathrm{n}}_\downarrow(k_{\mathrm{B}_1}) \dots \hat{\mathrm{n}}_\downarrow(k_{\mathrm{B}_N}) \rangle$, which in turn can be described in a basis analogous to the two-body case [Eq. (23a)]. As the extraction of coherences is considerably more involved than before, we give a high level explanation of the procedure here; for a full mathematical description of a general $N + N$ atom configuration see appendix C.

Having measured the momentum correlation function of all $2N$ atoms, one must first identify the coherences contributing to $F(\rho, \Psi_{\mathrm{MES}})$. Since every state contribution in second quantization has $(N!)^2$ counterparts in first quantization ($N!$ permutations in each subsystem), each coherence therefore is represented by $(N!)^4$ different terms, each with the same absolute value. This value is connected to the corresponding coherence in second quantization by the normalization constant $(N!)^{-2}$ introduced in Eq. (52), which again is equal for all coherences. The absolute value of the second quantization coherences c^{2nd} can therefore be obtained straightforwardly as $|c^{\mathrm{2nd}}| = (N!)^2|c^{\mathrm{1st}}|$. Averaging over all available $(N!)^4$ coherences aides in the reduction of statistical noise. The fidelity bound is then constructed analogously to the two-atom case where the non-contributing coherences can be upper bounded through measurements of the state populations in second quantization.

Some comments regarding computational complexity are in order. Scaling up the system size requires significant computational resources, both for synthetic data generation and data processing. We in fact expect exponential scaling in both aspects; these issues are partly covered in Sec. 4, but we give closing comprehensive discussion of the matter in Sec. 8. But also the demands on the measurement statistics increase for systems with more atoms; here the scaling is not so clear. Our data processing is based on Monte Carlo techniques, which do not inherently scale with the number of atoms in the system, but scaling can be introduced through the variance of the joint momentum distribution. We investigate these statistical scaling properties in the following section.

6.2. Numerical Results

We simulated a configuration of 2+2 particles in a lattice of 5 sites, yielding a maximum entanglement dimension of $D_{\mathrm{ent}}^{\mathrm{max}} = \binom{5}{2} = 10$ [Eq. (50)]. To be able to relate the behaviour of this few-body system with that of two atoms, we repeat the interaction strength sweep shown in Fig. 5. Our numerical data shows that the fidelity to the MES for $U/J \to -\infty$ is lower by $\Delta F \approx 0.1$ depending on the level of dephasing, see Fig. 12(a), but is otherwise qualitatively comparable. This effect is another expression of Pauli exclusion: Atoms of the same species increase the distance between each other to not restrict tunneling pathways. Finite size effects on the other hand penalize occupation of outlying sites. Both effects combined lead to a very non-uniform distribution of dimer populations and the reduction in fidelity. Despite the lower fidelity, the maximum certifiable entanglement $D_{\mathrm{ent}} = 7$ realized for $U/J \lesssim -8$ exceeds the two-atom case due to higher density of entanglement dimension thresholds B_k. Consequentially, the gap between entanglement dimension certifiable through the bound and through the actual fidelity is wider for $2 + 2$ atoms.

For fixed interaction strength, it is again possible to increase the fidelity of the state by altering

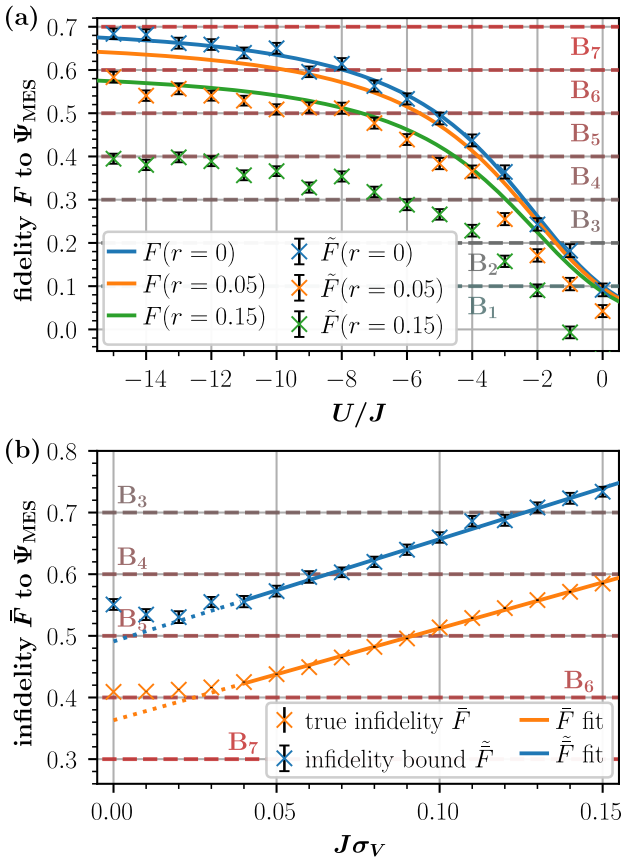

Figure 12: Numerical results for entanglement dimension certification of $2+2$ indistinguishable atoms in a lattice with $L = 5$. **(a)** Scaling of the fidelity F and the fidelity bound $\tilde{F}$ for different interaction-to-tunneling-strength ratios U/J for pure ($r = 0$) and dephased ($r \in \{0.05,\ 0.15\}$) states. **(b)** Scaling of the infidelity $\bar{F} = 1 - F$ as a function of the normalized optical lattice depth fluctuation $J\sigma_v$ at $r = 0.1$. The data is adequately described through a linear fit for $J\sigma_v \geq 0.04$ disorder strengths. Both simulations are conducted at an interaction-to-tunneling strength of $U/J = -12$ and an increased 5×10^4 momentum space and 2.5×10^4 position space samples.

the lattice potential. Since the local Hilbert spaces are no longer spanned by single atom states, but instead are described by a multiple atom basis, changing the potential of one lattice site affects several few-body contributions. This prevents precision changes to specific site double occupation probabilities, but we find that an overall improvement of fidelity from $F(\rho, \Psi_{\mathrm{MES}}) = 0.591$ to $F(\rho, \Psi_{\mathrm{MES}}) = 0.704$ at $U/J = -12$ and $r = 0.1$ is still possible. We achieved this by decreasing the potential depth on sites two and four by an energy offset of $\Delta E/J = 0.101$. The resulting fidelity is therefore expectedly lower than that achievable for a two-atom configuration on a lattice of equal size with $F(\rho, \Psi_{\mathrm{MES}}) = 0.867$.

With the introduction of disorder to the uniform lattice potential, localization effects can again be observed in the state populations. Like in the two-atom case, simulated infidelities $\bar{F}$ are well described through a linear fit in the strong disorder regime $J\sigma_V \geq 0.04$, as observed in Fig. 12(b). We find fit slopes $a = 1.49 \pm 0.02$ and $\tilde{a} = 1.66 \pm 0.05$, with a resulting small linear dispersion trend with slope $a_{\mathrm{Gap}}^{2+2} = 0.17 \pm 0.06$ between bound and true infidelity. Consequently, over the full range of the fit regime, our bound looses $\Delta\bar{F} \approx 0.02$ in tightness.

The linear regime is smaller than that reported for only two atoms, where all data with $J\sigma_v \geq 0.02$ follows linear growth. This can in parts be explained again with the localization length of the system. We investigate a smaller lattice ($L = 5$ in comparison to $L = 6$ for two atoms), and consequently only smaller localization lengths can be resolved. However, with the addition of

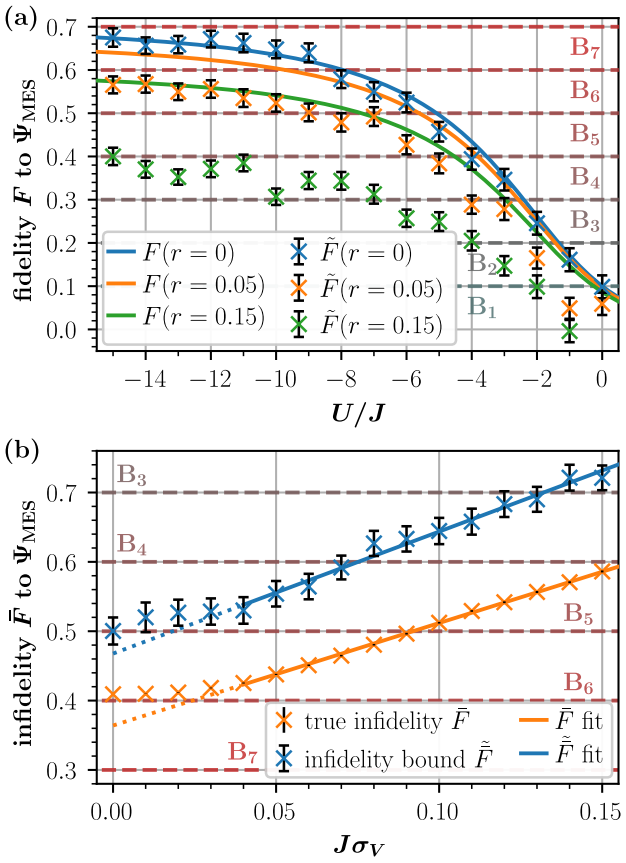

Figure 13: Numerical results for entanglement dimension certification of $3+3$ indistinguishable atoms in a lattice with $L=5$. **(a)** Scaling of the fidelity F and the fidelity bound $\tilde{F}$ for different interaction-to-tunneling-strength ratios U/J for pure ($r=0$) and dephased ($r \in \{0.05,\ 0.15\}$) states. **(b)** Scaling of the infidelity $\bar{F}=1-F$ as a function of the normalized optical lattice depth fluctuation $J\sigma_v$ at $r=0.1$. The data is adequately described through a linear fit for $J\sigma_v \geq 0.04$ disorder strengths. Both simulations are conducted at an interaction-to-tunneling strength of $U/J=-12$ and with an increased 1×10^5 momentum space and 5×10^4 position space samples.

two indistinguishable fermions, the internal structure of the wave function changes as well. Pauli exclusion forces the state populations to disperse over the whole lattice, and single localization centers do not impact the wave function so significantly anymore. The result is a regime of almost constant fidelity for weak to moderate disorder strengths.

We repeated the above simulations on the same lattice configuration with $L=5$, but now with $3+3$ atoms; the results are given in Fig. 13. The outcomes are qualitatively and quantitatively comparable, especially for the U/J sweep shown in Fig. 13(a). Our investigation of the disorder scaling shows a greater difference in the linear scaling with a dispersion of $a_{\mathrm{Gap}}^{3+3}=0.28\pm0.09$ [Fig. 13(b)]. Interestingly, there is no change in the size of the weak disorder regime, in which the infidelity and the bound deviate from the linear fitting model describing the behaviour at stronger disorder strengths. From the explanation applied above, one would expect this regime to extend to even higher disorder strengths, as at least three out of the five sites are occupied. The local dimension of this lattice however remains unchanged, as $D_{\mathrm{ent}}^{\max}=\binom{5}{3}=\binom{5}{2}=10$, due to the finite size of the lattice. We therefore conclude that finite size effects again suppress any further shift in infidelity.

The statistical errors of the $3+3$ atom case are increased by a factor of ≈ 2.2 with respect to the previous $2+2$ configuration, but we also doubled the position and momentum sample set size for the simulation. Disregarding the change in position sample size momentarily, one

can correct the error scaling using the Monte Carlo error $\sim 1/\sqrt{N_{\text{sample}}}$ to obtain an estimated increase of ≈ 3.1 for the standard error of the mean. On the other hand, going from $1 + 1$ atoms to $2 + 2$ while keeping the lattice size and the sample numbers fixed increases the standard error by a factor of ≈ 1.9. This indicates that adding a pair of atoms at least doubles the standard error of our fidelity bound, a strong indication of exponential scaling. On can compensate this effect by taking four times the sample size. It is therefore the number of atoms and not the local dimension which quantifies the expected statistical fluctuations in the experiment. A systematic analysis of bigger systems would be needed to make statistically significant quantitative statements about scaling in that regard.

Our analysis shows that entanglement certification is theoretically and experimentally possible for few particles per atomic species, without adding further experimental steps. The theoretical framework has to be extended by using a first quantization description to handle indistinguishability between the atoms. We certify up to $D_{\text{ent}} = 7$ in our lattice with $L = 5$. Simulation data indicates only shallow linear scaling of the bound tightness deviation with the disorder strength. Statistical errors on the other hand heavily depend on the number of atoms; our limited data suggest exponential growth of the standard error with the atom number. This approach is thus not scalable to the many-body regime, but configurations with a few atoms per species are realistically achievable.

7. Multipartite Entanglement

In the previous chapter we showed that when extend to few-body systems of multiple fermions per atomic species, our method still succeeds in the certification of high-dimensional entanglement with only small losses in bound tightness. This is a surprising result, considering the investigated state's inherent mixedness and complexity. Since only two spin states are populated, the system is fully described by the atom number N, the interaction strength U between atoms of the two states, and the tunneling strength J, so the same experimental toolbox can be used as for the initial two-atom fillings.

When instead more different hyperfine spin states are populated, a plethora of experimental and theoretical complications that have to be taken care of arise, but one gains the ability to certify genuine multipartite entanglement in return. In the following we first formulate the theoretical foundations needed for the classification of multipartite entanglement and then describe a possible setup for tripartite entangled states as a platform balanced between complexity gain and manageable experimental complications. Finally we present simulation results of entanglement certification for three atomic species in an optical lattice of five sites.

7.1. Multipartite Entanglement Foundations

Whereas bipartite entanglement of pure states is fully developed theoretically, many questions are still open concerning the characterization and certification of multipartite entanglement. For states consisting of three entangled parties, two sets of non-equivalent states sharing genuine tripartite entanglement have been identified, those equivalent under local operations and classical communication (LOCC) to the GHZ state and those LOCC-equivalent to the W state [5, 82, 83]. Because of this nonequivalence of entanglement, the Schmidt decomposition is no longer defined for general target states. Theoretical physicists therefore have to resort to different methods to obtain and describe the entanglement structure of multipartite quantum states. Numerous different approaches have been proposed to define canonical forms of tripartite and multipartite states with minimal number of non-zero coefficients. However, to uniquely define any given quantum state through these methods, a number of parameters significantly higher than the local Hilbert space dimension is required [57, 69, 84, 85]. For some states, most notably also for generalizations of the GHZ state to higher local dimensions,

$$|\psi\rangle_{\mathrm{ABC}} = \sum_{i=1}^{k} \lambda_i \, |i\rangle_{\mathrm{A}} \otimes |i\rangle_{\mathrm{B}} \otimes |i\rangle_{\mathrm{C}} \,, \tag{53}$$

the state contributions follow the same basic pattern of matching basis indices also found in the original Schmidt decomposition. No basis transformation can therefore reduce the number

of terms used for the representation of Eq. (53) any further [5, 86]. One can now define a multipartite entanglement dimension based on the above described non-reducibility with the properties of an entanglement monotone in analogy to that of bipartite states [87], also with a maximum value of $D_{\text{ent}}^{\max} = \dim \mathcal{H}_{\text{A}}$. A generalized GHZ state with equal contributions on all sites given by

$$|\Psi\rangle_{\text{MES}}^{\text{GHZ}} = \frac{1}{\sqrt{L}} \cdot \sum_{m=1}^{L} |mmm\rangle \tag{54}$$

therefore represents a suitable generalization of the maximally entangled state [Eq. (17)] as a reference state. It should be noted that this state is not maximally entangled in the sense that is has the maximum number of terms needed to represent general tripartite states, but rather has the highest number of terms possible for it to also have a generalized Schmidt decomposition.

The entanglement dimension of an experimental state ρ can be bounded by a set of fidelity thresholds B_k to that reference state analogous to Eq. (19), opening up in principle the same certification route taken for bipartite entanglement. We prove the existence of these bounds in appendix D. The extension of the algorithm [Eqs. (22a) to (29)] to include three or more atoms can be done in a direct way. For details see appendix E.

7.2. Experimental System Requirements

There are several different possible cold atom implementations in which multipartite entanglement can be realised. Here we choose a generalized Fermi-Hubbard system with three distinct atomic species. The interaction strength between two different spin states in Fermi-Hubbard system implementations is usually regulated through the use of a magnetic Feshbach resonance [33, 67]. When a third spin state is added to the system, each of the three possible atom pairs is now governed by their individual interaction strength U_{ij}. To experimentally realize control over a mixture of three different spin states similar to that possible over two atoms, an isotope with three overlapping Feshbach resonances connecting three low energy eigenstates can be used. One possible choice is ^{6}Li, for which Feshbach resonances for the three lowest energy states at 690, 811, and 834 G are experimentally accessible and have been realized before [88–90]. Since all three Feshbach resonances are magnetic, it is no longer possible to control the individual interaction strengths independently, but rather all three values U_{12}, U_{23}, and U_{13} are tuned at the same time through shifts of the external magnetic field. For field strengths up to 527 G all three scattering lengths are negative, delivering a broad regime of attractive interactions between all atom species. Preparation of states close to the aforementioned reference state [Eq. (54)] is thus in principle possible. A three-particle extension to the Hubbard model Hamiltonian can be constructed as [90],

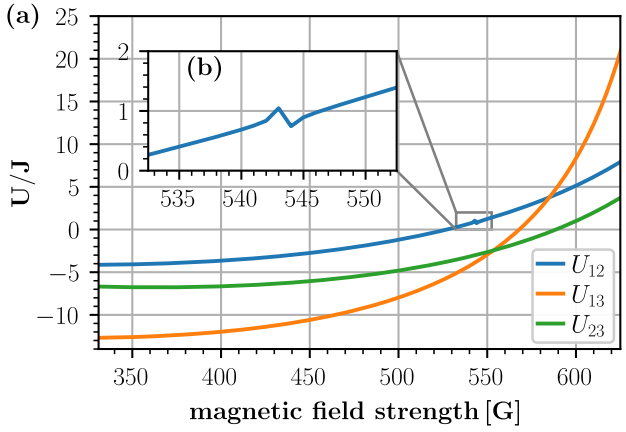

Figure 14: (a) Scaling of the three different interaction-to-tunneling-strength ratios U_{12}/J, U_{13}/J and U_{23}/J in dependence of the external magnetic field in Gauss based on [91] and gauged to fit experimental data published in [51]. **(b)** Magnification of the narrow s-wave Feshbach resonance at 543 G [92, 93].

$$H = -J \sum_{\sigma} \sum_{i,j} (\hat{c}^{\dagger}_{i,\sigma} c_{j,\sigma} + \text{h.c.}) + \sum_{\substack{\sigma_1,\sigma_2 \\ \sigma_1<\sigma_2}} \sum_{i} U_{\sigma_1\sigma_2} \hat{\text{n}}_{i,\sigma_1} \hat{\text{n}}_{i,\sigma_2} \,, \tag{55}$$

with $\sigma, \sigma_1, \sigma_2 \in \{1, 2, 3\}$ denoting the different hyperfine states.

We base our numerical simulation of tripartite entangled systems on precise scattering lengths for ^{6}Li published in reference [91]. From these measurements we derive U/J values for different magnetic field strengths gauged to fit the interaction strength data of U_{13} reported in [51] [Fig. 14(a)] to establish experimental comparability. This allows access to the interaction strength triplet for a wide field strength regime and thus enables one to repeat previous investigations for tripartite systems.

7.3. Numerical Results

To assess the effect of the new intricate triplet structure of interaction strengths, we perform a sweep across the accessible range of magnetic field strengths B. The result is presented in dependence of U_{13} in Fig. 15(a). All presented true fidelities $F(\rho, \Psi_{\text{MES}})$ are again computed through exact diagonalization of the Hamiltonian. The signal found at $U_{13} \approx -3.8J$ relates to a narrow s-wave Feshbach resonance at $B = 523\,\text{G}$ [magnified in Fig. 14(b)], which was earlier reported in references [92, 93]. The observed fidelities are of similar magnitude as values reported for the $2+2$ atoms configuration in Fig. 12(a), with slightly higher fidelity bounds for the tripartite configuration in the highly attractive regime ($\tilde{F}_{\text{TRI}} \approx 0.507 \pm 0.005$ in comparison to $\tilde{F}_{2+2} = 0.389 \pm 0.012$ at $U = U_{13} = -12$ and $= 0.15$).

In contrast to our findings for the configurations of indistinguishable atoms, we report a much stronger impact of lattice potential disorder on tripartite entangled states at the same interaction strength $U = U_{13}$. At $U/J = -12$ (which equals to $B = 399\,\text{G}$), $J\sigma_V = 0.02$, and $r = 0.1$, our simulation indicates a reachable fidelity bound of $\tilde{F}_{2+2} = 0.47 \pm 0.01$, whereas for the U/J

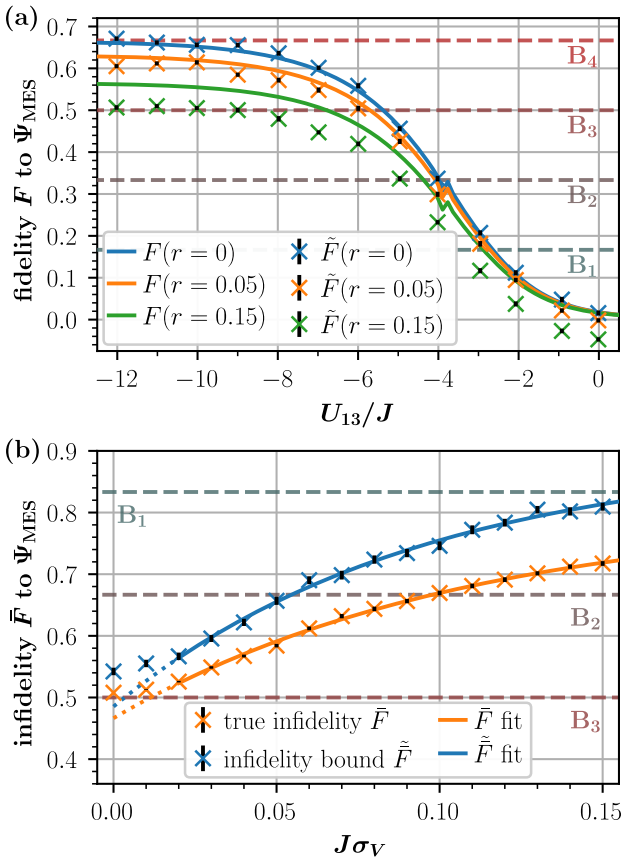

Figure 15: Numerical results for entanglement dimension certification of a tripartite state configuration in a lattice with $L = 6$. **(a)** Scaling of the fidelity F and the fidelity bound $\tilde{F}$ for different interaction-to-tunneling-strength ratios U/J for pure ($r = 0$) and dephased ($r \in \{0.05,\ 0.15\}$) states **(b)** Scaling of the infidelity $\bar{F} = 1 - F$ as a function of the normalized optical lattice depth fluctuation $J\sigma_V$ at $r = 0.1$ and $U_{13}/J = -6$. We report that the data is adequately described through an exponential fit approaching an asymptote for $J\sigma_v \geq 0.02$. Both simulations are conducted at an increased 5×10^4 momentum space and 1×10^4 position space samples. Only data in the solid part of the fit has been used for fitting.

triplet $U_{12} = -3.67$, $U_{13} = -12$, and $U_{23} = -6.66$ a fidelity of only $\tilde{F}_{\mathrm{TRI}} = 0.343 \pm 0.008$ is obtainable, a considerable regress. The three strongly attractive interaction strengths drive the atoms in triple-occupation states, which dominate the pure ground state at these values of U/J with 96.62% triple-occupation (trimers) and 3.35% double-occupation (dimers) contributions. In a lattice with non-vanishing disorder, the wave function therefore localizes solely around one or two lattice sites. Such bunching is prohibited for bipartite indistinguishable lattice fillings, where Pauli exclusion enforces a maximum of two atoms per site, see Sec. 6. Systems with weaker attractive interactions are not so heavily affected, as the atoms are not converging as strongly. This property comes at the cost of lower fidelity at very low disorder strengths, since single-occupation and double-occupation probabilities rise accordingly.

We therefore choose a more disorder-robust system and simulate a disorder strength sweep for a tripartite configuration at $U_{12}/J = -0.16$, $U_{13}/J = -6$, and $U_{23}/J = -3.91$ near the zero crossing of U_{12}/J, with the results displayed in Fig. 15(b). In contrast to all earlier investigated systems with linear dependencies, our simulation indicates exponential decay of the true fidelity and fidelity bound (or asymptotic exponential growth for the infidelities). We find numerical fits $\sim \exp(-bJ\sigma_V)$ with exponential scaling factor $b = 9.3 \pm 0.8$ for the true infidelity and $\tilde{b} = 10.6 \pm 1.3$ for our infidelity bound. However, for very small disorder strengths $J\sigma_v \leq 0.01$, one again observes deviation from the fit; the infidelities are higher than predicted. We suggest that the lack of Pauli exclusion in tripartite configurations is the cause of this behavior. It

is clear that the infidelities in all other configurations cannot continue to grow linearly for $J\sigma_v \to \infty$, as they are bounded by $\tilde{F} \xrightarrow{J\sigma_v \to \infty} 1$. The linear growth is therefore a valid description only for a finite disorder regime, after which asymptotic growth must set in. As discussed above, all three atoms can converge on the same lattice site, making the system more susceptible to localization effects. We therefore conclude that the simulated disorder regime simply includes a short growth phase in the beginning, well modeled through a linear fit, as well as asymptotic behavior for higher disorder strengths.

Over the course of the disorder interval under investigation, our bound again has a loss of $\Delta_{\tilde{F}} \lesssim 0.06$ in tightness. This value is slightly higher compared to the bipartite systems discussed above, but $\Delta_{\tilde{F}}$ still is much smaller than the distance between two adjacent fidelity thresholds $\mathrm{B}_{k+1} - \mathrm{B}_k$. Consequently, we do not expect the loss in tightness between the true fidelity and the fidelity bound caused by lattice fluctuations to decrease the certified dimension by more than one compared to the true fidelity. At vanishing disorder, robust certification of three-dimensional tripartite entanglement is possible, and for the highest simulated value $J\sigma_v = 0.15$, still two-dimensional tripartite entanglement is certified. We therefore witness multipartite entanglement for the entire investigated disorder regime. Even at high disorders, the contribution from lattice disorder to bound tightness is less or at the same order of magnitude than the contribution from state dephasing. However, the reduction in true fidelity through disorder dominates all other considered error sources. It should therefore be possible to experimentally observe trimer localization, if pure state dephasing can be brought under control. If the state dephasing gets too strong, it again becomes unclear if the observed low fidelity bounds are caused by localization or dephasing effects, unless full fidelity estimation measurements are conducted.

8. Conclusions

We presented a new method to bound the fidelity of few-body states of ultracold atom systems to a maximally entangled state. Large overlap or similarity between the two states indicates the presence of high-dimensional entanglement in the experimental state. The fidelity as a measure of that overlap can therefore be used to derive bounds on entanglement quantifiers of the experimentally realized state, such as the entanglement dimension or the entanglement of formation. Our approach requires only position and momentum space measurements, avoiding costly full state tomography. We provided a detailed study of the statistical significance and tightness of this bound under realistic assumptions about experimental measurement statistics and noise sources, showing that the experimental cost is manageable and the bound remains tight for certain classes of mixed states. Especially states highly mixed due to lattice potential fluctuation retain their bound tightness to a high degree. Dephasing noise has been identified to cause linear decline in tightness for our fidelity bound. Consequently, this bound can also be used as a witness of disorder in the lattice potential, utilizing the exponential scaling of the fidelity with regard to potential fluctuations. By including tailored modifications to the lattice potential, we were able to show that the maximal entanglement dimension can in principle be certified for pure ground states of this two-atom system. We extended our method to multipartite systems and configurations with several occupations per spin state, requiring adaptations to the coherence extraction framework. The impact of disorder on the few-body wave function depends heavily on the configuration of spin populations in the system. Bipartite systems are more robust and have linear scaling with disorder, whereas tripartite systems localize stronger with exponential scaling due to trimer formation. With these extensions and measures in place, our method gives experimentalists a powerful tool for the detection of entanglement and its structure in few-body systems.

Our research is placed among a long line of publications either working on more efficient state tomography schemes, or, leaving tomography out as a middle step, direct fidelity approximation methods. The need for such efficiency improvements is clear, as the number of different measurement bases necessary for a full state tomography is quadratic in local Hilbert space size, so that even single-digit particle numbers are enormously challenging to measure and process [94]. Much work has been invested in procedures based on compressed sensing [95, 96], a method that attempts state tomography with substantially fewer measurements based on classical techniques. It has already proven effective for experimental systems up to seven qubits [97]. Further alternatives are maximum likelihood estimation [98], Bayesian tomography methods [99], local measurement based readout schemes [100], or tomography based on artificial neural networks [101], among a plethora of others [102, 103]. For the direct approximation of the fidelity, variational methods [104] and random Pauli string measurements [105, 106] are noteworthy approaches. Almost all of these approaches work best for states ρ with low rank,

well described through matrix product states. These methods lose their numerical advantages in the strong presence of entanglement. It is precisely this regime for which we have developed our method; the number of necessary measurement repetitions is largely unaffected by the entanglement present in the state and explicitly works for highly entangled states.

In comparison to other experimental platforms, our method for cold atoms takes an approach based on accessible measurements that have been recently realized. In quantum optical setups, entanglement in photon pairs can be realized through different pairs of transverse propagation modes. Arbitrary spatial mode basis transformations can be readily implemented through the extensive experimental tool box of quantum optics. This gives experimentalists a more direct route to fidelity approximation that requires only the measurement in two MUBs [48]. Such a basis transformation of cold atom quantum states would require implementation of individually tuned tunneling strengths J_i, a highly non-trivial undertaking. We therefore see our method as a compromise between realistic experimental conditions and data processing simplicity.

In the following we briefly discuss model assumptions and discuss their validity in the investigated regime. In the construction of our bound, we assume negligible interactions during ballistic expansion. One can question this premise based on the non-zero scattering lengths, especially for multispecies scenarios as depicted in Fig. 14. This is especially significant in early stages of the expansion when atoms are not yet separated [24]. Rapid change of system parameters is known to cause excitation of higher energy bands [107], so speeding up the expansion phase is only viable within limits. Recent experiments for double-well and triple-well lattices have established experimental regimes in which these effects are restrained, but they should be studied in greater detail for potential experimental configurations [32, 80]. Similarly, assuming initial occupation of only the lowest energy band can be discussed depending on the lattice depth V_0. The band structure is gapped for $V_0 \geq 2.33E_r$ [24], so since our simulations were conducted at $V_0 = 8E_r$, neglecting other energy bands is a reasonable model choice.

Scalability is always one of the central concerns for methods and algorithms in quantum simulation; we therefore now summarize earlier findings and give some concluding remarks regarding that issue. One has to differentiate between three distinct aspects: The scaling of the sample size needed for sufficiently small statistical errors, the data processing complexity, and finally, the computational complexity of synthetic data generation. For the first part, we found no dependence of statistical errors on the lattice size L, but potentially exponential scaling with the particle number; here more data is needed. It is therefore clear that many-body systems remain out of reach for this method, but smaller few-body systems are feasible. We report that $\sim 1 \times 10^4$ samples in position and momentum space are enough to reduce errors to $\sigma_{\tilde{F}} \leq 0.01$ for systems of two atoms.

The data processing routine used in this work consists of several steps: Projection of the sampled momentum distribution onto modes of the momentum basis expansion, basis change via $\boldsymbol{Q}^{-1}$ to

correct for basis element overlap, and coherence extraction. We showed that the computational bottleneck of this approach is the computation of $\boldsymbol{Q}$, as its size scales exponentially with the atom number N. Furthermore, the number of basis coefficients we need to extract also scales exponentially with N, and the projection integral computation scaling depends on the suspected exponential scaling of statistical requirements regarding N as well. On the other hand, we demonstrated that the local Hilbert space size, and thus processing complexity, is only polynomial in the lattice size. It should be noted that the complexity of the entanglement spectrum itself scales with the local Hilbert space dimension, and so any procedure that extracts the spectrum has to have at least that scaling. We only extract the width of the spectrum, it is therefore unclear, if subexponential scaling can be achieved. Again, true many-body systems remain inaccessible to our method, but few-body systems, also in sizable lattices, can be processed as shown in this work.

Last, we consider synthetic data generation. We chose an autoregressive sampling strategy by sampling one momentum at a time, depending on all momenta sampled before. As a consequence, each distribution except for the first has to be computed on the fly. The number of contributions to the joint momentum distribution again scales exponentially in the particle number. Therefore, going to bigger system sizes adds significantly more complexity to the computation of the marginal momentum probability distributions. Synthetic sampling rates slow down accordingly, making computation on computer clusters advisable.

Experimental sampling on the other hand does not face this issue, since the hard computation is done on the quantum simulator device through ToF expansion. Imaging of momenta is then typically realized through fluorescence imaging, where all momenta of one atomic species are captured at a time. Subsequently, there is no inherent connection between sampling rate and system size, which allows a comparably much faster sample production in bigger few-body systems. This demonstrates that simulating the dynamics of few-body systems classically is a hard problem; using quantum hardware instead is more efficient and yields better sampling rates.

Building upon the results shown here, it is a promising idea to apply the concept of measuring in two complementary bases to other physical platforms with periodic properties. Trapped ions are a potential candidate for implementation, as control and readout mechanisms show similarities to cold atoms in periodic optical lattices. But other basis pairs might also offer new approaches to certify entanglement in different systems. Alternatively, pushing the certification scheme even further and investigating multipartite systems with several occupations per atomic species is another interesting research question to look for emerging many-body behaviour.

Acknowledgements

First and foremost, I want to thank my supervisor Martin Gärttner for his ever helpful and motivating support of this work. Furthermore, I thank Philipp Preiss and Selim Jochim for many interesting discussions concerning experimental aspects and Adrian Braemer for his valuable comments on the theory sections of this thesis. I acknowledge support by the state of Baden-Württemberg through bwHPC and the German Research Foundation (DFG) through grant no INST 40/575-1 FUGG (JUSTUS 2 cluster).

A. Fitting Parameters

Table 1: Table of fitting parameters

Fig.	Description	Fitting Model	Fitting Parameters		
			a	b	c
7(c)	Sampling Statistics	$\sigma_{\tilde{F}}(N_\mathrm{s}) = aN_\mathrm{s}^b$	$1.04^{+0.18}_{-0.16}$	-0.505 ± 0.017	-
8	Dephasing F	$F(r) = ar + b$	-0.76 ± 2e-16	0.787 ± 3e-17	-
	Dephasing $\tilde{F}$		-1.15 ± 0.03	0.788 ± 0.004	-
9	Disorder $\bar{F}$	$\bar{F}(\sigma) = a\sigma + b$	1.99 ± 0.03	0.262 ± 0.002	-
	Disorder $\bar{\tilde{F}}$		2.04 ± 0.06	0.304 ± 0.006	-
10(a)	Order $F\,(r = 0.00)$	$F(L) = aL^{-b} + c$	0.902 ± 0.002	2.123 ± 0.003	0.767 ± 6e-5
	Order $\tilde{F}\,(r = 0.00)$		0.95 ± 0.09	2.14 ± 0.14	0.766 ± 0.003
	Order $F\,(r = 0.05)$		0.906 ± 0.002	2.115 ± 0.003	0.729 ± 6e-5
	Order $\tilde{F}\,(r = 0.05)$		0.94 ± 0.06	1.94 ± 0.09	0.697 ± 0.003
	Order $F\,(r = 0.15)$		0.916 ± 0.002	2.101 ± 0.003	0.652 ± 5e5
	Order $\tilde{F}\,(r = 0.15)$		0.93 ± 0.05	1.64 ± 0.08	0.565 ± 0.005
10(b)	Disord. $F\,(r = 0.00)$	$F(L) = ae^{-bL}$	0.969 ± 0.005	0.0523 ± 5e-4	-
	Disord. $\tilde{F}\,(r = 0.00)$		0.990 ± 0.008	0.0569 ± 8e-4	-
	Disord. $F\,(r = 0.05)$		0.926 ± 0.005	0.0523 ± 6e-4	-
	Disord. $\tilde{F}\,(r = 0.05)$		0.946 ± 0.010	0.0621 ± 0.0012	-
	Disord. $F\,(r = 0.15)$		0.836 ± 0.002	0.0534 ± 3e-4	-
	Disord. $\tilde{F}\,(r = 0.15)$		0.848 ± 0.005	0.0735 ± 6e-4	-
12(b)	$2+2$ disord. $\bar{F}$	$\bar{F}(\sigma) = a\sigma + b$	1.49 ± 0.02	0.362 ± 0.002	-
	$2+2$ disord. $\bar{\tilde{F}}$		1.66 ± 0.05	0.491 ± 0.005	-
13(b)	$3+3$ disord. $\bar{F}$	$\bar{F}(\sigma) = a\sigma + b$	1.478 ± 0.015	0.3640 ± 0.0013	-
	$3+3$ disord. $\bar{\tilde{F}}$		1.76 ± 0.08	0.468 ± 0.008	-
15(b)	Tripartite disord. $\bar{F}$	$\bar{F}(\sigma) = ae^{-b\sigma} + c$	-0.366 ± 0.011	9.3 ± 0.8	0.802 ± 0.014
	Tripartite disord. $\bar{\tilde{F}}$		-0.412 ± 0.015	10.6 ± 1.3	0.897 ± 0.022

B. Preparation of High-Dimensional Entanglement

One can test the entanglement certification protocol presented in this work by applying it to a highly entangled state as a benchmark and reference point. To ensure rapid experimental repetition rates, such a state should be preparable within a short period of time compared to typical experimental lifetimes in the order of seconds to even minutes [24, 62, 108]. Furthermore, the preparation should require as few steps to realize as possible in order to streamline the process and reduce noise sources. We offer here one possible scheme to produce such a state of two atoms in an optical tweezer array. Our simulations of a lattice with $L = 5$ indicate that fidelities to the maximally entangled state of theoretically up to $\sim 95\%$ are possible through this protocol. In the following we outline the necessary experimental steps in more detail.

One starts with both atoms loaded in the same deep optical tweezer. This trap will later act as the central lattice cite of the array. In the beginning of the ramp, all other tweezers are tuned to have a very shallow potential such that tunneling away from the initial site is heavily suppressed. By slowly lowering down all other trap potentials to the level of the central site, the quantum state can be transferred adiabatically to the ground state of the final tweezer array configuration. The two outlying sites can optionally be lowered even further to produce a flat dimer population distribution; we apply this technique here for even higher fidelities.

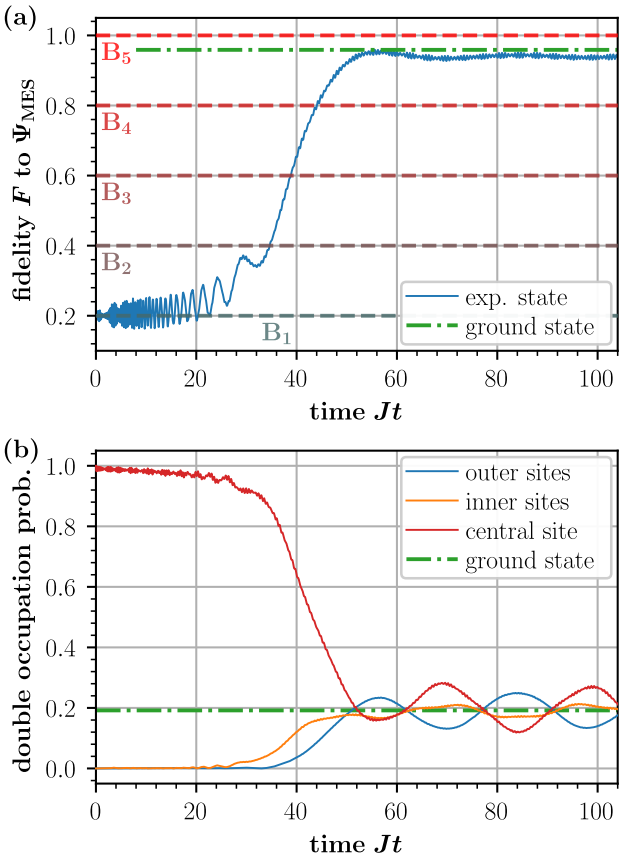

Figure 16: Adiabatic ramp close to the ground state for a lattice of size $L = 5$. **(a)** Fidelity $F(\rho, \Psi_{\mathrm{MES}})$ of the experimentally realized state ρ to the maximally entangled state Ψ_{MES}. The approximate level of the ground state is reached after $t \approx 55.6/J$, with small oscillations afterwards. **(b)** Double occupancy probability for the central site and for each of the inner and outer sites, respectively. Initially only one atom tunnels away from the central site, but eventually both atoms oscillate as a dimer between boundary and center sites.

However, such an ideal loading procedure can only be approximately reached in real experiments, as the energy gap between ground and first excited state approaches zero at the same time as the difference in potential depth between the central and the adjacent sites vanishes. Every realistic imperfect preparation scenario therefore inevitably leads to energy transfer and subsequent excitation of higher states in the system.

One potential ramp process is depicted in Fig. 16. The initial fidelity in Fig. 16(a) is low at $F(\rho, \Psi_{\mathrm{MES}}) \approx 0.2$, as the atoms both occupy one out of the five potential lattice sites. Up until $Jt \leq 30$, the fidelity begins oscillating rapidly, as energy is pumped into the system through the ramp of the microtraps. However, by looking at the dimer populations displayed in Fig. 16(b), it is clear that no significant shift of dimer population to other sites takes place in that time frame. Still, the central dimer population diminishes, meaning that first only one of the atoms starts to oscillate between the central sites and adjacent sites. After these initial single-particle oscillations, dimer population start to form again on the adjacent sites, and with some time delay also on the outlying sites. Simultaneously, one observes a sharp increase of $F(\rho, \Psi_{\mathrm{MES}})$, as the double occupation probability distribution rapidly approaches an even spread. It reaches its maximum at $t \approx 55.6/J$, after which the fidelity stays almost constant at $\sim 90\% - 95\%$. Dimer populations on the other hand show different dynamics: The dimer populations oscillate between the central site and the outlying sites, with the time average of each site corresponding approximately to the ground state expectation value. We can therefore conclude that this scheme produces a highly entangled state close to the ground state of the lattice.

C. Details on Indistinguishable Atom Bipartite Entanglement Certification

Here we give a more rigorous description on how to extract the relevant coherences from the full $2N$-particle momentum correlation function. The state populations of the Fock states can be measured directly in situ and pose no additional theoretical challenges in comparison to the process outlined in Sec. 3. Single particle resolved imaging is challenging for higher atom numbers, but experimental tools available today allow for high-fidelity measurements in the few-body regime [81]. We therefore omit their contributions here and focus on the coherence part of the fidelity $\tilde{F}_{\mathrm{coh}}$. The aim of this appendix is to give the mathematical framework needed for indistinguishable particle coherence extraction in a way that can be easily implemented for actual data processing. In the experiment the corresponding correlation function $\langle \hat{\mathrm{n}}_\uparrow(k_{\mathrm{A}_1}) \dots \hat{\mathrm{n}}_\uparrow(k_{\mathrm{A}_N}) \hat{\mathrm{n}}_\downarrow(k_{\mathrm{B}_1}) \dots \hat{\mathrm{n}}_\downarrow(k_{\mathrm{B}_N}) \rangle$ is obtained by probing the wave function after free ToF expansion, which subjects the many-body quantum state to an effective Fourier transformation. To understand its effect on the density matrix ρ, each of the $2N$ individual components of the tensor product wave function have to be explicitly labeled and transformed. The resulting formula is given in Eq. (C.1a) and contains a sum over all ket state site indices of both subsystems a_i', b_i' and their bra state counterparts a_i, b_i. Each coherence is multiplied with their individual weight function $\phi_{a_1 \dots b_N'}(k_{\mathrm{A}_1}, \dots, k_{\mathrm{B}_N})$ [Eq. (C.1b)], containing the $2N$-dimensional Fourier transformed Wannier envelope $|\tilde{w}(k_{\mathrm{A}_1}, \dots, k_{\mathrm{B}_N})|^2$, and a phase factor. The latter stems from the translation of the Wannier envelope in position space for different lattice sites and the fact that $\mathcal{F}[g(x-\delta)] = \tilde{g}(k) \cdot \exp\{-ik\delta\}$ for any integrable function $g(x)$. The full relation between the density matrix elements and $\langle \hat{\mathrm{n}}_\uparrow(k_{\mathrm{A}_1}) \dots \hat{\mathrm{n}}_\uparrow(k_{\mathrm{A}_N}) \hat{\mathrm{n}}_\downarrow(k_{\mathrm{B}_1}) \dots \hat{\mathrm{n}}_\downarrow(k_{\mathrm{B}_N}) \rangle$ is thus given as

$$\langle \hat{\mathrm{n}}_\uparrow(k_{\mathrm{A}_1}) \dots \hat{\mathrm{n}}_\uparrow(k_{\mathrm{A}_N}) \hat{\mathrm{n}}_\downarrow(k_{\mathrm{B}_1}) \dots \hat{\mathrm{n}}_\downarrow(k_{\mathrm{B}_N}) \rangle = \sum_{\substack{a_1,\dots,a_N,b_1,\dots,b_N=1 \\ a_1',\dots,a_N',b_1',\dots,b_N'=1}}^{L} \phi_{a_1 \dots b_N'}(k_{\mathrm{A}_1}, \dots, k_{\mathrm{B}_N}) \cdot \langle a_1, \dots, b_N | \, \rho \, | a_1', \dots, b_N' \rangle \,, \tag{C.1a}$$

$$\phi_{a_1 \dots b_N'}(k_{\mathrm{A}_1}, \dots, k_{\mathrm{B}_N}) = |\tilde{w}(k_{\mathrm{A}_1}, \dots, k_{\mathrm{B}_N})|^2 \cdot \exp\left(-id \cdot \sum_{i=1}^{N} (a_i - a_i') k_{\mathrm{A}_i} + (b_i - b_i') k_{\mathrm{B}_i} \right). \tag{C.1b}$$

This sum can also be decomposed into trigonometric functions of the $2N$ momenta of all atoms as shown in Eq. (C.2a). The basis consists of pairs of matching cosine and sine functions, where each pair is uniquely identified by a set $(\alpha_1, \dots, \alpha_N, \beta_1, \dots, \beta_N) \in M$ defining one possible lattice site gap configuration for the $2N$ atoms in the system. The basis function pairs are weighted through their coefficients $\mathrm{Re}(g_{\alpha_1 \dots \beta_N})$ and $\mathrm{Im}(g_{\alpha_1 \dots \beta_N})$. Deriving a mathematical

description of $g_{\alpha_1 \dots \beta_N}$ is crucial and will be discussed later. The decision rules for which sets $m \in M$ have to be considered are specified through the set definition of M in Eq. (C.2b) and are a generalization of the rules specified in Eq. (23b) to the case of $2N$ atoms. These rules ensure that $(\alpha_1, \dots, \alpha_N, \beta_1, \dots, \beta_N) \in M \Rightarrow (-\alpha_1, \dots, -\alpha_N, -\beta_1, \dots, -\beta_N) \notin M$ by forcing the first non-vanishing coefficient to be positive. This measure prohibits counting coherences twice. Consequently, only matrix elements in the upper triangular of the density matrix are included in the sum. The decomposition into trigonometric basis functions and the set M read

$$\begin{aligned}\langle \hat{\mathrm{n}}_\uparrow(k_{\mathrm{A}_1}) \dots \hat{\mathrm{n}}_\uparrow(k_{\mathrm{A}_N}) \hat{\mathrm{n}}_\downarrow(k_{\mathrm{B}_1}) \dots \hat{\mathrm{n}}_\downarrow(k_{\mathrm{B}_N}) \rangle &= |\tilde{w}(k_{\mathrm{A}_1}, \dots, k_{\mathrm{B}_N})|^2 \\ \cdot \left[\sum_{m \in M} \mathrm{Re}(g_{\alpha_1 \dots \beta_N}) \cdot \cos\left(d \sum_{i=1}^{N} \alpha_i k_{\mathrm{A}_i} + \beta_i k_{\mathrm{B}_i} \right) - \mathrm{Im}(g_{\alpha_1 \dots \beta_N}) \cdot \sin\left(d \sum_{i=1}^{N} \alpha_i k_{\mathrm{A}_i} + \beta_i k_{\mathrm{B}_i} \right) \right], \end{aligned} \tag{C.2a}$$

$$\begin{aligned} M = \Big\{ \underbrace{(\alpha_1, \dots, \alpha_N, \beta_1, \dots, \beta_N)}_{=:(\gamma_1, \dots, \gamma_{2N})} \in \{0, \dots, L-1\} \times \{-(L-1), \dots, L-1\}^{2N-1} \;\Big|\; \\ \forall i \in \{2, \dots, 2N\} : \gamma_i \geq 0 \vee \exists j \in \{1, \dots, 2N-1\},\ j < i \text{ s.t. } \gamma_j > 0 \Big\}. \end{aligned} \tag{C.2b}$$

As stated above, the basis weights of the trigonometric functions are the real and imaginary parts of some coefficients $g_{\alpha_1 \dots \beta_N}$. Using the initial formulation of $\langle \hat{\mathrm{n}}_\uparrow(k_{\mathrm{A}_1}) \dots \hat{\mathrm{n}}_\downarrow(k_{\mathrm{B}_N}) \rangle$ in Eq. (C.1a), the coefficients can be expressed as the sum over the coherences connected to their specific set $(\alpha_1, \dots, \alpha_N, \beta_1, \dots, \beta_N) \in M$ as defined in Eq. (C.3a). For example, the set $(1, \dots, 1) \in M$ describes all coherences between any two states where all atom positions in the ket-state have moved one lattice site to the right with respect to the bra-state. For two atoms all terms included by any set $(\alpha, \beta) \in M$ are physical coherences, but this no longer holds for the $2N$-atom generalization. One can see this on the example of $(0, 1, 0, 1) \in M$ and the corresponding coherence $\langle 1112 | \rho | 1213 \rangle$. The ket $|1213\rangle$ describes a physical state, but the bra $\langle 1112|$ includes two fermions in the same state on lattice site one, which is forbidden by Pauli exclusion. These unphysical terms are zero by definition and we could ignore them safely, but for clearer notation we define a set $G_{\alpha_1 \dots \beta_N}$ of physical coherences in Eq. (C.3b) to exclude all unphysical coherences. The set rules of $G_{\alpha_1 \dots \beta_N}$ implement the proper lattice site gaps in the first two conditions and enforce all lattice site indices to to be different in each subsystem and

state in the last four rules,

$$g_{\alpha_1\dots\beta_N} = 2\sum_{g\in G_{\alpha_1\dots\beta_N}} \langle a_1,\dots,b_N|\,\rho\,|a'_1,\dots,b'_N\rangle \quad \text{with} \quad g \coloneqq (a_1,\dots,b_N,a'_1,\dots,b'_N)\,, \tag{C.3a}$$

$$\begin{aligned} G_{\alpha_1\dots\beta_N} = \Big\{ &(a_1,\dots,b_N,a'_1,\dots,b'_N) \in \{1,\dots,L\}^{4N} \;\Big|\; \forall i,j \in \{1,\dots,N\} \text{ with } i\neq j \\ &\text{s.t. } a'_i = a_i+\alpha_i \wedge b'_i = b_i+\beta_i \wedge a_i\neq a_j \wedge b_i \neq b_j \wedge a'_i \neq a'_j \wedge b'_i \neq b'_j \Big\}. \end{aligned} \tag{C.3b}$$

This basis is non-orthogonal like its two-particle analogue due to the Wannier envelope. Instead of measuring $g_{\alpha_1,\dots,\beta_N}$ one measures the smeared out coefficients $c_{\alpha_1,\dots,\beta_N}$. These have to be transformed via $\boldsymbol{Q}^{-1}$ to obtain the correct weights and remove contributions caused by small overlap between any two basis functions,

$$\vec{G} = \boldsymbol{Q}^{-1}\vec{C}. \tag{C.4}$$

Analogous to the two-atom case, matrix elements of $\boldsymbol{Q}$ are given by the respective basis function overlap integrals. We note at this point that one can take a different route here: By replacing single basis function with sums over all label permutations of basis elements, it is possible to return to a second quantization picture. We do not go into detail here, but especially for higher atom numbers, doing so can reduce numerical complexity and the size of $\boldsymbol{Q}$. For simplicity we continue in our first quantization picture in this appendix.

After obtaining the correct basis weights $g_{\alpha_1\dots\beta_N}$, we can now go on and construct a bound on the off-diagonal terms of the fidelity F_{coh}, making them experimentally accessible. The general approach remains identical: First one has to identify and sum over coefficients that carry contributing coherences, and subsequently subtract bounds of all coherences contained in those coefficients not actually appearing in the fidelity. Equation (C.5a) is the desired lower bound on the coherence part of the fidelity, based on the coherences $g_{\alpha_1\dots\beta_N}$ extractable from

the $2N$-particle momentum space correlation function,

$$\tilde{F}_{\mathrm{coh}}(\rho, \Psi_{\mathrm{MES}}) = \sum_{m\in\widetilde{M}} \left(\frac{\mathrm{Re}(g_{\alpha_1\ldots\beta_N})}{\binom{L}{N}\cdot(N!)^2} - 2\sum_{\substack{(a_1,\ldots,b_N,a'_1,\ldots,b'_N) \\ \in G_{\alpha_1\ldots\beta_N}\bigcap \widetilde{G}_{\alpha_1\ldots\beta_N}}} \frac{\sqrt{\langle a'_1,\ldots,b'_N|\,\rho\,|a'_1,\ldots,b'_N\rangle\,\langle a_1,\ldots,b_N|\,\rho\,|a_1,\ldots,b_N\rangle}}{\binom{L}{N}\cdot(N!)^2} \right), \tag{C.5a}$$

$$\widetilde{M} = \Big\{(\alpha_1,\ldots,\alpha_N,\beta_1,\ldots,\beta_N)\in M \;\Big|\; \sum\alpha_i = \sum\beta_i \wedge \widetilde{G}_{\alpha_1,\ldots,\beta_N}\neq\varnothing\Big\}, \tag{C.5b}$$

$$\widetilde{G}_{\alpha_1\ldots\beta_N} = \Big\{(a_1,\ldots,b_N,a'_1,\ldots,b'_N)\in G_{\alpha_1\ldots\beta_N} \;\Big|\; \forall a_i\,\exists! b_j \text{ s.t. } a_i=b_j \wedge \forall a'_i\,\exists! b'_j \text{ s.t. } a'_i=b'_j \wedge \left(\exists a_i\,\nexists a'_j \text{ s.t. } a_i=a'_j \vee \exists b_i\,\nexists b'_j \text{ s.t. } b_i=b'_j\right),\ i,j\in\{1,\ldots,N\}\Big\}. \tag{C.5c}$$

The first sum of the bound in Eq. (C.5a) runs over elements of the subset $\widetilde{M}\subset M$, which contains the elements of M with contributing coherences. We define $\widetilde{M}$ implicitly in Eq. (C.5b), where two conditions on elements of $\widetilde{M}$ are given as follows. Firstly, the sum over all α coefficients of subset A must be equal to that of the β coefficients of subset B. This can be understood by again looking at the two-atom case: There, double occupation states are connected via $\alpha=\beta=:\delta$ for all indices such that only coherences with dimer populations in A and B like $\langle mm|\,\rho\,|nn\rangle$ appear. With the introduction of label permutations in first quantization, one-to-one matching of α to β coefficients is no longer an option, as different coherence realization can have different label permutations. One example for a $2+2$ system with $L=4$ is the coherence $\langle 2332|\,\rho\,|4343\rangle$ with $(2,0,1,1)\in\widetilde{M}$, equivalent to $\langle 2323|\,\rho\,|3434\rangle$ in second quantization and corresponding to $(1,1,1,1)\in\widetilde{M}$. The sums over the difference of label indices for each subsystem however must still be equal,

$$\sum_{i=1}^{N}\alpha_i = \sum_{i=1}^{N}(a'_i-a_i) = \sum_{i=1}^{N}(b'_i-b_i) = \sum_{i=1}^{N}\beta_i, \tag{C.6}$$

as the labels can be rearranged in the sum to have the same order in both subsystems. Restricting M in this way is not yet sufficient, as there are sets which fulfill this requirement, but still do not hold relevant coherence. To see this consider e.g. a lattice of three sites and the set $(1,2,1,2)\in M$. All four possible coherences mapping between existing sites, $\langle 1111|\,\rho\,|2323\rangle$, $\langle 1121|\,\rho\,|2333\rangle$, $\langle 2111|\,\rho\,|3323\rangle$, and $\langle 2121|\,\rho\,|3333\rangle$, contain at least one unphysical bra or ket. We therefore define the subset $\widetilde{G}_{\alpha_1\ldots\beta_N}\subset G_{\alpha_1\ldots\beta_N}$ of all relevant physical coherences needed for $\tilde{F}_{\mathrm{coh}}$ [see Eq. (20)] in Eq. (C.5c) and require any set of coefficients $(\alpha_1,\ldots,\beta_N)\in\widetilde{M}$ to

have a non-empty set $\widetilde{G}_{\alpha_1\ldots\beta_N} \neq \varnothing$ attached to it. By doing so, one can circumvent summing over basis coefficients that do not actually hold necessary coherences. If the whole term is not removed manually, one would simply subtract a coherence bound for every possible coherence contained in that specific coefficient $g_{\alpha_1\ldots\beta_N}$ in Eq. (C.5a). Keeping terms that could hold physical coherences, but in fact do not, would therefore have an avoidable negative impact on the fidelity bound.

The set $\widetilde{G}_{\alpha_1\ldots\beta_N}$ chooses potentially contributing coherences with the first two conditions of Eq. (C.5c) by matching atom positions one-to-one disregarding specific label positions in both subsystems for bra and ket state. Besides the states prohibited by Pauli rule already taken care of in the definition of $G_{\alpha_1\ldots\beta_N}$ in Eq. (C.3b), one must now also consider coherences of the form $\langle abcd|\,\rho\,|bacd\rangle$ where the only change is label permutation in one subsystem. The two states therefore look identical in second quantization and thus qualify as a state population. It is necessary to exclude these terms as state populations are explicitly taken out of the coherence part $\tilde{F}_{\text{coh}}$ [Eq. (20)]. Conditions three and four in Eq. (C.5c) are designed to make sure these states are excluded by demanding physical change of at least one atom position between initial and final state.

With the sets $\widetilde{M}$ and $\widetilde{G}_{\alpha_1\ldots\beta_N}$ in place, the next step is to construct the bounds for coherences that are not contributing to the fidelity and thus are not in $\widetilde{G}_{\alpha_1\ldots\beta_N}$. The second sum in Eq. (C.5a) hence runs over all non-relevant coherences $\langle a_1,\ldots,b_N|\,\rho\,|a'_1,\ldots,b'_N\rangle$ with $(a_1,\ldots,b_N,a'_1,\ldots,b'_N) \in G_{\alpha_1\ldots\beta_N} \bigcap \overline{\widetilde{G}_{\alpha_1\ldots\beta_N}}$ where we subtract the same bound constructed earlier through Cauchy-Schwarz inequality [Eq. (28)]. Finally normalization has to be adapted: Firstly, the local Hilbert space size increases from L to $\binom{L}{N}$, requiring adaption of the general normalization factor. Secondly, each relevant coherence is replaced by $(N!)^4$ equivalents in first quantization. They are indivudally weighted with a normalization factor of $(N!)^{-2}$, yielding a total increase of $(N!)^2$, as we sum over all of them. By dividing by this additional factor we reach the final normalized result stated in Eq. (C.5a).

D. Tripartite Entanglement Dimension Bounds

Here we extent the concept of entanglement dimension bounds to tripartite reference states with generalized Schmidt decomposition in close analogy to the original proof for bipartite states given in [49]. The proofs are analogous in most parts, but we include them for completeness.

We start with an expression of maximum state overlap of our D-dimensional reference state according to the definition of multipartite entanglement dimensions given in [87] and some d-dimensional probe state $|\phi_d\rangle$ given in the same tensor basis $|klm\rangle$,

$$F_d = \max_{|\phi_d\rangle} \left| \left(\langle klm| \sum_{k,l,m=1}^{D} c^*_{klm} \right) \left(\sum_{i=1}^{D} \lambda_i |iii\rangle \right) \right|^2 = \max_{|\phi_d\rangle} \left| \sum_{i=1}^{D} \sum_{k,l,m=1}^{D} \langle k|i\rangle \langle l|i\rangle \langle m|i\rangle c^*_{klm} \lambda_i \right|^2 . \quad \text{(D.1)}$$

We use that $\langle i|j\rangle = \langle j|i\rangle = \delta_{ij}$ and rewrite Eq. (D.1) by adding a trace and sorting basis elements, such that

$$F_d = \max_{|\phi_d\rangle} \left| \mathrm{Tr} \left(B^\dagger \sum_{i=1}^{D} \lambda_i |i\rangle \langle i| \langle i| \right) \right|^2 \quad \text{(D.2)}$$

with the operator $B = c_{klm} |k\rangle \langle m| \langle l|$. Next one adds the rank d-projector P_d and by the cyclic property of the trace obtains

$$F_d = \max_{|\phi_d\rangle} \left| \mathrm{Tr} \left(P_d B^\dagger \sum_{i=1}^{D} \lambda_i |i\rangle \langle i| \langle i| \right) \right|^2 = \max_{|\phi_d\rangle} \left| \mathrm{Tr} \left(B^\dagger \sum_{i=1}^{D} \lambda_i |i\rangle \langle i| \langle i| P_d \right) \right|^2 \quad \text{(D.3)}$$

By applying the Cauchy-Schwarz inequality for this picture, $|\mathrm{Tr}(AB^\dagger)|^2 \leq \mathrm{Tr}(AA^\dagger)\,\mathrm{Tr}(BB^\dagger)$, we can separate contributions from probe and reference states as follows,

$$F_d \leq \max_{|\phi_d\rangle} \mathrm{Tr}\left(B^\dagger B\right) \mathrm{Tr}\left(P_d \sum_{i=1}^{D} \lambda_i^2 |i\rangle \underbrace{\langle i| \langle i|i\rangle |i\rangle}_{=\mathbb{1}} \langle i| P_d \right). \quad \text{(D.4)}$$

We expand the first term like

$$\mathrm{Tr}\left(B^\dagger B\right) = \mathrm{Tr}\left(c^*_{klm}c_{klm}\underbrace{|l\rangle\langle m|k\rangle|k\rangle\langle m|\langle l|}_{=\mathbb{1}}\right) = \sum_{k,l,m=1}^{D} c^*_{klm}c_{klm} = 1 \tag{D.5}$$

and by inserting $P_d = \sum_{j=1}^{d} |j\rangle\langle j|$ where we select the basis elements with the highest values of λ_j we obtain the same result as for the bipartite case with

$$F_d \leq \sum_{i=1}^{d} \lambda_i^2, \quad \forall i,j \text{ with } i \leq j \text{ s.t. } \lambda_i \geq \lambda_j. \tag{D.6}$$

Since we find equality for

$$\left|\left(\frac{1}{N}\sum_{j=1}^{d}\langle jjj|\,\lambda_j\right)\left(\sum_{i=1}^{D}\lambda_i\,|iii\rangle\right)\right|^2 = \sum_{i=1}^{d}\lambda_i^2 \qquad \text{with } N = \sqrt{\sum_{j=1}^{d}\lambda_j^2} \tag{D.7}$$

this bound is in fact tight. We proved the existence of the bounds for a pure state $|\phi_d\rangle$, however due to the convexity of the fidelity, mixed states would just lower the bound further. This fact makes the bound applicable to generally mixed states ρ [49].

E. Details on Multipartite Entanglement Certification

Extending the original scheme for entanglement certification for multipartite entanglement is straightforward, but tedious. Here we briefly want to give a starting point of how such an expansion can be done and present the final bound $\tilde{F}_{\mathrm{coh}}$. Like before, we decompose the momentum correlation function of three atoms $\langle \hat{\mathrm{n}}_1(k_1)\hat{\mathrm{n}}_2(k_2)\hat{\mathrm{n}}_3(k_3)\rangle$ in terms of coherences and consider phases picked up due to the Fourier transformation. The tripartite description then reads

$$\langle \hat{\mathrm{n}}_1(k_1)\hat{\mathrm{n}}_2(k_2)\hat{\mathrm{n}}_3(k_3)\rangle = \sum_{\substack{a,b,c=1\\a',b',c'=1}}^{L} \phi_{a\ldots c'}(k_1,k_2,k_3)\cdot\langle abc|\,\rho\,|a'b'c'\rangle\,, \tag{E.1a}$$

$$\phi_{a\ldots c'}(k_1,k_2,k_3) = |\tilde{w}(k_1,k_2,k_3)|^2\cdot\exp\big\{-id\cdot[(a-a')k_1+(b-b')k_2+(c-c')k_3]\big\}. \tag{E.1b}$$

We label the three distinguishable atom species $\{1,2,3\}$ with their respective lattice site indices $\{a,b,c\}$ and $\{a',b',c'\}$ for the bra and ket states. This description can be expressed analogous to Eqs. (23) in trigonometric basis functions of all three lattice momenta k_1, k_2, and k_3. Special care has to be taken to avoid double counting by adapting the set M of of admissible lattice gap sets to again enforce $(\alpha,\beta,\gamma)\in M \Rightarrow (-\alpha,-\beta,-\gamma)\notin M$. This is necessary to do to get the full reconstruction of the momentum correlation function, since the actual coefficients $g_{\alpha\beta\gamma}$ have to be obtained from the full distribution of measured coefficients $c_{\alpha\beta\gamma}$ first. The redefined set M for three atomic species is given in Eq. (E.2b). All remaining steps outlined in Eqs. (24) to (28) can be adapted analogously such that one arrives at the final result for the bound of the coherence contributions as follows,

$$\tilde{F}_{\mathrm{coh}}(\rho,\Psi_{\mathrm{MES}}) = \sum_{\delta=1}^{L-1}\left(\frac{\mathrm{Re}(g_{\delta\delta\delta})}{L} - 2\sum_{\substack{a,b,c=1\\a\neq b\vee b\neq c}}^{L-\delta}\frac{\sqrt{\langle a'b'c'|\,\rho\,|a'b'c'\rangle\,\langle abc|\,\rho\,|abc\rangle}}{L}\right) \tag{E.2a}$$

$$\text{with}\quad a' \coloneqq a+\delta \quad b' \coloneqq b+\delta \quad c' \coloneqq c+\delta,$$

$$M = \Big\{(\alpha,\beta,\gamma)\in\{-(L-1),\ldots,L-1\}^3 \;\Big|\; \alpha\geq 0\wedge(\beta\geq 0\vee\alpha>0)\wedge(\gamma>0\vee\beta\neq 0\vee\alpha>0)\Big\}, \tag{E.2b}$$

$$g_{\alpha\beta\gamma} = 2\sum_{a=1}^{L-\alpha}\sum_{b=\max(1,1-\beta)}^{\min(L,L-\beta)}\sum_{c=\max(1,1-\gamma)}^{\min(L,L-\gamma)}\langle abc|\,\rho\,|(a+\alpha)(b+\beta)(c+\gamma)\rangle\,. \tag{E.2c}$$

References

[1] A. Einstein, B. Podolsky, and N. Rosen. "Can Quantum-Mechanical Description of Physical Reality Be Considered Complete?" In: *Physical Review* 47.10 (May 1935), pp. 777–780. ISSN: 0031-899X. DOI: 10.1103/PhysRev.47.777.

[2] J. S. Bell. "On the Einstein Podolsky Rosen paradox". In: *Physics Physique Fizika* 1.3 (Nov. 1964), pp. 195–200. ISSN: 0554-128X. DOI: 10.1103/PhysicsPhysiqueFizika.1.195.

[3] W. Dür et al. "Entanglement in Spin Chains and Lattices with Long-Range Ising-Type Interactions". In: *Physical Review Letters* 94.9 (Mar. 2005). ISSN: 00319007. DOI: 10.1103/PhysRevLett.94.097203.

[4] A. M. Kaufman et al. "Quantum thermalization through entanglement in an isolated many-body system". In: *Science* 353.6301 (Aug. 2016), pp. 794–800. ISSN: 0036-8075. DOI: 10.1126/science.aaf6725.

[5] R. Horodecki et al. "Quantum entanglement". In: *Rev. Mod. Phys.* 81 (2 June 2009), pp. 865–942. DOI: 10.1103/RevModPhys.81.865.

[6] A. Almheiri et al. "Black holes: complementarity or firewalls?" In: *Journal of High Energy Physics* 2013.2 (Feb. 2013). ISSN: 10298479. DOI: 10.1007/JHEP02(2013)062.

[7] M. A. Nielsen, I. Chuang, and L. K. Grover. *Quantum Computation and Quantum Information*. 10th edition. New York, USA: Cambridge University Press, 2010. ISBN: 9781107002173.

[8] A. K. Ekert. "Quantum cryptography based on Bell's theorem". In: *Phys. Rev. Lett.* 67 (6 Aug. 1991), pp. 661–663. DOI: 10.1103/PhysRevLett.67.661.

[9] D. S. Naik et al. "Entangled State Quantum Cryptography: Eavesdropping on the Ekert Protocol". In: *Physical Review Letters* 84.20 (May 2000), pp. 4733–4736. ISSN: 10797114. DOI: 10.1103/PhysRevLett.84.4733.

[10] W. Tittel et al. "Quantum Cryptography Using Entangled Photons in Energy-Time Bell States". In: *Physical Review Letters* 84.20 (May 2000), pp. 4737–4740. ISSN: 10797114. DOI: 10.1103/PhysRevLett.84.4737.

[11] C. H. Bennett et al. "Teleporting an unknown quantum state via dual classical and Einstein-Podolsky-Rosen channels". In: *Physical Review Letters* 70.13 (1993), pp. 1895–1899. ISSN: 00319007. DOI: 10.1103/PhysRevLett.70.1895.

[12] D. Bouwmeester et al. "Experimental quantum teleportation". In: *Nature* 390.6660 (Dec. 1997), pp. 575–579. ISSN: 0028-0836. DOI: 10.1038/37539.

[13] D. Boschi et al. "Experimental Realization of Teleporting an Unknown Pure Quantum State via Dual Classical and Einstein-Podolsky-Rosen Channels". In: *Physical Review Letters* 80.6 (Feb. 1998), pp. 1121–1125. ISSN: 10797114. DOI: 10.1103/PhysRevLett.80.1121.

[14] C. H. Bennett and S. J. Wiesner. "Communication via one- and two-particle operators on Einstein-Podolsky-Rosen states". In: *Physical Review Letters* 69.20 (Nov. 1992), pp. 2881–2884. ISSN: 00319007. DOI: 10.1103/PhysRevLett.69.2881.

[15] K. Mattle et al. "Dense Coding in Experimental Quantum Communication". In: *Physical Review Letters* 76.25 (June 1996), pp. 4656–4659. ISSN: 10797114. DOI: 10.1103/PhysRevLett.76.4656.

[16] A. Kitaev and J. Preskill. "Topological Entanglement Entropy". In: *Physical Review Letters* 96.11 (Mar. 2006). ISSN: 00319007. DOI: 10.1103/PhysRevLett.96.110404.

[17] M. Haque, O. Zozulya, and K. Schoutens. "Entanglement Entropy in Fermionic Laughlin States". In: *Physical Review Letters* 98.6 (Feb. 2007), p. 4. ISSN: 00319007. DOI: 10.1103/PhysRevLett.98.060401.

[18] A. Osterloh et al. "Scaling of entanglement close to a quantum phase transition". In: *Nature* 416.6881 (Apr. 2002), pp. 608–610. ISSN: 00280836. DOI: 10.1038/416608a.

[19] T. J. Osborne and M. A. Nielsen. "Entanglement in a simple quantum phase transition". In: *Physical Review A - Atomic, Molecular, and Optical Physics* 66.3 (Sept. 2002). ISSN: 10941622. DOI: 10.1103/PhysRevA.66.032110.

[20] G. Vidal et al. "Entanglement in Quantum Critical Phenomena". In: *Physical Review Letters* 90.22 (June 2003). ISSN: 10797114. DOI: 10.1103/PhysRevLett.90.227902.

[21] N. Laflorencie. "Quantum entanglement in condensed matter systems". In: *Physics Reports* 646 (Aug. 2016). ISSN: 03701573. DOI: 10.1016/j.physrep.2016.06.008.

[22] R. Orús. "A practical introduction to tensor networks: Matrix product states and projected entangled pair states". In: *Annals of Physics* 349 (Oct. 2014), pp. 117–158. ISSN: 00034916. DOI: 10.1016/j.aop.2014.06.013.

[23] D. Jaksch et al. "Fast Quantum Gates for Neutral Atoms". In: *Physical Review Letters* 85.10 (Sept. 2000), pp. 2208–2211. ISSN: 00319007. DOI: 10.1103/PhysRevLett.85.2208.

[24] T. Esslinger. "Fermi-Hubbard Physics with Atoms in an Optical Lattice". In: *Annual Review of Condensed Matter Physics* 1 (Nov. 2010), pp. 129–152. ISSN: 19475454. DOI: 10.1146/annurev-conmatphys-070909-104059.

[25] I. Bloch, J. Dalibard, and S. Nascimbène. "Quantum simulations with ultracold quantum gases". In: *Nature Physics* 8.4 (Apr. 2012), pp. 267–276. ISSN: 17452473. DOI: 10.1038/nphys2259.

[26] C. Gross and I. Bloch. "Quantum simulations with ultracold atoms in optical lattices". In: *Science* 357.6355 (Sept. 2017), pp. 995–1001. ISSN: 10959203. DOI: 10.1126/science.aal3837.

[27] L. Tarruell and L. Sanchez-Palencia. "Quantum simulation of the Hubbard model with ultracold fermions in optical lattices". In: *Comptes Rendus Physique* 19.6 (Nov. 2018), pp. 365–393. ISSN: 16310705. DOI: 10.1016/j.crhy.2018.10.013.

[28] W. Hofstetter and T. Qin. "Quantum simulation of strongly correlated condensed matter systems". In: *Journal of Physics B: Atomic, Molecular and Optical Physics* 51.8 (Apr. 2018). ISSN: 0953-4075. DOI: 10.1088/1361-6455/aaa31b.

[29] E. Altman et al. "Quantum Simulators: Architectures and Opportunities". In: *PRX Quantum* 2.1 (Feb. 2021). ISSN: 2691-3399. DOI: 10.1103/prxquantum.2.017003.

[30] D. Jaksch et al. "Cold Bosonic Atoms in Optical Lattices". In: *Physical Review Letters* 81.15 (Oct. 1998), pp. 3108–3111. ISSN: 10797114. DOI: 10.1103/PhysRevLett.81.3108.

[31] W. S. Bakr et al. "A quantum gas microscope for detecting single atoms in a Hubbard-regime optical lattice". In: *Nature* 462.7269 (Nov. 2009), pp. 74–77. ISSN: 00280836. DOI: 10.1038/nature08482.

[32] S. Murmann et al. "Two Fermions in a Double Well: Exploring a Fundamental Building Block of the Hubbard Model". In: *Physical Review Letters* 114.8 (Feb. 2015). ISSN: 10797114. DOI: 10.1103/PhysRevLett.114.080402.

[33] F. Schäfer et al. "Tools for quantum simulation with ultracold atoms in optical lattices". In: *Nature Reviews Physics* 2.8 (July 2020), pp. 411–425. ISSN: 25225820. DOI: 10.1038/s42254-020-0195-3.

[34] L. Gurvits. "Classical complexity and quantum entanglement". In: *Journal of Computer and System Sciences* 69.3 SPEC. ISS. (Nov. 2004), pp. 448–484. ISSN: 00220000. DOI: 10.1016/j.jcss.2004.06.003.

[35] N. Friis et al. "Entanglement certification from theory to experiment". In: *Nature Reviews Physics* 1.1 (Dec. 2018), pp. 72–87. ISSN: 25225820. DOI: 10.1038/s42254-018-0003-5.

[36] H. Li and F. D. Haldane. "Entanglement Spectrum as a Generalization of Entanglement Entropy: Identification of Topological Order in Non-Abelian Fractional Quantum Hall Effect States". In: *Physical Review Letters* 101.1 (July 2008). ISSN: 00319007. DOI: 10.1103/PhysRevLett.101.010504.

[37] L. Fidkowski. "Entanglement Spectrum of Topological Insulators and Superconductors". In: *Physical Review Letters* 104.13 (Apr. 2010). ISSN: 00319007. DOI: 10.1103/PhysRevLett.104.130502.

[38] P. Calabrese and A. Lefevre. "Entanglement spectrum in one-dimensional systems". In: *Physical Review A - Atomic, Molecular, and Optical Physics* 78.3 (Sept. 2008). ISSN: 10502947. DOI: 10.1103/PhysRevA.78.032329.

[39] C. Chamon, A. Hamma, and E. R. Mucciolo. "Emergent Irreversibility and Entanglement Spectrum Statistics". In: *Physical Review Letters* 112.24 (June 2014). ISSN: 0031-9007. DOI: 10.1103/PhysRevLett.112.240501.

[40] D. Shaffer et al. "Irreversibility and entanglement spectrum statistics in quantum circuits". In: *Journal of Statistical Mechanics: Theory and Experiment* 2014.12 (Dec. 2014). ISSN: 1742-5468. DOI: 10.1088/1742-5468/2014/12/P12007.

[41] M. Serbyn and J. E. Moore. "Spectral statistics across the many-body localization transition". In: *Physical Review B* 93.4 (Jan. 2016). ISSN: 2469-9950. DOI: 10.1103/PhysRevB.93.041424.

[42] S. D. Geraedts, R. Nandkishore, and N. Regnault. "Many-body localization and thermalization: Insights from the entanglement spectrum". In: *Physical Review B* 93.17 (May 2016). ISSN: 24699969. DOI: 10.1103/PhysRevB.93.174202.

[43] A. Muthukrishnan and C. R. Stroud. "Multivalued logic gates for quantum computation". In: *Physical Review A* 62.5 (Oct. 2000). ISSN: 1050-2947. DOI: 10.1103/PhysRevA.62.052309.

[44] B. P. Lanyon et al. "Simplifying quantum logic using higher-dimensional Hilbert spaces". In: *Nature Physics* 5.2 (Dec. 2009), pp. 134–140. ISSN: 17452481. DOI: 10.1038/nphys1150.

[45] M. Neeley et al. "Emulation of a Quantum Spin with a Superconducting Phase Qudit". In: *Science* 325.5941 (Aug. 2009), pp. 722–725. ISSN: 00368075. DOI: 10.1126/science.1173440.

[46] C. Kokail et al. *Quantum Variational Learning of the Entanglement Hamiltonian*. May 2021. arXiv: 2105.04317.

[47] C. Kokail et al. "Entanglement Hamiltonian tomography in quantum simulation". In: *Nature Physics* 17.8 (June 2021), pp. 936–942. ISSN: 1745-2473. DOI: 10.1038/s41567-021-01260-w.

[48] J. Bavaresco et al. "Measurements in two bases are sufficient for certifying high-dimensional entanglement". In: *Nature Physics* 14 (Oct. 2018), pp. 1032–1037. ISSN: 1745-2473. DOI: 10.1038/s41567-018-0203-z.

[49] R. Fickler et al. "Interface between path and orbital angular momentum entanglement for high-dimensional photonic quantum information". In: *Nature Communications* 5 (July 2014). ISSN: 20411723. DOI: 10.1038/ncomms5502.

[50] S. Fölling et al. "Spatial quantum noise interferometry in expanding ultracold atom clouds". In: *Nature* 434.7032 (Mar. 2005), pp. 481–484. ISSN: 00280836. DOI: 10.1038/nature03500.

[51] A. Bergschneider et al. "Experimental characterization of two-particle entanglement through position and momentum correlations". In: *Nature Physics* 15.7 (Apr. 2019), pp. 640–644. ISSN: 17452481. DOI: 10.1038/s41567-019-0508-6.

[52] E. Schrödinger. "Die gegenwärtige Situation in der Quantenmechanik". In: *Die Naturwissenschaften* 23.48 (Nov. 1935), pp. 807–812. ISSN: 0028-1042. DOI: 10.1007/BF01491891.

[53] S. K. Lamoreaux. "A Review of the Experimental Tests of Quantum Mechanics". In: *International Journal of Modern Physics A* 07.27 (Oct. 1992), pp. 6691–6762. ISSN: 0217-751X. DOI: 10.1142/S0217751X92003082.

[54] E. Schrödinger. "Die gegenwärtige Situation in der Quantenmechanik". In: *Die Naturwissenschaften* 23.50 (Dec. 1935), pp. 844–849. ISSN: 00281042. DOI: 10.1007/BF01491987.

[55] E. Schmidt. "Zur Theorie der linearen und nichtlinearen lntegralgleichungen." In: *Mathematische Annalen* 63 (1907), pp. 433–476. ISSN: 0303402X. DOI: 10.1007/BF01449770.

[56] J. A. Miszczak. "Singular ValueDdecomposition and Matrix Reorderings in Quantum Information Theory". In: *International Journal of Modern Physics C* 22.09 (Sept. 2011), pp. 897–918. ISSN: 0129-1831. DOI: 10.1142/S0129183111016683.

[57] A. Acín et al. "Generalized Schmidt Decomposition and Classification of Three-Quantum-Bit States". In: *Physical Review Letters* 85.7 (Aug. 2000), pp. 1560–1563. ISSN: 00319007. DOI: 10.1103/PhysRevLett.85.1560.

[58] B. M. Terhal and P. Horodecki. "Schmidt number for density matrices". In: *Physical Review A - Atomic, Molecular, and Optical Physics* 61 (Mar. 2000). ISSN: 10941622. DOI: 10.1103/PhysRevA.61.040301.

[59] N. W. Ashcroft and D. Mermin. *Solid State Physics*. Brooks/Cole Publishing Company, 1976. ISBN: 8131500527.

[60] R. P. Feynman. "Simulating physics with computers". In: *International Journal of Theoretical Physics* 21.6-7 (June 1982), pp. 467–488. ISSN: 00207748. DOI: 10.1007/BF02650179.

[61] M. Lewenstein et al. "Ultracold atomic gases in optical lattices: mimicking condensed matter physics and beyond". In: *Advances in Physics* 56.2 (Mar. 2007), pp. 243–379. ISSN: 0001-8732. DOI: 10.1080/00018730701223200.

[62] N. I. Strohmaier. "Exploring the Hubbard Model With Ultracold Fermionic Atoms in an Optical Lattice". PhD thesis. ETH Zürich, 2010.

[63] G. H. Wannier. "The Structure of Electronic Excitation Levels in Insulating Crystals". In: *Physical Review* 52.3 (Aug. 1937), pp. 191–197. ISSN: 0031-899X. DOI: 10.1103/PhysRev.52.191.

[64] M. L. Wall. *Quantum Many-Body Physics of Ultracold Molecules in Optical Lattices: Models and Simulation Methods*. Springer Theses. Springer International Publishing, 2015. ISBN: 9783319142524.

[65] W. Kohn. "Analytic Properties of Bloch Waves and Wannier Functions". In: *Physical Review* 115.4 (Aug. 1959), pp. 809–821. ISSN: 0031-899X. DOI: 10.1103/PhysRev.115.809.

[66] J. Hubbard. "Electron correlations in narrow energy bands". In: *Proceedings of the Royal Society of London. Series A. Mathematical and Physical Sciences* 276.1365 (Nov. 1963), pp. 238–257. ISSN: 0080-4630. DOI: 10.1098/rspa.1963.0204.

[67] H. Feshbach. "Unified theory of nuclear reactions". In: *Annals of Physics* 5.4 (Dec. 1958), pp. 357–390. ISSN: 1096035X. DOI: 10.1016/0003-4916(58)90007-1.

[68] M. Piani and C. E. Mora. "Class of positive-partial-transpose bound entangled states associated with almost any set of pure entangled states". In: *Physical Review A - Atomic, Molecular, and Optical Physics* 75.1 (Jan. 2007). ISSN: 10502947. DOI: 10.1103/PhysRevA.75.012305.

[69] M. Huber and J. I. De Vicente. "Structure of Multidimensional Entanglement in Multipartite Systems". In: *Physical Review Letters* 110.3 (Jan. 2013). ISSN: 00319007. DOI: 10.1103/PhysRevLett.110.030501.

[70] M. Bonneau et al. "Characterizing twin-particle entanglement in double-well potentials". In: *Physical Review A* 98.3 (Sept. 2018). ISSN: 24699934. DOI: 10.1103/PhysRevA.98.033608.

[71] K. Atkinson. *An Introduction to Numerical Analysis*. 2nd edition. Iowa City: Wiley, 1989. ISBN: 0471624896.

[72] R. E. Caflisch. "Monte Carlo and quasi-Monte Carlo methods". In: *Acta Numerica* 7 (Jan. 1998). ISSN: 14740508. DOI: 10.1017/S0962492900002804.

[73] C. M. Bishop. *Pattern Recognition and Machine Learning*. 1th edition. New York: Springer US, 2006. ISBN: 978-0-387-31073-2.

[74] S. Ross. "Generating Continuous Random Variables". In: *Simulation*. 5th edition. Academic Press, 2013. Chap. 5, pp. 69–96. ISBN: 9780124158252. DOI: 10.1016/b978-0-12-415825-2.00005-x.

[75] S. Ross. "Random Numbers". In: *Simulation*. 5th edition. Academic Press, 2013. Chap. 3, pp. 39–46. ISBN: 9780124158252. DOI: 10.1016/B978-0-12-415825-2.00003-6.

[76] P. W. Anderson. "Absence of Diffusion in Certain Random Lattices". In: *Physical Review* 109.5 (Mar. 1958), pp. 1492–1505. ISSN: 0031899X. DOI: 10.1103/PhysRev.109.1492.

[77] E. Abrahams et al. "Scaling Theory of Localization: Absence of Quantum Diffusion in Two Dimensions". In: *Physical Review Letters* 42.10 (Mar. 1979), pp. 673–676. ISSN: 0031-9007. DOI: 10.1103/PhysRevLett.42.673.

[78] A. N. Wenz et al. "From Few to Many: Observing the Formation of a Fermi Sea One Atom at a Time". In: *Science* 342.6157 (Oct. 2013), pp. 457–460. ISSN: 0036-8075. DOI: 10.1126/science.1240516.

[79] L. Rammelmüller et al. "Evolution from few- to many-body physics in one-dimensional Fermi systems: One- and two-body density matrices and particle-partition entanglement". In: *Physical Review A* 96.3 (Sept. 2017). ISSN: 24699934. DOI: 10.1103/PhysRevA.96.033635.

[80] J. H. Becher et al. "Measurement of Identical Particle Entanglement and the Influence of Antisymmetrization". In: *Physical Review Letters* 125.18 (Oct. 2020). ISSN: 10797114. DOI: 10.1103/PhysRevLett.125.180402.

[81] Ralf Arne Klemt. "Correlations from Microscopic to Macroscopic Quantum Systems: Interactions vs Indistinguishability". PhD thesis. Heidelberg University, 2021.

[82] D. M. Greenberger, M. A. Horne, and A. Zeilinger. "Going Beyond Bell's Theorem". In: *Bell's Theorem, Quantum Theory and Conceptions of the Universe*. Ed. by M. Kafatos. Dordrecht: Springer Netherlands, 1989, pp. 69–72. ISBN: 978-94-017-0849-4. DOI: 10.1007/978-94-017-0849-4_10.

[83] W. Dür, G. Vidal, and J. I. Cirac. "Three qubits can be entangled in two inequivalent ways". In: *Phys. Rev. A* 62 (6 Nov. 2000). DOI: 10.1103/PhysRevA.62.062314.

[84] H. A. Carteret, A. Higuchi, and A. Sudbery. "Multipartite generalization of the Schmidt decomposition". In: *Journal of Mathematical Physics* 41.12 (Nov. 2000), pp. 7932–7939. ISSN: 00222488. DOI: 10.1063/1.1319516.

[85] M. Huber, M. Perarnau-Llobet, and J. I. De Vicente. "Entropy vector formalism and the structure of multidimensional entanglement in multipartite systems". In: *Physical Review A - Atomic, Molecular, and Optical Physics* 88.4 (Oct. 2013). ISSN: 10502947. DOI: 10.1103/PhysRevA.88.042328.

[86] A. V. Thapliyal. "Multipartite pure-state entanglement". In: *Physical Review A - Atomic, Molecular, and Optical Physics* 59.5 (May 1999), pp. 3336–3342. ISSN: 10941622. DOI: 10.1103/PhysRevA.59.3336.

[87] L. Chen, Y. Yang, and W. S. Tang. "Schmidt number of bipartite and multipartite states under local projections". In: *Quantum Information Processing* 16.3 (Feb. 2017). ISSN: 15700755. DOI: 10.1007/s11128-016-1501-y.

[88] T. B. Ottenstein et al. "Collisional Stability of a Three-Component Degenerate Fermi Gas". In: *Physical Review Letters* 101.20 (Nov. 2008). ISSN: 00319007. DOI: 10.1103/PhysRevLett.101.203202.

[89] J. H. Huckans et al. "Three-Body Recombination in a Three-State Fermi Gas with Widely Tunable Interactions". In: *Physical Review Letters* 102.16 (Apr. 2009). ISSN: 00319007. DOI: 10.1103/PhysRevLett.102.165302.

[90] P. Azaria, S. Capponi, and P. Lecheminant. "Three-component Fermi gas in a one-dimensional optical lattice". In: *Physical Review A - Atomic, Molecular, and Optical Physics* 80.4 (Oct. 2009). ISSN: 10502947. DOI: 10.1103/PhysRevA.80.041604.

[91] G. Zürn et al. "Precise Characterization of ^{6}Li Feshbach Resonances Using Trap-Sideband-Resolved RF Spectroscopy of Weakly Bound Molecules". In: *Physical Review Letters* 110.13 (Mar. 2013). ISSN: 00319007. DOI: 10.1103/PhysRevLett.110.135301.

[92] K. Dieckmann et al. "Decay of an Ultracold Fermionic Lithium Gas near a Feshbach Resonance". In: *Physical Review Letters* 89.20 (Oct. 2002). ISSN: 10797114. DOI: 10.1103/PhysRevLett.89.203201.

[93] C. H. Schunck et al. "Feshbach resonances in fermionic ^{6}Li". In: *Physical Review A - Atomic, Molecular, and Optical Physics* 71.4 (Apr. 2005). ISSN: 10502947. DOI: 10.1103/PhysRevA.71.045601.

[94] H. Häffner et al. "Scalable multiparticle entanglement of trapped ions". In: *Nature* 438.7068 (Dec. 2005), pp. 643–646. ISSN: 14764687. DOI: 10.1038/nature04279.

[95] D. Gross et al. "Quantum State Tomography via Compressed Sensing". In: *Physical Review Letters* 105.15 (Oct. 2010). ISSN: 00319007. DOI: 10.1103/PhysRevLett.105.150401.

[96] A. Kalev, R. L. Kosut, and I. H. Deutsch. "Quantum tomography protocols with positivity are compressed sensing protocols". In: *npj Quantum Information* 1.August (Dec. 2015). ISSN: 20566387. DOI: 10.1038/npjqi.2015.18.

[97] C. A. Riofrío et al. "Experimental quantum compressed sensing for a seven-qubit system". In: *Nature Communications* 8 (May 2017). ISSN: 20411723. DOI: 10.1038/ncomms15305.

[98] J. Shang, Z. Zhang, and H. K. Ng. "Superfast maximum-likelihood reconstruction for quantum tomography". In: *Physical Review A* 95.6 (June 2017). ISSN: 24699934. DOI: 10.1103/PhysRevA.95.062336.

[99] C. Granade, J. Combes, and D. G. Cory. "Practical Bayesian tomography". In: *New Journal of Physics* 18.3 (Mar. 2016). ISSN: 13672630. DOI: 10.1088/1367-2630/18/3/033024.

[100] M. Cramer et al. "Efficient quantum state tomography". In: *Nature Communications* 1.149 (Dec. 2010). ISSN: 20411723. DOI: 10.1038/ncomms1147.

[101] T. Schmale, M. Reh, and M. Gärttner. *Scalable quantum state tomography with artificial neural networks*. 2021. arXiv: 2109.13776.

[102] M. S. Kaznady and D. F. James. "Numerical strategies for quantum tomography: Alternatives to full optimization". In: *Physical Review A - Atomic, Molecular, and Optical Physics* 79.2 (Feb. 2009). ISSN: 10502947. DOI: 10.1103/PhysRevA.79.022109.

[103] C. Granade, C. Ferrie, and S. T. Flammia. "Practical adaptive quantum tomography". In: *New Journal of Physics* 19.11 (Nov. 2017). ISSN: 13672630. DOI: 10.1088/1367-2630/aa8fe6.

[104] M. Cerezo et al. "Variational Quantum Fidelity Estimation". In: *Quantum* 4 (Mar. 2020). ISSN: 2521327X. DOI: 10.22331/q-2020-03-26-248.

[105] S. T. Flammia and Y. K. Liu. "Direct Fidelity Estimation from Few Pauli Measurements". In: *Physical Review Letters* 106.23 (June 2011). ISSN: 00319007. DOI: 10.1103/PhysRevLett.106.230501.

[106] M. P. Da Silva, O. Landon-Cardinal, and D. Poulin. "Practical Characterization of Quantum Devices without Tomography". In: *Physical Review Letters* 107.21 (Nov. 2011). ISSN: 00319007. DOI: 10.1103/PhysRevLett.107.210404.

[107] M. Łącki and J. Zakrzewski. "Fast Dynamics forAatoms in Optical Lattices". In: *Physical Review Letters* 110.6 (Feb. 2013). ISSN: 00319007. DOI: 10.1103/PhysRevLett.110.065301.

[108] F. Serwane et al. "Deterministic Preparation of a Tunable Few-Fermion System". In: *Science* 332.6027 (Apr. 2011), pp. 336–338. ISSN: 0036-8075. DOI: 10.1126/science.1201351.

Erklärung:

Ich versichere, dass ich diese Arbeit selbstständig verfasst habe und keine anderen als die angegebenen Quellen und Hilfsmittel benutzt habe.

Heidelberg, den 18.10.2021 .....